Spring 2016

Modeling, analysis, and simulation for aqueous-based ceramic pastes in freeze-form extrusion fabrication process

Mingyang Li

MODELING, ANALYSIS, AND SIMULATION FOR AQUEOUS-BASED CERAMIC

PASTES IN FREEZE-FORM EXTRUSION FABRICATION PROCESS

by

MINGYANG LI

A DISSERTATION

Presented to the Faculty of the Graduate School of the

MISSOURI UNIVERSITY OF SCIENCE AND TECHNOLOGY

In Partial Fulfillment of the Requirements for the Degree

DOCTOR OF PHILOSOPHY

in

MECHANICAL ENGINEERING

2016

Approved
Dr. Robert G. Landers, Advisor
Dr. Ming C. Leu, Co-Advisor
Dr. Kelly O. Homan
Dr. Kakkattukuzhy M. Isaac
Dr. Gregory E. Hilmas

ABSTRACT

During the freeze-form extrusion fabrication process, both the extrusion and freezing processes are complex due to the aqueous-based ceramic pastes' non-Newtonian behavior, large latent heat of the water contained in the paste, and the small temperature difference between the ambient and the paste. In this study, the steady-state relationship between plunger velocity and extrusion force is developed based on a modified Herschel-Bulkley viscosity model and the Navier-Stokes equations, and the dynamic response of the extrusion force is described by a first-order nonlinear equation when plunger velocity is taken as an input. It is shown that the extrusion response time depends on the amount of air inside the extruder and the magnitude of the extrusion force. Air bubble release and pre-loading are then analyzed based on the developed constitutive model. The freezing process is modeled by a simplified one-dimensional heat transfer model and a lumped method. As the layer number increases, the paste freezing time increases and finally reaches a steady state. A non-dimensional analytical solution for the freezing time of parts with large numbers of layers was obtained using the lumped method. The effects of both non-dimensional and dimensional factors on the critical freezing time were studied. The critical freezing time is the time when the steady-state freezing time equals the total time between layers, which is the sum of the deposition time for the current layer and the dwell time between the current and next layers. A series of simulations and experiments were conducted to validate the predictive capabilities of the constitutive model for the extrusion force and the critical freezing time for parts with large numbers of layers. Good agreements between the simulation and experimental results were obtained.

ACKNOWLEDGMENTS

TABLE OF CONTENTS

LIST OF ILLUSTRATIONS

LIST OF TABLES

NOMENCLATURE

Symbol	Description
r, θ, z	Coordinates (m, rad, m, respectively)
u_r, u_θ, u_z	Radial, cylindrical, and longitudinal velocities, respectively (m/s)
ρ	Density (kg/m^3)
t	Time (s)
g	Gravity (m/s^2)
p	Pressure (Pa)
σ	Shear stress (Pa)
σ_{rz}	Shear stress caused by longitudinal velocity changing in radial direction (Pa)
μ	Viscosity (Pa·s)
σ_0	Yield shear stress (Pa)
κ	Consistency index (kg/m·s)
n	Power law index
$\dot{\gamma}$	Shear rate (s^{-1})
$\dot{\gamma}_c$	Critical shear rate (s^{-1})
p'	Pressure drop rate (Pa/m)
B, C	Constants
r_0	Pipe radius (m)
r_c	Critical radius, where critical shear rate occurs (m)
u_{bulk}	Paste bulk velocity (m/s)
A	Area (m^2)
P'	Pressure drop rate function (Pa/m)
u_p	Plunger velocity (m/s)
r_p	Plunger radius (m)
F_{ram}	Ram force (N)
F_{fric}	Friction force between plunger and barrel (N)
A_p	Plunger cross-sectional area (m^2)
V	Volume (m^3)

V_a	Air volume (m^3)
u_a	Bulk velocity of paste-air interface (m/s)
p_a	Air pressure (Pa)
p_{atm}	Atmospheric pressure (Pa)
l_0	Initial air layer thickness (m)
K_t	Time constant (s)
K_L	Gain (N·s/m)
l_p	Total length of paste in nozzle (m)
ε	Dummy variable
T	Temperature (°C)
k	Thermal conductivity (W/m·°C)
H	Enthalpy (J/kg)
$\dot{S}$	Volumetric rate of heat generation or absorption (W/m^3)
c	Specific heat (J/kg·°C)
χ	Material's liquid fraction
L	Latent heat (J/kg)
T_∞	Ambient temperature (°C)
h	Convection coefficient (W/m^2·°C)
n	Normal vector to the boundary surface
v	Volume fraction
m	Mass fraction
Subscript P	Variable of paste
Subscript e	Variable of ceramic particles
Subscript w	Variable of water
Subscript b	Variable of binder plus despersant
Subscript u	Variable of mixture of ceramic particles, binder, and dispersant
D	Part's effective dimension (m)
k_∞	Thermal conductivity of air (W/m·°C)
Pr	Prandtl number
Ra	Rayleigh number

Re	Reynolds number
β	Coefficient of volume expansion (1/K)
v_∞	Kinematic viscosity of air (m^2/s)
Δy	Filament width (m)
Δz	Filament height (m)
δ_t	Time step size (s)
δ_z	Spatial step size (m)
t_c	Critical freezing time (s)
T_0	Initial paste temperature (°C)
Subscript s	Solid region
Subscript m	Mushy region
Subscript l	Liquid region
T_S	Solidus temperature (°C)
τ	Non-dimensional time
Bi	Effective Biot number
Bi$_z$	Effective Biot number on top surface
η	Non-dimensional enthalpy
E	Non-dimensional latent heat
λ	Eigenvalue
W	Lambert W function, principal branch
τ_f	Non-dimensional freezing time
τ_d	Non-dimensional steady state freezing time
τ_ξ	Non-dimensional total time between layers

1. INTRODUCTION

Due to their high heat resistance and hardness, ceramic materials are widely used in automotive, aerospace and other industries. However, traditional technologies for processing ceramic materials are very expensive and time consuming when fabricating parts with complex geometries. Over the past few years, several Solid Freeform Fabrication (SFF), also called Rapid Prototyping (RP), Additive Manufacturing (AM) and other names, processes have been developed to fabricate ceramic components from three-dimensional (3D) CAD models. Freeze-form Extrusion Fabrication (FEF) is a novel, environmentally friendly SFF method for fabricating ceramic parts [1-3]. In this process aqueous-based ceramic pastes with high solids loadings up to 60 vol.% and trace amounts of organic binder (1-4 vol.%) are used in a low-temperature environment (< 0 ^oC) to fabricate parts. During the process, the aqueous based colloidal paste is extruded from one or multiple extruders to fabricate a ceramic component in a layer-by-layer manner. The low-temperature environment aids the part in maintaining its shape by freezing the water present in the paste.

The paste used in FEF process was a combination of ceramic powder, organic binder, dispersant, and deionized water. During the paste preparing process, the ceramic powder was dispersed in deionized water using dispersant, then this mixture was ball milled to break up agglomerates and to produce a uniform mixture. Binder was then added to the slurry with mechanical stirring to increase paste viscosity and to assist in forming a stronger green body after drying. Finally, a vacuum mixer was used to remove air bubbles trapped in the paste.

Three types of methods have been used to predict extrusion force in the literature. The first category includes the Benbow-Bridgwater model [4], the viscoplasticity method [5] and the artificial neural network method [6]. This type of method, especially the Benbow-Bridgwater model, is widely used in the prediction of extrusion forces. The parameters in the predictive models are usually obtained empirically. These techniques are not based on a viscosity model; instead, viscosity is measured by extrusion experiments or other standard methods. The second type of method includes upper bound techniques [7] and finite element methods [8,9], which are numerical techniques. This

type of methods uses the basic material properties, such as viscosity and density; however, they typically need to solve a set of high-order partial differential equations, which is very time-consuming. In addition, this type of methods does not provide the insights that can be used to derive a constitutive extrusion law, which is crucial for efficient process planning and controller design. The third type of methods includes analytical studies which are also based on basic material properties [10]. In this type of methods, the paste viscosity is characterized by the Herschel-Bulkley model [11] and then the relationship between extrusion force and plunger velocity is developed. However, in the previous study [12], the Hershel-Bulkley model considered the zero-shear viscosity as infinite, which introduces errors during the extrusion transient phases.

The dynamic response, which is related to extrusion mass flow rate, is also important for precise EOD in the FEF process [13]; however, only empirical modeling work has been done thus far. Mason et al. [2] characterized the extrusion force dynamics for ceramic paste by a first-order linear model using experiments where constant ram velocities in the operating range were applied to estimate model parameters. They observed significant variation in the time constant, which is caused by different amounts of air trapped in the paste. They ascribed this phenomenon to paste inhomogenity. Zhao et al. [3] noted that as paste is extruded, air bubble release will decrease the effective compressibility of the paste; therefore, the time constant will decrease and the gain will increase. Zhu and Smay [14] studied the thixotropic rheology of alumina paste empirically using structural kinetics; however, their theory cannot explain the change in time constant before and after air bubble release.

In Sections 2 and 3 of this dissertation, the extruder geometry was modeled as a series of pipes, and the paste was modeled as an incompressible fluid whose viscosity was characterized using a modified Herschel-Bulkley model. The Navier-Stokes equation was utilized to describe the paste flow and then simplified to investigate the steady-state relationship between plunger velocity and extrusion force. Compressibility was taken into consideration by adding air bubbles into the incompressible paste and a dynamic extrusion force model is obtained. Air bubble release was then analyzed using this constitutive model. A capillary rheometer was used to determine the viscosity model parameters, which were then used in the constitutive model to predict the extrusion force.

Capillary rheometers have a wide working range [15], which is important for the highly viscous paste used in the Freeze-form Extrusion Fabrication (FEF) process [2, 3]. Extrusion experiments were conducted by using a single extruder to validate the steady-state and transient characteristics of the dynamic extrusion force model. The extrusion equipment with its control system was described in detail in [2, 3, 13]. Highly nonlinear paste responses at low extrusion forces and air bubble release were observed in many of the extrusion experiments. Simulation and experimental studies were conducted to analyze these phenomena.

After the paste is extruded from the extruder nozzle, the paste freezes very quickly when it is directly deposited on a metal substrate in the subzero temperature environment. However, as the part height increases, the heat conduction rate to the substrate decreases and, thus, the freezing time increases. In some cases, the freezing time may substantially exceed the time required to extrude one paste layer. When the paste is not totally frozen and remains in a semiliquid state, a large part may deform or even collapse during the fabrication process. As in most additive manufacturing processes, the spatial and temporal temperature distributions, which affect part quality and dimensional accuracy, are significantly influenced by the process parameters. Therefore, the factors affecting the paste freezing time should be investigated in order to determine the time required for freezing and, thus, prevent the part from collapsing or deformation while minimizing the fabrication time.

Both experimental studies and thermal analysis are widely used to understand the physics of AM processes and to improve the part quality of these processes. Zeng et al. [16] reviewed the thermal analysis methods in Laser Sintering and Selective Laser Melting processes. The governing equations, boundary conditions, material properties, energy source characteristics, analytical solutions, and numerical simulations were reviewed in this paper. Tapia et al. [17] reviewed temperature and displacement sensors, monitoring setup, and control research progress in metal-based AM processes. Both of the review papers noted that there is still a significant lack of physical understanding and mathematical models for thermal analysis of AM processes. In some of the recent AM research, the effects of interpass idle time [18], heat transfer rate [19], and slice thickness [20] on thermal stresses and part distortions were investigated.

Numerical simulation was the main method used to conduct thermal analysis in AM processes. In a related freeform fabrication process, the rapid freeze prototyping process [21], which uses water as the part material, the solidification time was studied using both finite difference analysis [22] and finite element analysis [23,24]. Since the simulation is computational expensive, an adaptive meshing method [25] and dimension reduction [26] were applied to reduce node number and simulation time. However, few analytical studies [27] have been done and the basic physical understanding is still lacking.

In Section 4 of this dissertation, a simplified one-dimensional (1D) heat transfer model was introduced to provide a deep understanding of the paste freezing behavior, and the model was validated by the commercial finite element software FLUENT. The paste temperature and the paste freezing time were computed via numerical simulations based on this simplified model. Eight factors were considered in this study, including total time between layers, convection coefficient, material, solids loading, initial paste temperature, ambient temperature, filament height, and filament width. Their effects on the steady-state and critical freezing times for parts built starting from the substrate were studied.

In Section 5 of this dissertation, a lumped method was used to further the understanding of FEF processes in fabricating thin-wall parts. A non-dimensional analytical solution for the critical freezing time (i.e., when the steady-state freezing time is equal to the total time between layers) was obtained from this method, and its corresponding dimensional solution was compared with numerical simulation results. Experiments using different pastes and extrusion parameters were conducted to validate the prediction of the lumped method. Possible error sources during the experiments were discussed and their corresponding effects were estimated.

2. EXTRUSION PROCESS MODELING FOR AQUEOUS-BASED CERAMIC PASTES, PART 1: CONSTITUTIVE MODEL

2.1. ASSUMPTIONS AND BOUNDARY CONDITIONS

The following assumptions are made:

(1) The extruder geometry is modeled as a series of pipes.

(2) Since the extrusion velocity is slow (10^{-5} to 10^{-2} m/s) and the paste viscosity is high (~20 Pa·s), the Reynolds Number will be much smaller than 1; therefore, the flow is taken as laminar.

(3) Since the Reynolds Number is small, the developing section of flow is much shorter than the length of flow channel; therefore, the flow is taken as fully developed.

(4) Since the extrusion velocity is slow, the pressure drop caused by changing flow channel cross-sections is negligible.

(5) The material is homogenous.

(6) The flow channel is completely filled by paste, except for studies where air is present.

(7) Unless otherwise stated, the paste is incompressible.

(8) The temperature is constant. Therefore, viscosity is only a function of shear rate, and density is only a function of pressure.

(9) The paste does not experience slip at the wall.

The following boundary conditions are used:

(1) Since the paste is assumed to not experience slip at the wall, the paste velocity at the wall is zero.

(2) The pressure at the extruder outlet is 101,325 Pa, i.e., 1 atm.

(3) The plunger is modeled as a moving wall. Thus, the paste velocity at the plunger contact is the same as the plunger velocity.

2.2. STEADY-STATE EXTRUSION FORCE MODEL

While flowing in a pipe, the paste continuity and momentum equations can be described by the Navier-Stokes equations in cylindrical coordinates. Since there is no source or velocity in the θ direction, the terms involving θ can be neglected. The continuity equation becomes

$$\frac{1}{r}\frac{\partial}{\partial r}(ru_r) + \frac{\partial u_z}{\partial z} = 0 \tag{2.1}$$

The momentum equation in the radial direction is

$$\rho\left[\frac{\partial u_r}{\partial t} + u_r\frac{\partial u_r}{\partial r} + u_z\frac{\partial u_z}{\partial z}\right] = \rho g_r - \frac{\partial p}{\partial r} + \frac{1}{r}\frac{\partial}{\partial r}(r\sigma_{rr}) - \frac{\sigma_{rr}}{r} + \frac{\partial \sigma_{rz}}{\partial z} \tag{2.2}$$

The momentum equation in the circumferential direction is neglected and the momentum equation in the longitudinal direction is

$$\rho\left[\frac{\partial u_z}{\partial t} + u_r\frac{\partial u_z}{\partial r} + u_z\frac{\partial u_z}{\partial z}\right] = \rho g_z - \frac{\partial p}{\partial z} + \frac{1}{r}\frac{\partial}{\partial r}(r\sigma_{rz}) + \frac{\partial \sigma_{zz}}{\partial z} \tag{2.3}$$

For fully developed flow, $\frac{\partial u_z}{\partial t} = 0$, $u_r = 0$, $\frac{\partial u_z}{\partial z} = 0$ and $\frac{\partial \sigma_{zz}}{\partial z} = 0$. In this case Eq. (2.2) can be neglected, and Eq. (2.3) can be rewritten as

$$\rho g_z - \frac{\partial p}{\partial z} + \frac{1}{r}\frac{\partial}{\partial r}(r\sigma_{rz}) = 0 \tag{2.4}$$

Rearranging Eq. (2.4) and integrating with respect to r

$$r\sigma_{rz} = \frac{1}{2}\left(\frac{\partial p}{\partial z} - \rho g_z\right)r^2 + B_0 \tag{2.5}$$

When $r = 0$, σ_{rz} must be finite; therefore, $B_0 = 0$ and

$$\sigma_{rz} = \frac{1}{2}\left(\frac{\partial p}{\partial z} - \rho g_z\right)r \tag{2.6}$$

Previous research has shown that the paste viscosity has a yield stress and a shear thinning behavior [1]. This type of viscosity can be described by a modified Herschel-Bulkley model [28]

$$
\mu = \begin{cases}
\dfrac{\sigma_0}{|\dot{\gamma}|} + \kappa \dfrac{|\dot{\gamma}|^{n-1}}{\dot{\gamma}_c^{n-1}} & \text{if} \quad |\dot{\gamma}| \geq \dot{\gamma}_c \\[2ex]
\left[\dfrac{2\sigma_0}{\dot{\gamma}_c} + \kappa(2-n) \right] + \left[\dfrac{\kappa(n-1)}{\dot{\gamma}_c} - \dfrac{\sigma_0}{\dot{\gamma}_c^2} \right] |\dot{\gamma}| & \text{if} \quad |\dot{\gamma}| < \dot{\gamma}_c
\end{cases}
\tag{2.7}
$$

Substituting Eq. (2.7) into the equation $\sigma_{rz} = \mu\dot{\gamma}$ where $\dot{\gamma} = \dfrac{\partial u_z}{\partial r}$ in fully developed flow

$$
\sigma_{rz} = \begin{cases}
\left(\sigma_0 \left| \dfrac{\partial u_z}{\partial r} \right|^{-1} + \dfrac{\kappa}{\dot{\gamma}_c^{n-1}} \left| \dfrac{\partial u_z}{\partial r} \right|^{n-1} \right) \left(\dfrac{\partial u_z}{\partial r} \right) & \text{if} \quad \left| \dfrac{\partial u_z}{\partial r} \right| \geq \dot{\gamma}_c \\[2ex]
\left[\dfrac{2\sigma_0}{\dot{\gamma}_c} + \kappa(2-n) \right] \left(\dfrac{\partial u_z}{\partial r} \right) + \left[\dfrac{\kappa(n-1)}{\dot{\gamma}_c} - \dfrac{\sigma_0}{\dot{\gamma}_c^2} \right] \left| \dfrac{\partial u_z}{\partial r} \right| \left(\dfrac{\partial u_z}{\partial r} \right) & \text{if} \quad \left| \dfrac{\partial u_z}{\partial r} \right| < \dot{\gamma}_c
\end{cases}
\tag{2.8}
$$

Apparently $\sigma_{rz}\left(-\dfrac{\partial u_z}{\partial r} \right) = -\sigma_{rz}\left(\dfrac{\partial u_z}{\partial r} \right)$, which means that once the shear stress for fluid flows in one direction is computed, the shear stress for fluid flows in the reverse direction can be obtained by simply changing the sign. Therefore, to simplify the derivation process, the condition when $\dfrac{\partial u_z}{\partial r} \geq 0$ is considered in the sequent derivation. Thus, Eq. (2.8) becomes

$$
\sigma_{rz} = \begin{cases}
\sigma_0 + \dfrac{\kappa}{\dot{\gamma}_c^{n-1}} \left(\dfrac{\partial u_z}{\partial r} \right)^n & \text{if} \quad \dfrac{\partial u_z}{\partial r} \geq \dot{\gamma}_c \\[2ex]
\left[\dfrac{2\sigma_0}{\dot{\gamma}_c} + \kappa(2-n) \right] \left(\dfrac{\partial u_z}{\partial r} \right) + \left[\dfrac{\kappa(n-1)}{\dot{\gamma}_c} - \dfrac{\sigma_0}{\dot{\gamma}_c^2} \right] \left(\dfrac{\partial u_z}{\partial r} \right)^2 & \text{if} \quad \dfrac{\partial u_z}{\partial r} < \dot{\gamma}_c
\end{cases}
\tag{2.9}
$$

From Eqs. (2.6) and (2.9), when $\dfrac{\partial u_z}{\partial r} \geq \dot{\gamma}_c$

$$\sigma_0 + \frac{\kappa}{\dot{\gamma}_c^{n-1}}\left(\frac{\partial u_z}{\partial r}\right)^n = \frac{1}{2}\left(\frac{\partial p}{\partial z} - \rho g_z\right)r \tag{2.10}$$

Rearranging Eq. (2.10)

$$\frac{\partial u_z}{\partial r} = \frac{du_z}{dr} = \left[\frac{\dot{\gamma}_c^{n-1}\left(\frac{\partial p}{\partial z} - \rho g_z\right)}{2\kappa}r - \frac{\dot{\gamma}_c^{n-1}\sigma_0}{\kappa}\right]^{\frac{1}{n}} \tag{2.11}$$

Letting $p' = \left(\frac{\partial p}{\partial z} - \rho g_z\right)$, $C_1 = \frac{\dot{\gamma}_c^{n-1}}{2\kappa}$, and $C_2 = \frac{\dot{\gamma}_c^{n-1}\sigma_0}{\kappa}$, Eq. (2.11) can be rewritten as

$$\frac{du_z}{dr} = \left(C_1 p' r - C_2\right)^{\frac{1}{n}} \tag{2.12}$$

Solving Eq. (2.12)

$$u_z = \frac{n}{n+1} \cdot \frac{1}{C_1 p'}\left(C_1 p' r - C_2\right)^{\frac{n+1}{n}} + B_1 \tag{2.13}$$

From Eq. (2.9) when $\dfrac{du_z}{dr} < \dot{\gamma}_c$

$$\left[\frac{2\sigma_0}{\dot{\gamma}_c} + \kappa(2-n)\right]\left(\frac{\partial u_z}{\partial r}\right) + \left[\frac{\kappa(n-1)}{\dot{\gamma}_c} - \frac{\sigma_0}{\dot{\gamma}_c^2}\right]\left(\frac{\partial u_z}{\partial r}\right)^2 = \frac{1}{2}\left(\frac{\partial p}{\partial z} - \rho g_z\right)r \tag{2.14}$$

Letting $C_3 = \dfrac{2\sigma_0}{\dot{\gamma}_c} + \kappa(2-n)$ and $C_4 = \dfrac{\kappa(n-1)}{\dot{\gamma}_c} - \dfrac{\sigma_0}{\dot{\gamma}_c^2}$, Eq. (2.14) can be rewritten as

$$C_4\left(\frac{\partial u_z}{\partial r}\right)^2 + C_3\left(\frac{\partial u_z}{\partial r}\right) - \frac{1}{2}p'r = 0 \tag{2.15}$$

Solving Eq. (2.15)

$$\frac{\partial u_z}{\partial r} = \frac{du_z}{dr} = -\frac{C_3}{2C_4} \pm \frac{1}{2C_4}\left(C_3^2 + 2C_4 p' r\right)^{\frac{1}{2}} \tag{2.16}$$

Since $\sigma_0 > 0$, $\dot{\gamma}_c > 0$, $\kappa > 0$, $p' > 0$, $r \geq 0$ and $0 < n < 1$, $C_3 > 0$ and $C_4 < 0$. Therefore,

if $\dfrac{du_z}{dr} = -\dfrac{C_3}{2C_4} - \dfrac{1}{2C_4}\left(C_3^2 + 2C_4 p' r\right)^{\frac{1}{2}}$, when $r = 0$

$$\frac{du_z}{dr} = -\frac{C_3}{C_4} = -\frac{\dfrac{2\sigma_0}{\dot{\gamma}_c} + \kappa(2-n)}{\dfrac{\kappa(n-1)}{\dot{\gamma}_c} - \dfrac{\sigma_0}{\dot{\gamma}_c^2}} = \frac{2\sigma_0 + \dot{\gamma}_c \kappa(2-n)}{\sigma_0 + \dot{\gamma}_c \kappa(1-n)} \dot{\gamma}_c > 2\dot{\gamma}_c \qquad (2.17)$$

This is contrary to the assumption $\dfrac{du_z}{dr} < \dot{\gamma}_c$. Therefore

$$\frac{du_z}{dr} = -\frac{C_3}{2C_4} + \frac{1}{2C_4}\left(C_3^2 + 2C_4 p' r\right)^{\frac{1}{2}} \qquad (2.18)$$

Solving Eq. (2.18)

$$u_z = -\frac{C_3}{2C_4} r + \frac{1}{6C_4^2 p'}\left(C_3^2 + 2C_4 p' r\right)^{\frac{3}{2}} + B_2 \qquad (2.19)$$

Therefore, the paste velocity in the longitudinal direction is

$$u_z = \begin{cases} \dfrac{n}{n+1} \cdot \dfrac{1}{C_1 p'}\left(C_1 p' r - C_2\right)^{\frac{n+1}{n}} + B_1 & \text{if} \quad \dfrac{du_z}{dr} \geq \dot{\gamma}_c \\[4mm] -\dfrac{C_3}{2C_4} r + \dfrac{1}{6C_4^2 p'}\left(C_3^2 + 2C_4 p' r\right)^{\frac{3}{2}} + B_2 & \text{if} \quad \dfrac{du_z}{dr} < \dot{\gamma}_c \end{cases} \qquad (2.20)$$

There are two possible conditions at $r = r_0$: (1) $\dfrac{du_z}{dr} \geq \dot{\gamma}_c$ and (2) $\dfrac{du_z}{dr} < \dot{\gamma}_c$. For condition

(1), the velocity profile is given by Eq. (2.20), which can be rewritten as

$$u_z = \begin{cases} \dfrac{n}{n+1} \cdot \dfrac{1}{C_1 p'}\left(C_1 p' r - C_2\right)^{\frac{n+1}{n}} + B_1 & \text{if} \quad r \geq r_c \\[4mm] -\dfrac{C_3}{2C_4} r + \dfrac{1}{6C_4^2 p'}\left(C_3^2 + 2C_4 p' r\right)^{\frac{3}{2}} + B_2 & \text{if} \quad r < r_c \end{cases} \qquad (2.21)$$

and the velocity profile should be continuous, which implies

$$u_z\big|_{r=r_c-} = u_z\big|_{r=r_c+} \tag{2.22}$$

The boundary condition is

$$u_z\big|_{r=r_0} = 0 \tag{2.23}$$

The definition of bulk velocity is

$$u_{bulk} = \frac{1}{A}\int_A u_z dA = \frac{2}{r_0^2}\int_0^{r_0} u_z r dr \tag{2.24}$$

Substituting Eq. (2.23) into Eq. (2.21) for $r \geq r_c$

$$\frac{n}{n+1}\cdot\frac{1}{C_1 p'}\left(C_1 p' r_0 - C_2\right)^{\frac{n+1}{n}} + B_1 = 0 \tag{2.25}$$

Solving Eq. (2.25) for B_1

$$B_1 = -\frac{n}{n+1}\cdot\frac{1}{C_1 p'}\left(C_1 p' r_0 - C_2\right)^{\frac{n+1}{n}} \tag{2.26}$$

Substituting Eq. (2.26) into Eq. (2.21) for $r \geq r_c$

$$u_z = \frac{n}{n+1}\cdot\frac{1}{C_1 p'}\left(C_1 p' r - C_2\right)^{\frac{n+1}{n}} - \frac{n}{n+1}\cdot\frac{1}{C_1 p'}\left(C_1 p' r_0 - C_2\right)^{\frac{n+1}{n}} \tag{2.27}$$

When $r = r_c$, $\dfrac{du_z}{dr} = \dot{\gamma}_c$. Substituting into Eq. (2.12) and solving for r_c

$$r_c = \frac{\dot{\gamma}_c^n + C_2}{C_1 p'} \tag{2.28}$$

From Eq. (2.22)

$$\frac{n}{n+1}\cdot\frac{1}{C_1 p'}\left[\left(C_1 p' r_c - C_2\right)^{\frac{n+1}{n}} - \left(C_1 p' r_0 - C_2\right)^{\frac{n+1}{n}}\right]$$
$$= -\frac{C_3}{2C_4} r_c + \frac{1}{6C_4^2 p'}\left(C_3^2 + 2C_4 p' r_c\right)^{\frac{3}{2}} + D_2 \tag{2.29}$$

Substituting Eq. (2.28) into Eq. (2.29) and solving for B_2

$$B_2 = \frac{n}{n+1} \cdot \frac{1}{C_1 p'} \left[\dot{\gamma}_c^{n+1} - \left(C_1 p' r_0 - C_2\right)^{\frac{n+1}{n}} \right]$$

$$+ \frac{C_3 \left(\dot{\gamma}_c^n + C_2\right)}{2 C_4 C_1 p'} - \frac{1}{6 C_4^2 p'} \left[C_3^2 + \frac{2 C_4 \left(\dot{\gamma}_c^n + C_2\right)}{C_1} \right]^{\frac{3}{2}} \tag{2.30}$$

Substituting Eq. (2.30) into Eq. (2.21) for $r < r_c$

$$u_z = -\frac{C_3}{2 C_4} r + \frac{1}{6 C_4^2 p'} \left(C_3^2 + 2 C_4 p' r\right)^{\frac{3}{2}}$$

$$+ \frac{n}{n+1} \cdot \frac{1}{C_1 p'} \left[\dot{\gamma}_c^{n+1} - \left(C_1 p' r_0 - C_2\right)^{\frac{n+1}{n}} \right] \tag{2.31}$$

$$+ \frac{C_3 \left(\dot{\gamma}_c^n + C_2\right)}{2 C_4 C_1 p'} - \frac{1}{6 C_4^2 p'} \left[C_3^2 + \frac{2 C_4 \left(\dot{\gamma}_c^n + C_2\right)}{C_1} \right]^{\frac{3}{2}}$$

In this case, Eq. (2.24) becomes

$$\int_0^{r_0} u_z r \, dr = \int_0^{r_c} u_z r \, dr + \int_{r_c}^{r_0} u_z r \, dr = \frac{r_0^2}{2} u_{bulk} \tag{2.32}$$

Substituting Eqs. (2.27) and (2.31) into Eq. (2.32) and rearranging

$$-\frac{n^3}{(n+1)(2n+1)(3n+1) C_1^3} \cdot \frac{\left(C_1 p' r_0 - C_2\right)^{\frac{3n+1}{n}}}{p'^3}$$

$$+ \frac{n^2 r_0}{(n+1)(2n+1) C_1^2} \cdot \frac{\left(C_1 p' r_0 - C_2\right)^{\frac{2n+1}{n}}}{p'^2} \tag{2.33}$$

$$- \frac{n r_0^2}{2(n+1) C_1} \cdot \frac{\left(C_1 p' r_0 - C_2\right)^{\frac{n+1}{n}}}{p'} + \frac{C_5}{p'^3} - \frac{u_{bulk} r_0^2}{2} = 0$$

where

$$C_5 = \frac{C_3^7 - \left[C_3^2 + \dfrac{2C_4\left(\dot{\gamma}_c^n + C_2\right)}{C_1}\right]^{\frac{7}{2}}}{210C_4^4} + \frac{\left(\dot{\gamma}_c^n + C_2\right)\left[C_3^2 + \dfrac{2C_4\left(\dot{\gamma}_c^n + C_2\right)}{C_1}\right]^{\frac{5}{2}}}{30C_4^3 C_1}$$

$$- \frac{\left(\dot{\gamma}_c^n + C_2\right)^2 \left[C_3^2 + \dfrac{2C_4\left(\dot{\gamma}_c^n + C_2\right)}{C_1}\right]^{\frac{3}{2}}}{12C_4^2 C_1^2} + \frac{C_3\left(\dot{\gamma}_c^n + C_2\right)^3}{12C_4 C_1^3} + \frac{n\dot{\gamma}_c^{n+1}\left(\dot{\gamma}_c^n + C_2\right)^2}{2(n+1)C_1^3} \quad (2.34)$$

$$- \frac{n^2\dot{\gamma}_c^{2n+1}\left(\dot{\gamma}_c^n + C_2\right)}{(n+1)(2n+1)C_1^3} + \frac{n^3\dot{\gamma}_c^{3n+1}}{(n+1)(2n+1)(3n+1)C_1^3}$$

In Eq. (2.33), $\dot{\gamma}_c$, C_1, C_2, C_3, C_4 and C_5 are given and they are functions of material properties, and r_0 is determined by the ram geometry. Given a value of u_{bulk}, p' can be solved numerically using Eq. (2.33).

For condition (2) (i.e., $\dfrac{du_z}{dr} < \dot{\gamma}_c$) at $r = r_0$, the velocity profile is

$$u_z = -\frac{C_3}{2C_4}r + \frac{1}{6C_4^2 p'}\left(C_3^2 + 2C_4 p' r\right)^{\frac{3}{2}} + B_2 \quad (2.35)$$

The boundary conditions are given by Eqs. (2.23) and (2.24). Substituting Eq. (2.23) into Eq. (2.35)

$$0 = -\frac{C_3}{2C_4}r_0 + \frac{1}{6C_4^2 p'}\left(C_3^2 + 2C_4 p' r_0\right)^{\frac{3}{2}} + B_2 \quad (2.36)$$

Solving Eq. (2.36) for B_2

$$B_2 = \frac{C_3}{2C_4}r_0 - \frac{1}{6C_4^2 p'}\left(C_3^2 + 2C_4 p' r_0\right)^{\frac{3}{2}} \quad (2.37)$$

Substituting Eq. (2.37) into Eq. (2.35)

$$u_z = \left[-\frac{C_3}{2C_4} r + \frac{1}{6C_4^2 p'} \left(C_3^2 + 2C_4 p' r \right)^{\frac{3}{2}} \right]$$
$$- \left[\frac{1}{6C_4^2 p'} \left(C_3^2 + 2C_4 p' r_0 \right)^{\frac{3}{2}} - \frac{C_3}{2C_4} r_0 \right] \tag{2.38}$$

Substituting Eq. (2.38) into Eq. (2.24)

$$\frac{u_{bulk} r_0^2}{2} = \int_0^{r_0} \left\{ \left[-\frac{C_3}{2C_4} r + \frac{1}{6C_4^2 p'} \left(C_3^2 + 2C_4 p' r \right)^{\frac{3}{2}} \right] \right.$$
$$\left. - \left[\frac{1}{6C_4^2 p'} \left(C_3^2 + 2C_4 p' r_0 \right)^{\frac{3}{2}} - \frac{C_3}{2C_4} r_0 \right] \right\} r dr \tag{2.39}$$

Integrating the left side of Eq. (2.39)

$$\frac{r_0 \left(C_3^2 + 2C_4 p' r_0 \right)^{\frac{5}{2}}}{30 C_4^3 p'^2} + \frac{C_3^7 - \left(C_3^2 + 2C_4 p' r_0 \right)^{\frac{7}{2}}}{210 C_4^4 p'^3}$$
$$+ \frac{C_3 r_0^3}{12 C_4} - \frac{\left(C_3^2 + 2C_4 p' r_0 \right)^{\frac{3}{2}} r_0^2}{12 C_4^2 p'} - \frac{u_{bulk} r_0^2}{2} = 0 \tag{2.40}$$

In Eq. (2.40), the parameters C_1, C_2, C_3 and C_4 are functions of material properties, and

the parameter r_0 is determined by the ram geometry. Given a value of u_{bulk}, p' can be

computed numerically using Eq. (2.40). Then, for specific values of r_0 and u_{bulk}, r_c is

calculated from Eq. (2.28). If $r_0 > r_c$, then p' is solved from Eq. (2.33); if $r_0 \leq r_c$, p' is

solved from Eq. (2.40).

From the above derivation and discussion, p' is a function of material properties,

flow channel radius and paste bulk velocity, and can be written in the form

$$p' = P'\left(n, \ \kappa, \ \sigma_0, \ \dot{\gamma}_c, \ r_0, \ u_{bulk} \right) \tag{2.41}$$

Typically the plunger velocity u_p is known. Then, for a ram extruder having N sections,

each with different radius $r_{0,i}$, the paste bulk velocity for each section is $\dfrac{r_p^2}{r_{0,i}^2} u_p$ ($i =$

$1,\ldots,N$). Therefore, the pressure drop rate in section i is

$$p_i' = P'\left(n,\ \kappa,\ \sigma_0,\ \dot{\gamma}_c,\ r_{0,i},\ \frac{r_p^2}{r_{0,i}^2} u_p \right) \tag{2.42}$$

Thus, the pressure drop from the ram to the nozzle tip is

$$P = \sum_{i=1}^{N} p_i'\, l_i \tag{2.43}$$

which is a function of material properties, extruder geometry and plunger velocity. For

specific material properties, the pressure drop is a function of plunger velocity and

plunger position

$$P = P\left(z,\ u_p \right) \tag{2.44}$$

For most extruders, the barrel radius is much larger than the nozzle radius; therefore, the

paste velocity in the barrel is much lower. In this case, the pressure drop in the barrel can

be neglected, and the pressure drop function becomes

$$P = P\left(u_p \right) \tag{2.45}$$

Typically, a ram driven by a motor is used to push a plunger to extrude paste. A load cell

can be connected to the ram to measure the force between the ram and the plunger, which

is referred to as the extrusion force. Therefore, the relationship between extrusion force

and plunger velocity is

$$F_{ram} = A_p P\left(u_p \right) + F_{fric}\, \mathrm{sgn}\left(u_p \right) \tag{2.46}$$

In order to build this relationship to determine the extrusion force, the extruder geometry can be modeled as sections of pipes and the paste viscosity can be characterized using the modified Herschel-Bulkley model. For each extruder section, the pressure drop rate is determined by Eq. (2.42), and the pressure drop from the plunger to the nozzle tip is calculated by Eq. (2.45), or Eq. (2.44) if the pressure drop in the barrel is not negligible. Then, the relationship between extrusion force and plunger velocity is built from Eq. (2.46). This relationship depends on both the extruder geometry and the paste viscosity.

2.3. DYNAMIC EXTRUSION FORCE MODEL

During the paste extrusion process for a constant plunger velocity, the extrusion force response has been observed to be slow (on the order of minutes [2]) when the plunger velocity changes to another constant value. It is believed that material compressibility is the reason for this slow response. The paste, which is mainly composed of water and ceramic powder, is supposed to be an incompressible material. However, a small amount of air is often trapped in the paste as evidenced by air bubble release that has been observed during the extrusion process. Since the paste contains air bubbles, which become trapped in the paste during paste preparation and loading processes, the entire mixture can be treated as a compressible material. A dynamic extrusion force model is built on this assumption.

Consider a volume of compressible air in an incompressible paste with the mixture flowing in a pipe as shown in Figure 2.1. Applying volume conservation to the paste

$$\frac{dV_a(t)}{dt} = \int_{A_a} u_a \, dA - \int_{A_p} u_p \, dA \qquad (2.47)$$

The volume of the compressible air is a function of pressure

$$V_a = V(p_a) \qquad (2.48)$$

From Eq. (2.44), the absolute pressure of the compressible air is

$$p_a = P(z, u_a) + p_{atm} \qquad (2.49)$$

As mentioned in Section 2.2, when the ram geometry consists of a large radius barrel connected with a small radius nozzle, it can be shown that the pressure drop in the barrel is negligible. For this geometry, the position of the compressible material in the barrel is not important; therefore, the mixture can be modeled as a layer of compressible material above the incompressible paste in the barrel as illustrated in Figure 2.2.

Figure 2.1. Schematic of a volume of compressible air in an incompressible paste flowing in a pipe.
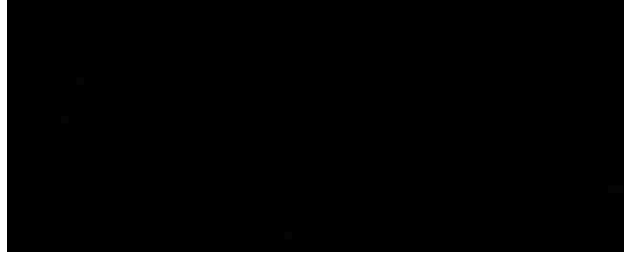
Figure 2.2. Schematic of a layer of compressible material above incompressible paste.

In this case, Eqs. (2.47) and (2.49), respectively, can be written as

$$\frac{dV_a(t)}{dt} = A_p \left[u_a(t) - u_p(t) \right] \tag{2.50}$$

$$p_a(t) = P\left[u_a(t) \right] + p_{atm} \tag{2.51}$$

If the compressible material in Figure 2.2 is pure air, based on the ideal gas model and assuming constant temperature, Eq. (2.48) becomes

$$V_a(t) = \frac{p_a(0)V_a(0)}{p_a(t)} \tag{2.52}$$

Integrating Eq. (2.50) with respect to time

$$V_a(t) = A_p \left[z_a(t) - z_p(t) \right] \tag{2.53}$$

If the air layer has an initial thickness l_0, then combining Eqs. (2.52) and (2.53) with

$V_a(0) = l_0 A_p$, and solving for $p_a(t)$

$$p_a(t) = \frac{p_a(0)l_0}{z_a(t) - z_p(t)} \tag{2.54}$$

Substituting Eq. (2.54) into Eq. (2.51) with the expression $u_a(t) = \dfrac{dz_a(t)}{dt}$

$$P\left[u_a(t)\right] + p_{atm} = P\left[\frac{dz_a(t)}{dt}\right] + p_{atm} = \frac{p_a(0)l_0}{z_a(t) - z_p(t)} \tag{2.55}$$

This equation can be rewritten as the following ordinary differential equation

$$\frac{dz_a(t)}{dt} = u_a(t) = P^{-1}\left[\frac{p_a(0)l_0}{z_a(t) - z_p(t)} - p_{atm}\right] \tag{2.56}$$

where P^{-1} is the function inverse of P. In this case, $z_a(t)$ can be obtained by solving Eq. (2.56) with the initial condition $z_a(0) = l_0$ and $u_a(t)$ is obtained from $u_a(t) = \dfrac{dz_a(t)}{dt}$.

Performing a force balance on the plunger, the extrusion force is

$$F_{ram}(t) = A_p\left[p_a(t) - p_{atm}\right] + F_{fric}\,\mathrm{sgn}\left(u_p\right) \tag{2.57}$$

Substituting Eq. (2.54) into Eq. (2.57)

$$F_{ram}(t) = A_p\left[\frac{p_a(0)l_0}{z_a(t) - z_p(t)} - p_{atm}\right] + F_{fric}\,\mathrm{sgn}\left(u_p\right) \tag{2.58}$$

Solving Eq. (2.58) for z_a

$$z_a(t) = z_p(t) + \frac{A_p p_a(0)l_0}{F_{ram}(t) - F_{fric}\,\mathrm{sgn}\left(u_p\right) + A_p p_{atm}} \tag{2.59}$$

Substituting Eq. (2.59) into Eq. (2.56) and rearranging

$$\begin{aligned}
\frac{dF_{ram}(t)}{dt} &= \frac{\left[F_{ram}(t) - F_{fric}\,\mathrm{sgn}\left(u_p\right) + A_p p_{atm}\right]^2}{A_p p_a(0)l_0} \\
&\quad \cdot\left\{u_p(t) - u_a\left[F_{ram}(t) - F_{fric}\,\mathrm{sgn}\left(u_p\right)\right]\right\}
\end{aligned} \tag{2.60}$$

From Eq. (2.56), Eq. (2.60) can also be written as

$$\frac{dF_{ram}(t)}{dt} = \frac{\left[F_{ram}(t) - F_{fric}\,\text{sgn}(u_p) + A_p p_{atm}\right]^2}{A_p p_a(0) l_0}$$
$$\cdot\left\{u_p(t) - P^{-1}\left[\frac{F_{ram}(t) - F_{fric}\,\text{sgn}(u_p)}{A_p}\right]\right\}$$

(2.61)

Equation (2.61) is the constitutive law for the extrusion of aqueous-based ceramic pastes. In this equation, the term $p_a(0)l_0$ is proportional to the total mass of air trapped in the paste. The term $F_{ram}(t) - F_{fric}\text{sgn}(u_p) + A_p p_{atm}$ is proportional to the pressure of air trapped in the paste. Note that the value of this term is always positive and, thus, when

$\frac{dF_{ram}(t)}{dt} = 0$, $u_p(t) - u_a(t) = 0$. When $u_p(t)$ changes from zero to some constant value,

F_{ram} increases from F_f to some steady-state extrusion force and, when $u_p(t)$ goes to zero,

F_{ram} will decrease from its current value to F_{fric}.

Since the dynamic extrusion force model is described by a first-order nonlinear equation, the response time cannot be determined analytically. However, it can be approximated by linearizing the dynamic extrusion force model at a nominal extrusion force $\bar{F}_{ram}$ and a corresponding nominal plunger velocity $\bar{u}_p = u_a\left(\bar{F}_{ram} - F_{fric}\,\text{sgn}(u_p)\right)$ as follows:

$$\dot{F}_{ram}(t) = G\left(F_{ram},\ u_p,\ t\right)$$
$$\approx G\left(\bar{F}_{ram},\ \bar{u}_p,\ t\right)$$
$$+ \frac{\partial G}{\partial F_{ram}}\bigg|_{\bar{F}_{ram},\bar{u}_p}\left[F_{ram}(t) - \bar{F}_{ram}\right] + \frac{\partial G}{\partial u_p}\bigg|_{\bar{F}_{ram},\bar{u}_p}\left[u_p(t) - \bar{u}_p\right]$$

(2.62)

The linearized model is

$$K_t\dot{\hat{F}}_{ram}(t) + \hat{F}_{ram}(t) = K_L\hat{u}_p(t)$$

(2.63)

where the incremental extrusion force and velocity, respectively, are

$$\hat{F}_{ram}(t) = F_{ram}(t) - \bar{F}_{ram} \tag{2.64}$$

$$\hat{u}_p(t) = u_p(t) - \bar{u}_p \tag{2.65}$$

In Eq. (2.63), the time constant is

$$K_t = -\frac{1}{\left.\dfrac{\partial G}{\partial F_{ram}}\right|_{\bar{F}_{ram},\bar{u}_p}} = \frac{A_p p_a(0) l_0}{\left.\dfrac{du_a}{dF_{ram}}\right|_{\bar{F}_{ram}} \left[\bar{F}_{ram} - \text{sgn}(u_p) F_{fric} + A_p p_{atm}\right]^2} \tag{2.66}$$

and the gain is

$$K_L = -\frac{\left.\dfrac{\partial G}{\partial u_p}\right|_{\bar{F}_{ram},\bar{u}_p}}{\left.\dfrac{\partial G}{\partial F_{ram}}\right|_{\bar{F}_{ram},\bar{u}_p}} = \left.\frac{dF_{ram}}{du_p}\right|_{\bar{u}_p} \tag{2.67}$$

The response time is determined by $p_a(0)l_0$, F_{ram} and du_a/dF_{ram}. As the value of $p_a(0)l_0$

increases, the response time increases. The effects of F_{ram} and du_a/dF_{ram} are more

complex since, for a specific paste and extruder, du_a/dF_{ram} is also a function of F_{ram}.

Typically, as the extrusion force F_{ram} increases, the response time decreases. The gain is

only determined by the relationship between u_p and F_{ram}. For a typical ceramic paste, as

the extrusion force F_{ram} increases, the gain decreases.

2.4. AIR BUBBLE RELEASE

Typically, air exists in the paste in the form of bubbles. During the extrusion

process, air bubbles may be released, causing an extrusion discontinuity and a sudden

drop in the extrusion force. This phenomenon can be described by the dynamic response

model derived in Section 2.3. When an air bubble goes through the nozzle, the volume of

paste in the nozzle will change. This process is shown in Figure 2.3. In this case the term

$p_a(t)$ in Eq. (2.51) is described by

$$p_a(t) = l_p(t) P'(u_a) + p_{atm} \tag{2.68}$$

Substituting Eq. (2.57) into Eq. (2.68) and solving for u_a

$$u_a(t) = P'^{-1}\left[\frac{F_{ram}(t) - F_{fric}\,\mathrm{sgn}(u_p)}{A_p l_p(t)}\right] \tag{2.69}$$

Substituting Eq. (2.69) into Eq. (2.60)

$$\frac{dF_{ram}(t)}{dt} = \frac{\left[F_{ram}(t) - F_{fric}\,\mathrm{sgn}(u_p) + A_p p_{atm}\right]^2}{A_p p_a(0) l_0}$$

$$\cdot \left\{ u_p(t) - P'^{-1}\left[\frac{F_{ram}(t) - F_{fric}\,\mathrm{sgn}(u_p)}{A_p l_p(t)}\right] \right\} \tag{2.70}$$

It is assumed that the air bubble has volume V_a and enters the nozzle at time t_0. Since the

air bubble volume is assumed to be small relative to the total volume of air trapped in the

paste, the air bubble volume change can be neglected while it goes through the nozzle,

and $l_p(t)$ is

$$l_p(t) = \begin{cases} l_n - \dfrac{r_p^2}{r_n^2}\displaystyle\int_{t_0}^{t} u_a(\varepsilon)\,ds & \pi r_p^2 \displaystyle\int_{t_0}^{t} u_a(\varepsilon)\,d\varepsilon \le V_a \\[2em] l_n - \dfrac{V_a}{\pi r_n^2} & V_a < \pi r_p^2 \displaystyle\int_{t_0}^{t} u_a(\varepsilon)\,d\varepsilon \le \pi r_n^2 l_n \\[2em] \dfrac{r_p^2}{r_n^2}\displaystyle\int_{t_0}^{t} u_a(\varepsilon)\,d\varepsilon - \dfrac{V_a}{\pi r_n^2} & \pi r_n^2 l_n < \pi r_p^2 \displaystyle\int_{t_0}^{t} u_a(\varepsilon)\,d\varepsilon \le \pi r_n^2 l_n + V_a \end{cases} \tag{2.71}$$

Equation (2.71) describes the three phases of air bubble release. In the first phase,

the air bubble enters the nozzle with part of its volume outside of the barrel. In this phase

the length of paste in the nozzle will decrease. In the second phase, the air bubble has fully entered the nozzle. In this phase the length of paste in the nozzle is constant since the air bubble volume is assumed to be constant. In the third phase, the air bubble has reached the end of nozzle and starts to release. In this phase the length of paste in the nozzle will increase until the nozzle is completely filled with paste, assuming another air bubble is not directly behind the previous air bubble.

Figure 2.3. Air bubble release schematic.

3. EXTRUSION PROCESS MODELING FOR AQUEOUS-BASED CERAMIC PASTES, PART 2: EXPERIMENTAL VERIFICATION

3.1. EXTRUDER GEOMETRY

Two types of extruders were used in this study; one is a capillary rheometer used to characterize paste viscosity and the other is a single extruder used to fabricate parts. These extruders can be modeled as pipes. The assumptions and boundary conditions used to develop the steady-state and dynamic extrusion force models are discussed in Section 2.

The geometric model of the capillary rheometer used for viscosity measurement in this study is shown in Figure 3.1. The dimensions of this capillary rheometer are $l_p =$ 60 mm, $r_n = 0.55$ mm, and $r_p = 4.78$ mm. The capillary rheometer includes a barrel with a large diameter to hold the paste and a die with a small diameter where the pressure drop rate is dominating. To minimize the effect of flow channel cross section change, two different diameter dies, denoted die 1 ($l_n = 20$ mm) and die 2 ($l_n = 10$ mm), were used in this study. After determining the paste viscosity parameters, another ram extruder, which is used to fabricate parts, was employed to validate the constitutive model created in Section 2. The geometric model of the ram extruder is shown in Figure 3.2. The ram extruder includes a barrel to hold the paste, a throat to connect the nozzle with the barrel, and a nozzle with a small diameter. The dimensions of this ram extruder are $l_p = 120$ mm, $l_q = 98$ mm, $l_t = 15.2$ mm, $l_n = 11.5$ mm, $r_p = 15.1$ mm, $r_q = 2.5$ mm, $r_t = 2.4$ mm, and $r_n = 0.290$ mm.

Figure 3.1. Capillary rheometer geometric model.
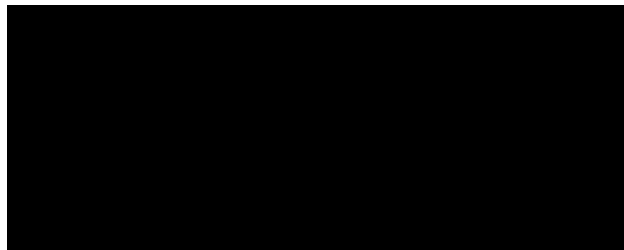
Figure 3.2. Ram extruder geometric model.

3.2. EXPERIMENTAL SETUP

A series of extrusion studies were conducted to validate the steady-state and transient responses predicted by the extrusion force models. In order to predict the extrusion force, the paste viscosity was obtained by conducting a set of experiments using the capillary rheometer depicted in Figure 3.1. After determining the paste viscosity, a series of experiments were conducted using the single extruder depicted in Figure 3.2 to validate the steady-state model. The dynamic responses obtained from these experiments were used to validate the constitutive model and the predicted effect of air bubble release.

In these experiments, Kollmorgen servomotors (AKM23D-EFCNR-00 for the capillary rheometer, AKM23D-EFBNR-00 for the single extruder) were used to drive the

rams. Load cells (Omega Engineering model LC-305-25 for the capillary rheometer, Omega Engineering model LC-305-1k for the single extruder) were used to measure the extrusion force. The load cells have ± 0.11 N and ± 4.5 N resolutions for the capillary rheometer and single extruder, respectively. The load cell signals were sent to amplifiers that increase the differential voltage signals by a factor of 50. The signals were then read by a National Instruments PXI-6025E multifunction board. National Instruments Labview software was utilized to control the ram velocity and record the ram velocity and extrusion force data with a sample period of 10 ms. When the ram is pushing the plunger, the ram velocity is also the plunger velocity, otherwise the plunger velocity is zero. The experimental systems are shown in Figures 3.3 and 3.4.
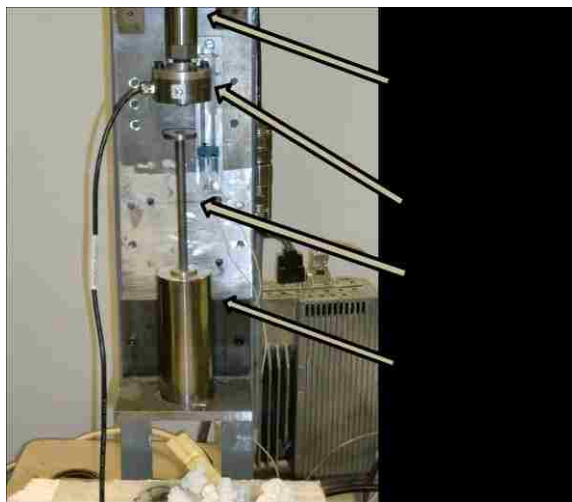
Figure 3.3. Capillary rheometer experimental system.
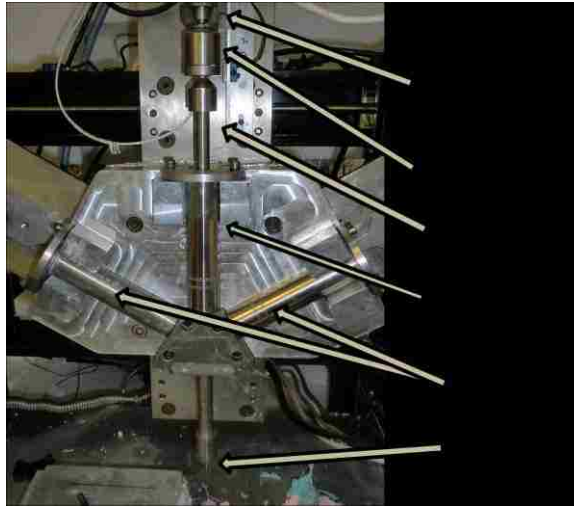
Figure 3.4. Single ram extruder experimental system.

Each test consisted of three extrusion experiments, two without paste and one with paste. The first experiment was conducted without paste at a constant ram velocity of 0.25 mm/s to test whether the barrel and plunger were well lubricated. The second experiment was conducted without paste using the same ram velocity that was to be used in the third experiment, which was later conducted with paste. The second experiment was used to determine the friction between the barrel and the plunger. The third experiment was used to gather the paste extrusion data. When multiple velocities were used in the third experiment, friction tests were conducted separately for each velocity. The experimental data showed that the wall friction in the capillary rheometer varied between 1 and 4 N, and the friction in the single extruder varied between 20 and 70 N.

3.3. VISCOSITY MODEL

In order to determine the paste viscosity model parameters, several batches of 45% solids loading Al_2O_3 paste were tested using the capillary rheometer depicted in Figure 3.1. Each batch was made using the same procedure. Forty-two tests were conducted to measure the extrusion force. For each test, a constant ram velocity was applied and the extrusion force was recorded. For each extrusion test record, the steady-state section of the response was selected and the average extrusion force was calculated as the steady-state extrusion force for the corresponding plunger velocity. The Herschel-Bulkley model parameters was then identified using the steady-state extrusion forces and their corresponding plunger velocities.

The pressure drop in the capillary rheometer barrel can be neglected; therefore, the extrusion force model for the capillary rheometer is

$$F_{ram}\left(u_p\right) = \pi r_p^2 l_n P'\left(n,\ \kappa,\ \sigma_0,\ \dot{\gamma}_c,\ r_n,\ \frac{r_p^2}{r_n^2}u_p\right) \tag{3.1}$$

The corresponding pressure drop rate model is

$$P'\left(n,\ \kappa,\ \sigma_0,\ \dot{\gamma}_c,\ r_n,\ \frac{r_p^2}{r_n^2}u_p\right) = \frac{F_{ram}\left(u_p\right)}{\pi r_p^2 l_n} \tag{3.2}$$

Since the two capillary rheometer dies have the same radius, the parameter values in Eq. (3.2) are the same. Least squares regression of the pressure drop rate model with the experimental data was conducted using the *nlinfit* function in MATLAB, which is based on the Levenberg-Marquardt algorithm for nonlinear least squares [29]. The calculated viscosity model parameters are $n = 0.437$, $\kappa = 67.1$ kg/m·s, $\sigma_0 = 249$ Pa and $\dot{\gamma}_c = 33.6$ s^{-1}. The pressure drop rate model has a correlation coefficient of 0.991 and a root mean

squared error of 2.04 MPa/m. This pressure drop is relatively small in comparison with the average pressure drop rate of 20.6 MPa/m, illustrating that the model fits the data very well. The pressure drop rate model is correlated with the experimental results in Figure 3.5, and the extrusion force models fit to experimental results for the two dies in Figure 3.6. It is seen that the extrusion force increases with an increase in plunger velocity; however, the extrusion force increases slowly as the plunger velocity increases, indicating that the paste has a shear thinning property. For the same ram velocity, the extrusion force varies due to batch variation, paste inhomogeneity in the same batch, and variation in the wall friction.
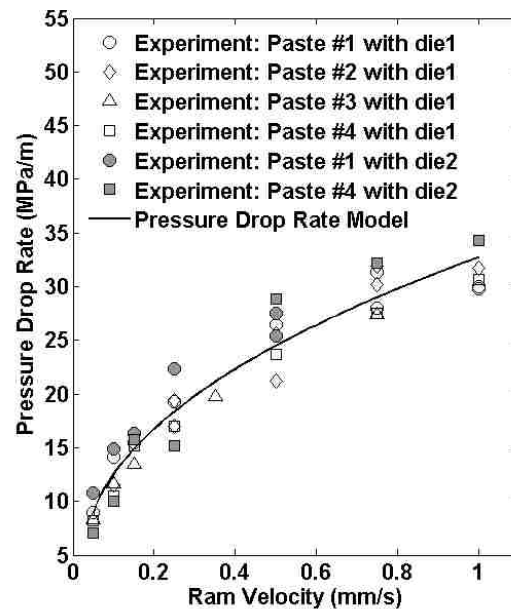
Figure 3.5. Experimental pressure drop rate data and model for capillary rheometer system.
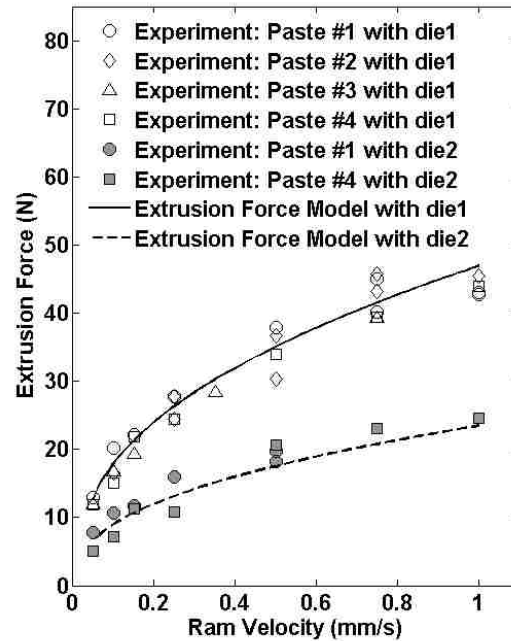
Figure 3.6. Experimental extrusion force data and model for capillary rheometer system.

3.4. STEADY-STATE EXTRUSION FORCE VALIDATION RESULTS

Tests were conducted using the single ram extruder to experimentally verify the steady-state component of the extrusion force model. The viscosity model parameters in Section 3.3 were used in the mathematical model, i.e., Eq. (2.41), to predict the extrusion force. The comparison between the analytical model predictions and experimental results is shown in Figure 3.7. It is seen that good agreement is obtained between experimental and simulation results, especially for paste #3, which was used to calibrate the viscosity model parameters. Due to the inconsistency of paste and the variation of wall friction, the extrusion force can vary by more than 100 N from batch to batch.
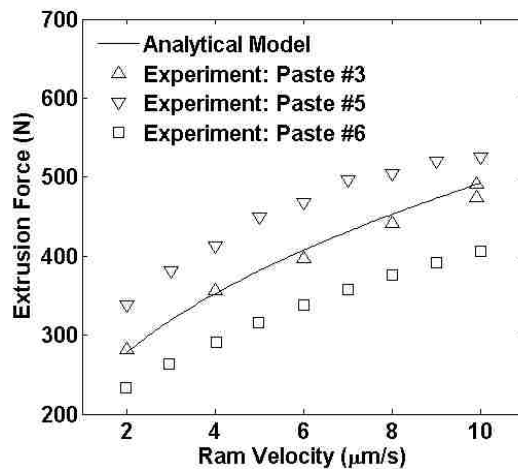
Figure 3.7. Steady-state extrusion forces obtained analytically and experimentally on single extruder system.

3.5. DYNAMIC RESPONSE RESULTS

To predict the extrusion force dynamic response using the developed analytical model, the air volume fraction must be known. However, the air volume fraction in the paste is difficult to measure in practice and varies significantly between different batches of paste. Therefore, the dynamic response varies significantly between different extrusion experiments. The capillary rheometer was given a set of constant ram velocities as shown in Figure 3.8. According to the dynamic model in Section 2.3, the dynamic response settling time is a function of initial air layer thickness and extrusion force. Therefore, the dynamic response of one transient phase (in this case between 288 and 381 s in Figure 3.8) is used to identify the air volume fraction. The parameter $p_a(0)$ is set to 1 atm, i.e., 0.1 MPa, and the initial air layer thickness is adjusted until the simulation results match well with the experimental results of the selected transient phase. In this case, the initial air layer thickness is indentified to be 8.5 mm. This value is verified by the large air

bubble release occurring at 450 s. The large air bubble release lasted approximately 8 s and the ram velocity was 0.25 mm/s; therefore, the compressed air layer thickness was approximately 2 mm. When the large air bubble started to release, the extrusion force was approximately 23 N. Based on the ideal gas law

$$A_p l_a(t)\left[\frac{F_{ram}(t)}{A_p} + p_{atm}\right] = A_p l_0 p_a(0) \tag{3.3}$$

and applying the fact that the plunger cross sectional area is approximately 7.2×10^{-5} m^2, the initial air layer thickness is calculated as approximately 8.4 mm. With the identified air layer thickness, the extrusion force dynamic model is simulated for the ram velocity profile in Figure 3.8 and compared with the experimental results. The friction, identified by experiments conducted for this test, is considered as a constant with the value of 1.5 N. The mean absolute percent error for the entire extrusion process (between 30 to 643 s) is 7.2%, illustrating good agreement obtained between the experimental and simulated responses. However, the mean absolute percent error is not equally distributed in each section. The mean absolute percent error is 5.8% for the first section (between 30 to 288 s), 0.83% for the second section (between 288 to 381 s), 0.56% for the third section (between 381 to 445 s), 8.3% for the forth section (between 445 to 502 s), 2.3% for the fifth section (between 502 to 538 s), 11.4% for the sixth section (between 538 to 597 s) and 2.8% for the seventh section (between 597 to 630 s). The error in the sixth section is mainly caused by paste inhomogeneity, since it has the same ram velocity as in the first section and, thus, is supposed to have the same steady-state extrusion force as in the first section.
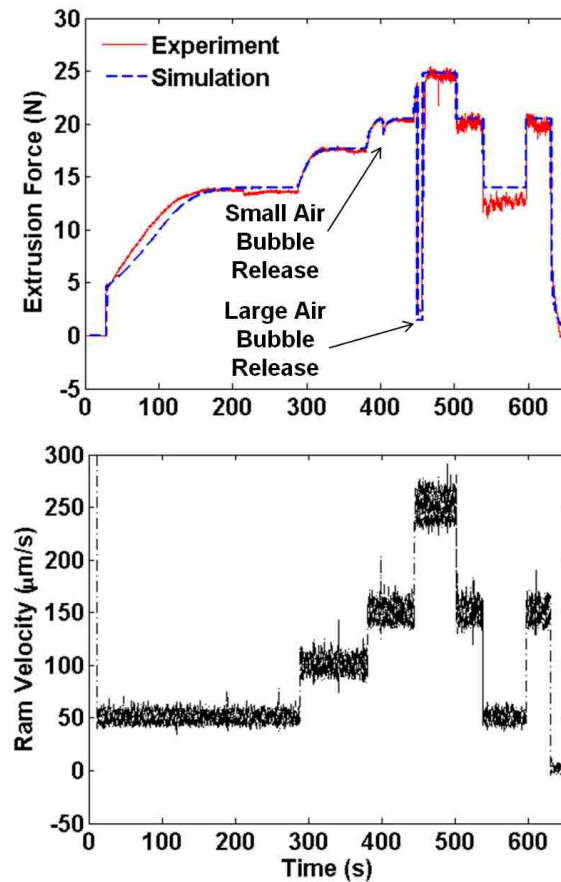
Figure 3.8. Experimental and simulation dynamic extrusion force responses with corresponding ram velocity for test conducted on capillary rheometer system.

It can be observed that after the large air bubble release, the transient response has a much shorter settling time compared with the settling time before the large air bubble release, confirming that paste compressibility is mainly due to the air trapped in the paste. As mentioned earlier, larger extrusion forces lead to shorter settling times. As seen in Figure 3.8, when extrusion starts (at 30 s), the 10% settling time is very long, approximately 89.2 s. As the extrusion force increases, the 10% settling time becomes shorter. When the ram velocity changes the first time (between 287 to 388 s), the 10%

settling time is approximately 19.6 s and when the ram velocity changes the second time (between 388 to 445 s), the 10% settling time is only approximately 10.1 s.

The dynamic response simulation for the single extruder was also conducted. The simulation and experimental results are shown in Figure 3.9. In this case, the initial air layer thickness is estimated to be approximately 0.9 mm based on the dynamic response when the ram velocity changes the first time (between 3840 to 4031 s).
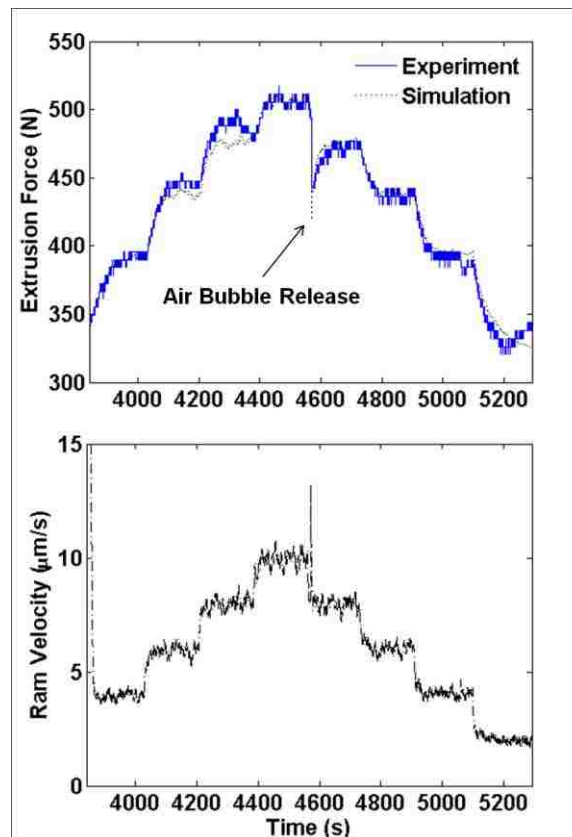
Figure 3.9. Experimental and simulation dynamic extrusion force responses and corresponding ram velocity for the test conducted on single extruder system.

The mean absolute percent error between the experimental and simulated responses for the entire extrusion process is 6.3%, indicating good agreement between the two responses. The differences between the experimental and simulated results in the third section are mainly caused by the paste inhomogeneity, and the difference between experimental and simulated results towards the end of the test is caused by paste clogging in the nozzle.

3.6. PRE-LOADING ANALYSIS

When loading the paste into the extruder barrel, the plunger is typically inserted into the barrel with a higher velocity than normal extrusion process. During this process, referred to as "pre-loading," the paste is compressed to a high pressure state, causing the starting extrusion force to be much larger than the friction. With different initial pressures, the initial dynamic responses can be very different. The dynamic response of the extrusion force is typically dominated by a first-order response as shown in Figures 3.8 and 3.9; however, the dynamic response can also be dominated by an apparent quadratic response when the initial extrusion force is small. A series of simulations with different initial extrusion forces were conducted and the results are compared with the corresponding experimental results in Figure 3.10. In this case, the initial air layer thickness is 14.5 mm. The mean absolute percent error between a simulation conducted with $F_{ram}(0) = 4.1$ N, which is the initial experimental extrusion force, and the experiment for the entire extrusion process (between 23 to 44 s) is 4.3%, indicating good agreement between the experimental and simulated responses.
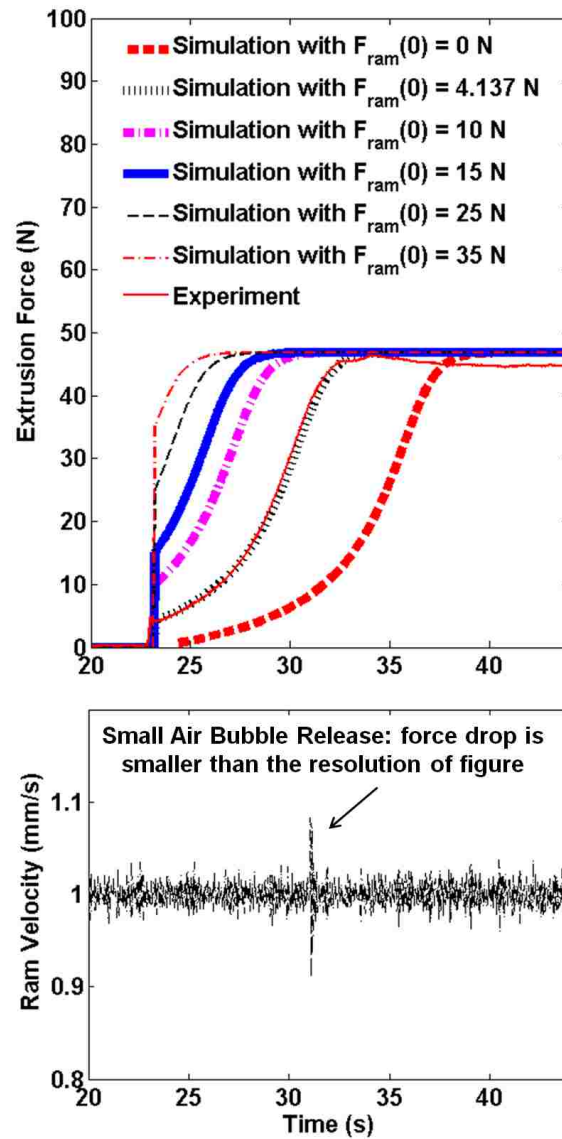
Figure 3.10. Simulated dynamic extrusion force responses with different initial values and corresponding ram velocity compared with experimental results obtained from capillary rheometer system.

When the initial extrusion force is small, the dynamic response is dominated by a response that appears quadratic and, when the initial extrusion force becomes larger, the dynamic response is dominated by a first-order response. Based on Eqs. (2.66) and (2.67)

derived from the linearization analysis, the time constant and gain for the extrusion process with alumina paste and the capillary rheometer with die 1 geometry is plotted versus extrusion force and ram velocity in Figures 3.11 and 3.12, the air amount used to calculate time constant is the same as in experiment conducted in Figure 3.10. It is seen that as the extrusion force increases, the time constant and gain decrease as discussed in Section 2.3. When the extrusion force goes from some low value to a higher value, the corresponding time constant decreases rapidly, giving the dynamic response an apparent quadratic response. This quadratic response is actually composed by a series of first-order responses, like depicted in Figure 3.13. When the extrusion force is larger than 30 N, the time constant decreases slowly and the dynamic response is then dominated by a first-order response, as described by Eq. (2.63).

Because the steady-state extrusion force model is described by Eqs. (2.40) and (2.33) before and after the critical shear rate occurs, respectively, the trends of time constant and gain are also different before and after the critical shear rate occurs. Both of the time constant and gain decreases as the extrusion force increases; however, the decreasing rate are different before and after the critical shear rate occurs. Before the critical shear rate occurs, the decreasing rate of time constant slightly increases as the extrusion force increases, and the decreasing rate of gain significantly increases as the extrusion force increases. After the critical shear rate occurs, the decreasing rate of time constant and gain both decrease as the extrusion force increases.
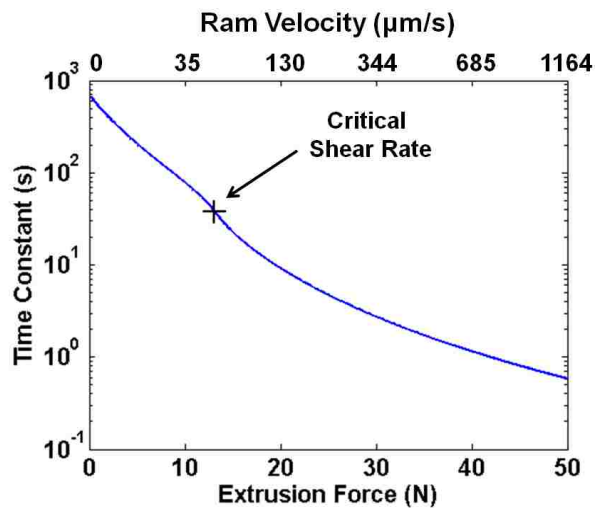
Figure 3.11. Time constant in capillary rheometer system as a function of extrusion force and ram velocity.
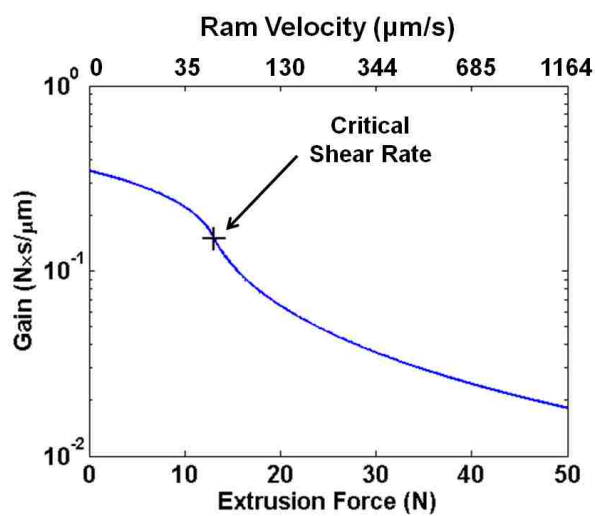
Figure 3.12. Gain in capillary rheometer system as a function of extrusion force and ram velocity.
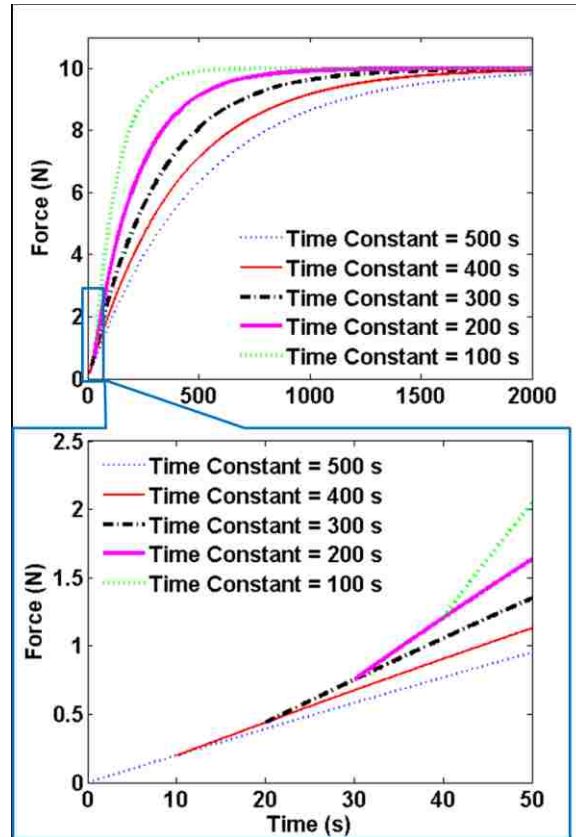
Figure 3.13. An apparent quadratic response composed by a series of first-order responses with decreasing time constants.

3.7. AIR BUBBLE RELEASE ANALYSIS

Similar to the amount of air trapped in the paste, the volume of air during an air bubble release is also difficult to measure. To study the air bubble release process, a series of simulations were conducted with different volumes of released air for the ram velocity profile in an experiment on the capillary rheometer where air bubble release occurred. The results are shown in Figure 3.14. The simulation with an air bubble volume that is 30% of the nozzle volume is close to the experimental results. The air bubble release simulation for the single extruder system was also conducted, and the simulation

results were compared with the experimental results in Figure 3.15. In this case, an air

bubble volume of 85% of the nozzle volume is close to the experimental result.
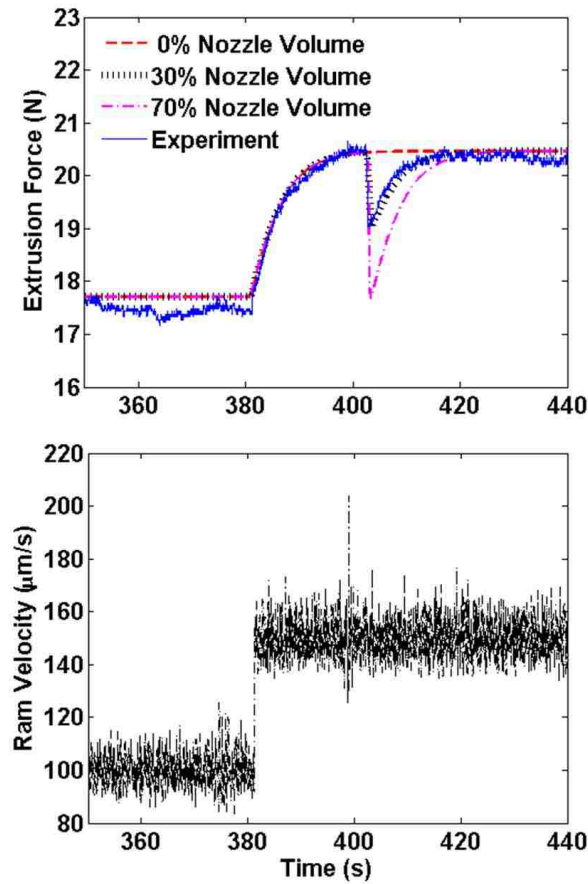
Figure 3.14. Extrusion force responses on capillary rheometer with different volumes of air bubble release.

As seen in Figures 3.14 and 3.15, when the air bubble release starts, the extrusion

force will drop dramatically, the magnitude of which depends on the air bubble size. The

larger the volume of air released, the larger the extrusion force drop. Because of the

sudden extrusion force drop, the motor will generate a large velocity peak, as seen in Figures 3.14 and 3.15. After the air bubble is totally released, the nozzle is filled by paste again, and then the extrusion force increases as described by the constitutive law of the extrusion process. With proper air bubble volume, the simulation results fit the experimental results very well, thus the model built in Section 2.4 can be used to describe the air bubble release process.
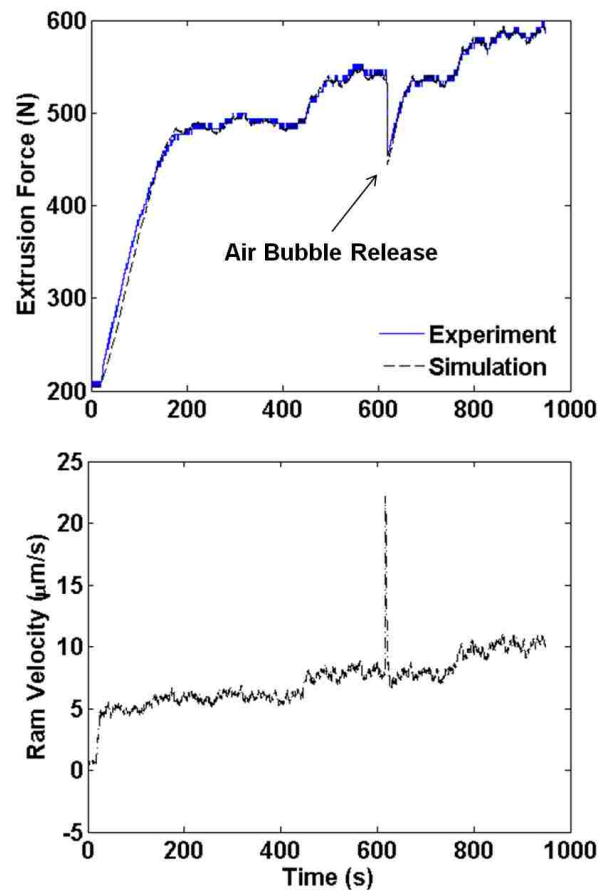
Figure 3.15. Extrusion force responses on single extruder system with an air bubble release.

3.8. SUMMARY AND CONCLUSIONS OF EXTRUSION PROCESS MODELING FOR AQUEOUS-BASED CERAMIC PASTES

A dynamic extrusion force constitutive model was developed to describe the relationship between the plunger velocity and the extrusion force in the extrusion of aqueous-based ceramic paste. A modified Herschel-Bulkley model was used to describe the viscosity of aqueous-based ceramic paste. The steady-state component of the constitutive model was then developed based on the Navier-Stokes equation. Because of the compressibility introduced by the trapped air, the extrusion force dynamic was described by a first-order nonlinear differential equation using plunger velocity as an input. The settling time depends on the amount of air trapped in the paste and the magnitude of the extrusion force. As more air is trapped in the paste, the settling time increases; as the extrusion force increases, the settling time and gain both decrease. The dynamics that occur during air bubble release, which causes a sudden drop in the extrusion force due to the change of the volume of paste in the nozzle, can be described by the developed constitutive model.

A series of experimental and numerical studies were conducted to verify the developed constitutive model. A capillary rheometer was used to determine the viscosity model parameters, which were then used for the prediction of extrusion forces in a single extruder system. Extrusion experiments were also conducted in this single extruder system, and a good agreement was obtained between the predicted and measured extrusion forces. The extrusion experiments conducted on the capillary rheometer and on the single extruder system proved that the large settling time is mainly caused by the air trapped in the paste and the change of settling time also depends on the extrusion force. As the extrusion force increases from a small value, the settling time decreases rapidly,

giving the dynamic response the appearance of a quadratic response. When the extrusion force is large, the settling time changes slowly, thus, the dynamic response is dominated by a first-order response. Air bubble release was studied by a series of simulations, which showed that the magnitude of drop in the extrusion force depends on the air bubble volume. Experimental and simulation results were compared for the dynamic response models of extrusion process and air bubble release. Good agreements were obtained in all of the experimental and simulation comparisons, suggesting that the constitutive model can be used to predict the steady-state and transient extrusion force responses, as well as to describe the air bubble release phenomenon in aqueous-based extrusion of ceramic paste.

4. MODELING, ANALYSIS AND SIMULATION OF PASTE FREEZING IN FREEZE-FORM EXTRUSION FABRICATION OF THIN-WALL PARTS

4.1. 3D ENERGY GOVERNING EQUATION

The 3D energy governing equation is [30]

$$\frac{\partial(\rho H)}{\partial t} = \nabla \cdot (k \nabla T) + \dot{S} \tag{4.1}$$

where T (°C), ρ (kg/m^3), k (W/m·°C) and H (J/kg) are the material temperature, density, thermal conductivity, and enthalpy, respectively, and $\dot{S}$ (W/m^3) is the volumetric rate of heat generation or absorption. The enthalpy can be written as

$$H = H_{ref} + \int_{T_{ref}}^{T} c\, dT + \Delta H \tag{4.2}$$

where c (J/kg·°C) is the material specific heat, and the subscript ref denotes the reference condition. Here, the absolute zero temperature is selected as the reference condition. The enthalpy correction, which depends upon the material phase, is

$$\Delta H = \chi L \tag{4.3}$$

where χ is the material's liquid fraction and L (J/kg) is the material's latent heat. The convection boundary constraint is

$$-k \nabla T \cdot \mathbf{n} = h(T - T_{\infty}) \tag{4.4}$$

where T_{∞} (°C) is the ambient temperature, h (W/m^2·°C) is the convection coefficient, and $\mathbf{n}$ is the normal vector to the boundary surface.

4.2. MATERIAL PROPERTIES

The paste is composed primarily of ceramic particles and water, with only trace amounts (1-4 vol.%) of organic binder. Therefore, the paste's properties can be estimated from the material properties of ceramic particles and water.

Typically, the solids loading (volume fraction of ceramic particles, denoted by v_e) of the paste is known. Thus, the volume fraction of water is

$$v_w = 1 - v_e \tag{4.5}$$

The mass fractions of ceramic particles and water, respectively, are

$$m_e = \frac{\rho_e v_e}{\rho_e v_e + \rho_w v_w} \tag{4.6}$$

$$m_w = \frac{\rho_w v_w}{\rho_e v_e + \rho_w v_w} \tag{4.7}$$

Since ceramic powder cannot be dissolved in water, the paste can be considered as a simple mixture of these two components. Therefore, the paste's density, specific heat, and latent heat, respectively, are

$$\rho_P = \rho_e v_e + \rho_w v_w \tag{4.8}$$

$$c_P = c_e m_e + c_w m_w \tag{4.9}$$

$$L_P = L_w m_w \tag{4.10}$$

When the paste is frozen, the properties of ice instead of water should be used in Eqs. (4.9) and (4.11).

The estimation of thermal conductivity is more complex. There are numerous papers studying the thermal conductivity of two-phase mixtures, which can be classified into several different conditions [31]. The law of mixtures can be used to estimate paste thermal conductivity

$$k_P = k_e v_e + k_w v_w \tag{4.11}$$

However, due to the high solids loading of the paste used in this study (45-65 vol.%), it can be assumed that the two phases (i.e., ceramic particles and water) have similar distributions. Therefore, the General Effective Medium Theory (GEMT) [32] is used to estimate the paste thermal conductivity

$$k_P = \text{GEMT}\left(k_e, k_w, v_e, v_w\right)$$

$$= \frac{\left(3v_e - 1\right)k_e + \left(3v_w - 1\right)k_w + \left\{\left[\left(3v_e - 1\right)k_e + \left(3v_w - 1\right)k_w\right]^2 + 8k_e k_w\right\}^{\frac{1}{2}}}{4} \tag{4.12}$$

where v is volume fraction, and the subscripts P, w, and e denote paste, water, and ceramic, respectively.

A possible source of error in this calculation is that the binder and dispersant may accumulate on the surface of ceramic particles, changing the paste's effective thermal conductivity. The binder and the dispersant have smaller thermal conductivities (~0.02 W/m·°C) than the ceramic particles and the water; therefore, a thin binder and dispersant film between the ceramic particles and the water may significantly decrease the paste thermal conductivity. Since the binder and the dispersant are assumed to accumulate on the surface of the ceramic particles, they have the same distribution as the ceramic particles and, thus, the effective thermal conductivity of the mixture of ceramic particles, binder, and dispersant is

$$k_u = \text{GEMT}\left(k_e, k_b, \frac{v_e}{v_e + v_b}, \frac{v_b}{v_e + v_b}\right) \tag{4.13}$$

where the subscript b denotes binder plus dispersant. In this case, the paste thermal conductivity is

$$k_P^* = \text{GEMT}\left(k_u, k_{w,} v_e, v_w\right) \tag{4.14}$$

For the cases studied in this paper, the volume fraction of binder and dispersant together is less than 4%. It can be shown that the thermal conductivity error (i.e., $\left|k_P - k_P^*\right|/k_P^*$) is less than 4% and the critical freezing time error is less than 2%. Since the distribution of binder and dispersant can be very complex and the error is small, the effect of binder and dispersant on paste thermal conductivity in this study is neglected. The paste thermal conductivities used in Section 4 will be computed via Eq. (4.11), the paste thermal conductivities used in Section 5 will be computed via Eq. (4.12).

4.3. CONVECTION COEFFICIENT

When the air flow surrounding the part is not forced but due to buoyancy, the convection is natural convection. In this case, the convection coefficient is [33]

$$h = \left\{0.825 + \frac{0.387\text{Ra}^{1/6}}{\left[1 + \left(0.492/\text{Pr}\right)^{9/16}\right]^{8/27}}\right\} \frac{k_\infty}{D} \tag{4.15}$$

where D (m) is the part's effective dimension, which is part height under natural convection, k_∞ (W/m·°C) is the thermal conductivity of air, Pr is the Prandtl number for air, and Ra is the Rayleigh number

$$\mathrm{Ra} = \frac{g\beta(T - T_\infty)D^3}{v_\infty^2}\mathrm{Pr} \tag{4.16}$$

where β (1/K) is the coefficient of volume expansion, which is considered to be $1/(T + 273.15)$ for air, and v_∞ (m²/s) is the kinematic viscosity of air. For the various part sizes, part temperatures, and ambient temperatures considered in this study, the average convection coefficient is 6.7 W/m²·°C.

When the air is forced (e.g., blown by a fan), the convection is forced convection, which is determined by not only the flow condition but also the part shape. When cylinder parts are fabricated, the convection coefficient is [33]

$$h = \left(C\,\mathrm{Re}^n\,\mathrm{Pr}^{\frac{1}{3}}\right)\frac{k_\infty}{D} \tag{4.17}$$

where effective dimension D is the part's diameter and Re is air's Reynolds number. The coefficients C and n as functions of Reynolds number are given in Table 4.1 [33]. When hollow square parts are fabricated and one of its faces is perpendicular to the air flow, the convection condition is [33]

$$h = \left(0.102\,\mathrm{Re}^{0.675}\,\mathrm{Pr}^{\frac{1}{3}}\right)\frac{k_\infty}{D} \tag{4.18}$$

where effective dimension D is the side length for square parts in this case. The fan used for the experiments conducted in this study blew the air with a speed of approximately 3 m/s. For the various part sizes and shapes considered in the simulation, the average convection coefficient is 35 W/m²·°C.

Table 4.1. The values of C and n.

Re	C	n
0.4~4	0.989	0.330
4~40	0.911	0.385
40~400	0.683	0.385
4×10^3~4×10^4	0.193	0.618
4×10^4~4×10^5	0.0266	0.805

4.4. 3D FINITE ELEMENT SIMULATION SETUP

Simulations of a thin wall were conducted with the commercial software FLUENT 12. In these simulations, dynamic meshing was applied to simulate continuous paste deposition. The simulation schematic with boundary conditions is shown in Figure 4.1. A vertical monitor surface was created inside the wall, as depicted in the figure. The maximum temperature on this monitor surface was recorded for each time step. When the newly deposited paste moved through this monitor surface, the surface's maximum temperature increased to the initial paste temperature, and the time at which this occurred was recorded. When the maximum temperature of the monitor surface dropped just below 0 °C, the time was also recorded. The difference between these two times was taken to be the layer freezing time.

The boundary conditions used in the simulations are as follows:

(1) The bottom of the first layer was set to a constant temperature, which was the ambient temperature.

(2) All other surfaces had the convection heat transfer constraint shown in Figure 4.1.
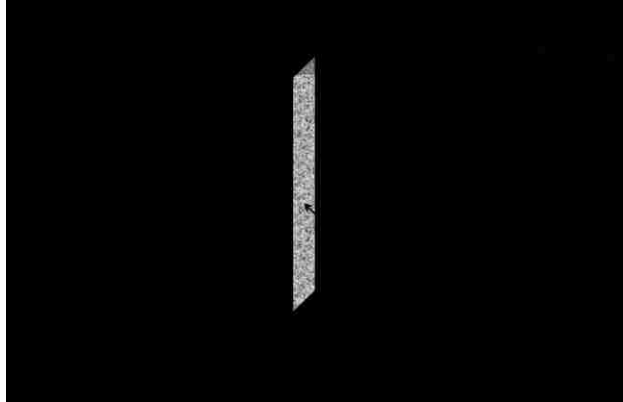
Figure 4.1. 3D simulation schematic with dynamic meshing and boundary conditions.

4.4.1. Assumptions. For the finite element analysis and simulation, the following assumptions were made:

(1) In the FEF process, a metal substrate much larger than the part was used; therefore, the substrate's temperature was considered to be constant and equal to the ambient temperature.

(2) The convection coefficient may change due to the change of air flow around the part, which is complex and difficult to model. Thus, in order to analyze the effect of convection and simplify the simulation, the convection coefficient was considered to be constant on each surface during the part fabrication process.

(3) The paste density was considered to be constant during the paste freezing process. Since water's volume expands by approximately 9% when frozen, the 45% solids loading paste's volume expansion rate is approximately 5% and, thus, the linear expansion rate is approximately 1.6%.

(4) Water is the component of the paste which actually freezes, thus the paste freezes at the freezing temperature of water, i.e., 0 °C.

4.4.2. Paste Properties. Materials used in the FEF process study included zirconia (ZrO_2), zirconium carbide (ZrC), alumina (Al_2O_3) and tungsten (W). The estimated material properties of these pastes with 45% solids loading are listed in Table 4.2. The solids loadings used in the FEF process are typically larger than 35%, and may be up to 65%. The estimated material properties of Al_2O_3 paste with various solids loadings are listed in Table 4.3.

Table 4.2. Estimated material properties of pastes with 45% solids loading used for simulations conducted in this paper.

Paste material	ZrO_2	ZrC	Al_2O_3	W
Density (kg/m^3)	3025	3579	2350	9235
Thermal conductivity when not frozen (W/m·°C)	1.2	5.6	19.7	78.2
Specific heat when not frozen (J/kg·°C)	1102	1087	1653	371.3
Latent heat (10^4J/kg)	6.07	5.13	7.82	1.99
Thermal conductivity when frozen (W/m·°C)	2.0	6.3	20.5	79.0
Specific heat when frozen (J/kg·°C)	725.6	768.6	1168	247.9

Table 4.3. Estimated material properties of Al_2O_3 pastes with various solids loadings used for simulations conducted in this paper.

Solids loadings	35%	45%	55%	65%
Density (kg/m^3)	2050	2350	2650	2950
Thermal conductivity when not frozen (W/m·°C)	15.5	19.7	24.0	28.2
Specific heat when not frozen (J/kg·°C)	1927	1653	1441	1272
Latent heat (10^4J/kg)	10.6	7.82	5.67	3.96
Thermal conductivity when frozen (W/m·°C)	16.4	20.5	24.6	28.7
Specific heat when frozen (J/kg·°C)	1270	1168	1089	1026

4.5. 1D MODEL SIMPLIFICATION

FLUENT's dynamic mesh feature is powerful for simulation of the paste deposition process; however, it also generates a large number of nodes for the simulation, and may take weeks or even months to conduct one single simulation. A more efficient 1-D simulation model was thus introduced in this study.

4.5.1. Theory. The FLUENT simulations showed that, for a thin-wall part, the temperature gradient along deposition and width directions are typically near zero. Therefore, the temperature gradient in the two directions parallel to the substrate can be neglected, and Eq. (4.1) reduces to

$$\rho \frac{\partial H}{\partial t} = \frac{\partial}{\partial z} \left(k \frac{\partial T}{\partial z} \right) + \dot{S} \tag{4.19}$$

where S is computed using the convection boundary condition

$$\dot{S} = -\frac{2h(T - T_\infty)}{\Delta y} \tag{4.20}$$

The term Δy (m) is the paste filament width. Combining Eqs. (4.19) and (4.20), and applying the chain rule leads to

$$\frac{\partial H}{\partial t} = \frac{\partial}{\partial z} \left(\frac{k}{\rho} \frac{\partial T}{\partial H} \frac{\partial H}{\partial z} \right) - \frac{2h(T - T_\infty)}{\rho \Delta y} \tag{4.21}$$

In Eq. (4.21), $\dfrac{k}{\rho} \dfrac{\partial T}{\partial H}$ and T both are functions of H. Let

$$\Gamma(H) = \frac{k}{\rho} \frac{\partial T}{\partial H} \tag{4.22}$$

$$\Theta(H) = -\frac{2h\left[T(H) - T_\infty\right]}{\rho \Delta y} \tag{4.23}$$

Then the implicit difference form of Eq. (4.21) can be written as

$$-\frac{\delta_t}{2\delta_z^2}\left[\Gamma\left(H_{i+1}^{n+1}\right)+\Gamma\left(H_i^{n+1}\right)\right]H_{i+1}^{n+1}$$

$$+\left\{1+\frac{\delta_t}{2\delta_z^2}\left[\Gamma\left(H_{i+1}^{n+1}\right)+2\Gamma\left(H_i^{n+1}\right)+\Gamma\left(H_{i-1}^{n+1}\right)\right]\right\}H_i^{n+1} \tag{4.24}$$

$$-\frac{\delta_t}{2\delta_z^2}\left[\Gamma\left(H_i^{n+1}\right)+\Gamma\left(H_{i-1}^{n+1}\right)\right]H_{i-1}^{n+1}=\delta_t\Theta\left(H_i^{n+1}\right)+H_i^n$$

4.5.2. Simulation Setup. The simplified 1D model was implemented in C++. In this simplified model, the mesh was vertical to the substrate. The simulation schematic with boundary conditions is shown in Figure 4.2. The maximum temperature of the entire mesh was recorded for each time step. When the new layer of paste was deposited, a new layer mesh block was added to the top of the existing mesh, the maximum temperature increased to the paste's initial temperature, and the time at which this occurred was recorded. When the maximum temperature dropped below 0 °C, the time was also recorded. The difference between these two times is the freezing time of this layer. The assumptions in Section 4.4.1 and the material properties in Section 4.4.2 were also applied to the simulations using the simplified 1D model.

Figure 4.2. Schematic of 1D model simulation with boundary conditions.

4.6. 3D VERSUS 1D SIMULATION

Eight factors that affect the paste freezing time in the FEF process were considered in this study. They are: (1) total time between layers (i.e., sum of the deposition time for the current layer and the dwell time between the current and next layers), (2) convection coefficient, (3) paste material, (4) paste solids loading, (5) initial paste temperature, (6) ambient temperature, (7) filament height, and (8) filament width.

Unless otherwise noted, Al_2O_3 paste with 45% solids loading was used as the extrusion material, the convection condition was forced, where the convection coefficient was considered as 35 $W/m^2 \cdot °C$, the initial paste temperature was 5 °C, the ambient temperature was -10 °C, the filament height and width were both 580 μm, and the total time between layers was 10 s. If the freezing time is smaller than the total time between layers, the paste is totally frozen and the part being fabricated is considered successfully built. If the freezing time is larger than the total time between layers, the paste is in a semiliquid state and the part being fabricated is under the risk of deforming or even collapsing.

Three test cases were conducted using both the commercial code ANSYS FLUENT 12 and the code developed by the authors based on the proposed 1D model. The setups of these cases are tuned to guarantee the results are independent of mesh density or node number, time step size and convergence criteria. The results of freezing time versus layer number are shown in Figure 4.3. The mean absolute percent error due to the 1D simplification for the entire curve are 7.05% for condition (a), 6.17% for condition (b) and 2.09% for condition (c); however, due to the large node number in the 3D cases, ANSYS FLUENT took about 20 days to obtain one curve for condition (a), while the 1D model code took only 10 min. Therefore, the proposed 1D model is much more efficient for computing the paste freezing time for thin-wall parts in the FEF process.
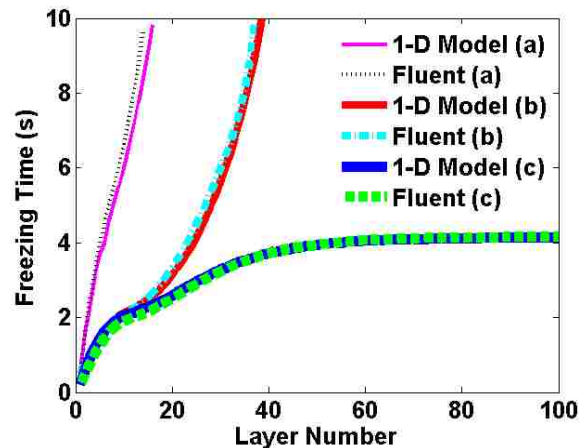
Figure 4.3. Paste freezing times obtained from simulations using FLUENT and the code based on the proposed 1D model with 45% solids loading, 5 °C initial paste temperature, −10 °C ambient temperature, 580 μm filament height and width, 10 s total time between layers, (a) ZrC paste material, and 35 W/m^2·°C convection coefficient (forced convection); (b) Al$_2$O$_3$ paste material, and 6.7 W/m^2·°C convection coefficient (natural convection); (c) Al$_2$O$_3$ paste material, and 35 W/m^2·°C convection coefficient (forced convection).

4.7. EFFECTS OF TOTAL TIME BETWEEN LAYERS ON PASTE FREEZING TIME

The total time between layers is the sum of the paste deposition time for a layer and the dwell time between layers. When the paste freezing time is shorter than the deposition time, dwell time is not required. However, if the freezing time is longer than the deposition time, dwell time is necessary to prevent the part from deforming or even collapsing. When the dwell time between layers increases, the temperature of the previously extruded paste will decrease, which will increase the temperature difference between the previously and newly deposited pastes; therefore, the freezing time of the next layer will decrease. However, the increase in dwell time will also increase the part build time, thus, decreasing fabrication productivity. The simulation results for different total times between layers are given in Figure 4.4.

Figure 4.4 shows that when the total time between layers is 5 s, the freezing time of the Al$_2$O$_3$ paste will increase more quickly after the 12th layer, and the paste will not be totally frozen after the 20th layer. When the total time between layers is 10 s, the freezing

time will increase more slowly with increasing layer number after the 10th layer, and the paste will be able to freeze regardless of how many layers of paste have been deposited. When the total time is 20 s, the freezing time is even shorter; however, the part build time will be longer.

Figures 4.4 and 4.5 show a typical pattern of paste freezing time: When the paste is near the substrate, the paste freezing time is short; however, as the part height increases, the paste freezing time increases, finally reaching a steady-state value. The steady-state value is useful for FEF process planning. If the planned total time between layers is larger than the steady-state freezing time, the part will always be totally frozen and will not deform or collapse.

The relationship between the steady-state freezing time and the total time between layers is studied using the 1D model for the other six parameters in Section 4.8. In this study, if the paste freezing time does not increase by more than 0.01 s for 15 consecutive layers, the freezing time is considered as the paste's steady-state freezing time.
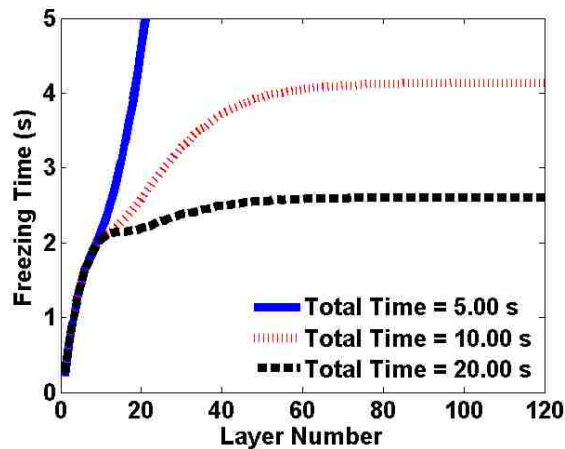
Figure 4.4. Paste freezing time for different total times between layers with Al_2O_3 paste, 45% solids loading, 35 $W/m^2 \cdot °C$ convection coefficient (forced convection), 5 °C initial paste temperature, −10 °C ambient temperature, and 580 μm filament height and width.

4.8. EFFECTS OF OTHER FACTORS ON PASTE FREEZING TIME

4.8.1. Convection Coefficient. A change in the convection coefficient will change the heat transfer rate between the paste and its surroundings, which affects the paste freezing time. When the convection coefficient increases, the paste freezing time decreases. The convection coefficient can be changed, for example, by using a fan to blow cool air over the extruded paste. As mentioned in Section 4.3, when the fan is off, the convection is considered as natural convection, and the average convection coefficient is 6.7 W/m$^2\cdot$°C. When the fan is on, the convection changes to forced convection, and the average convection coefficient is 35 W/m$^2\cdot$°C in this study. If the fan speed is adjusted or the part size is changed, other values of the convection coefficient can also be obtained.

The layer freezing time simulation results with natural and forced convection conditions are shown in Figure 4.5. Under natural convection, the paste freezing time increases exponentially after approximately 15 layers, and the paste is not totally frozen after 40 layers. In this case, a large part being fabricated will deform or even collapse. A similar condition also occurs when the convection coefficient is 15 W/m$^2\cdot$°C as the paste will not be totally frozen after 54 layers. When the convection coefficient increases to 25 or 35 W/m$^2\cdot$°C, the paste freezing time is shorter than the total time between layers, and it increases more slowly with respect to the increase in layer number. Therefore, the part will not collapse during the fabrication process regardless of how tall it is. At the beginning of the extrusion process, the freezing times for all convection conditions are similar. This is because when the paste layers are close to the substrate, the conduction heat transfer dominates, and the effect of convection is not significant. When the part height increases, the effect of convection becomes more and more dominant.

The simulation result for the steady-state freezing time vs. the total time between layers with different convection coefficients is shown in Figure 4.6. When the steady-state freezing time is smaller than the total time between layers, the paste will be totally frozen (shown in the frozen region in Figure 4.6). The "critical freezing time" is defined as the point where the steady-state freezing time equals to the total time between two successive layers. As the convection coefficient decreases, the heat transfer rate decreases; therefore, the critical freezing time increases. The relationship between the

critical freezing time and the convection coefficient is plotted in Figure 4.7. A power law was constructed using a nonlinear least squares algorithm to obtain the following relationship

$$t_c = 44.7h^{-0.505} \tag{4.25}$$

where t_c (s) is the critical freezing time. The power law in Eq. (4.25) has a correlation coefficient of 0.999 and a root-mean-square error of 0.125 s, indicating a nonlinear relationship between the critical freezing time and the convection coefficient. As the convection coefficient increases, the critical freezing time becomes smaller.
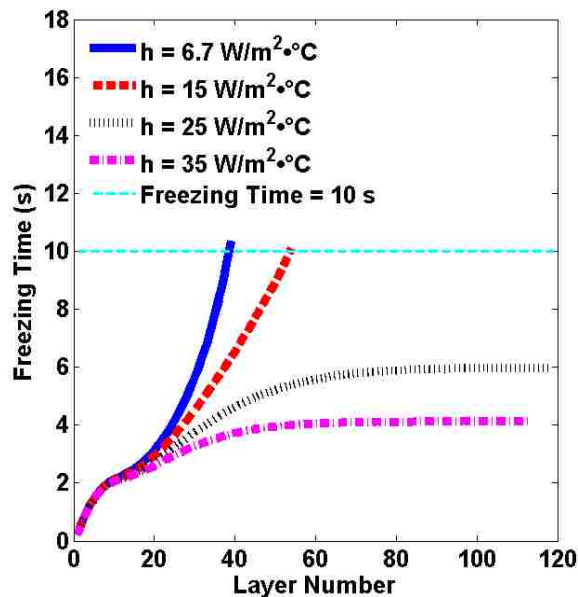
Figure 4.5. Paste freezing time for natural and forced convections with Al_2O_3 paste, 45% solids loading, 5 °C initial paste temperature, −10 °C ambient temperature, 580 μm filament height and width, and 10 s total time between layers.

Figure 4.6. Steady-state freezing time versus total time between layers for natural and forced convections with Al$_2$O$_3$ paste, 45% solids loading, 5 °C initial paste temperature, –10 °C ambient temperature, and 580 μm filament height and width.
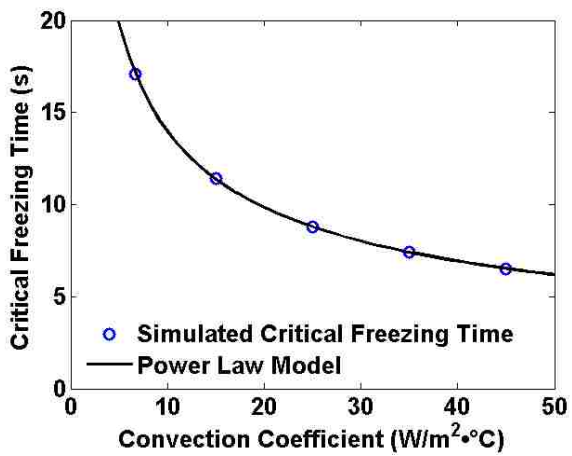
Figure 4.7. Simulated critical freezing time as a power law function of convection coefficient.

As shown in Figure 4.6, when the total time between layers decreases slightly from the critical freezing time, the steady-state freezing time increases drastically. This is because when one layer is not totally frozen, the freezing time of the next layer increases, leaving more semiliquid paste when the following layer is deposited; therefore, the freezing time of each successive layer will continue to increase rapidly, until it reaches a much larger steady-state freezing time, as shown in Figure 4.8. This phenomenon suggests that once one layer is not totally frozen, the semiliquid region will continue to expand, causing the part to deform or even collapse. Also, when the total time is close to the critical freezing time, the freezing time is very sensitive to any disturbance that may occur. Therefore, in planning the FEF process, a total time larger than the critical freezing time should be used to ensure the part does not deform or collapse during fabrication.
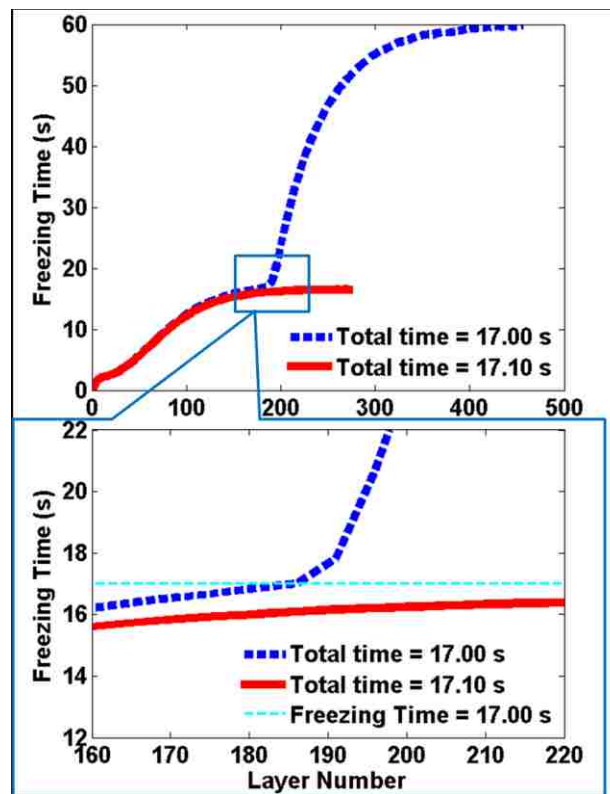
Figure 4.8. Paste freezing time for total times between layers of 17.00 and 17.10 s with Al$_2$O$_3$ paste, 45% solids loading, 6.7 W/m^2·°C convection coefficient (natural convection), 5 °C initial paste temperature, −10 °C ambient temperature, and 580 μm filament height and width.

4.8.2. Paste Material. The paste material may dramatically change the paste's properties, including the thermal conductivity and the specific heat. Any changes in these properties will change the heat transfer rate and, thus, the paste freezing time. The paste freezing time simulation results for ZrO_2, ZrC, Al_2O_3 and W pastes are shown in Figures 4.9 and 4.10. The ZrO_2 and ZrC pastes cannot totally freeze within 10 s after 4 and 16 layers, respectively, while the steady-state freezing times for the Al_2O_3 and W pastes are 4.1 and 1.1 s, respectively. The dramatic differences in the paste freezing times are due to the fact that the ZrO_2 and ZrC pastes' thermal conductivities, approximately 1.6 and 6 W/m·°C, respectively, are much lower than the Al_2O_3 paste's thermal conductivity (approximately 20 W/m·°C) and the W paste's thermal conductivity (approximately 79 W/m·°C).

To determine which property between the thermal conductivity and the specific heat is the more influential on the freezing time, the thermal conductivity of 45% solids loading Al_2O_3 paste is altered in the simulations. The relationship between the critical freezing time and the average thermal conductivity is plotted in Figure 4.11. The critical freezing times of Al_2O_3 pastes with various thermal conductivities are almost exactly the same as other pastes having the same thermal conductivities, indicating that the thermal conductivity is more influential on paste freezing time than the specific heat. A power law was constructed using a nonlinear least squares algorithm to obtain the following relationship

$$t_c = 26.6 k_P^{-0.433} \tag{4.26}$$

where k_P (W/m·°C) is the paste thermal conductivity. The power law in Eq. (4.26) has a correlation coefficient of 0.993 and a root-mean-square error of 0.598 s, indicating a nonlinear relationship between the critical freezing time and the thermal conductivity. As the thermal conductivity increases, the critical freezing time becomes smaller.
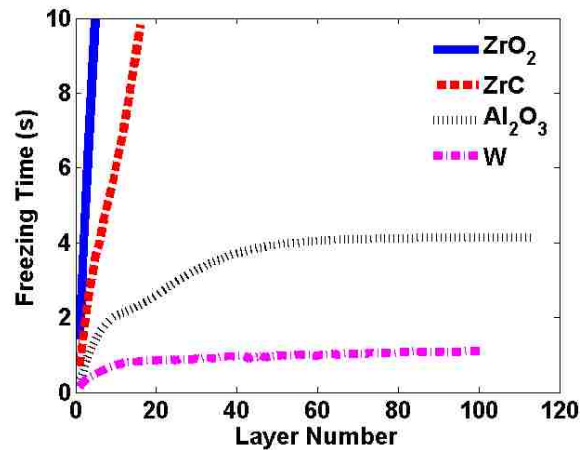
Figure 4.9. Paste freezing time for different paste materials with 45% solids loading, 35 W/m^2·°C convection coefficient (forced convection), 5 °C initial paste temperature, −10 °C ambient temperature, 580 μm filament height and width, and 10 s total time between layers.

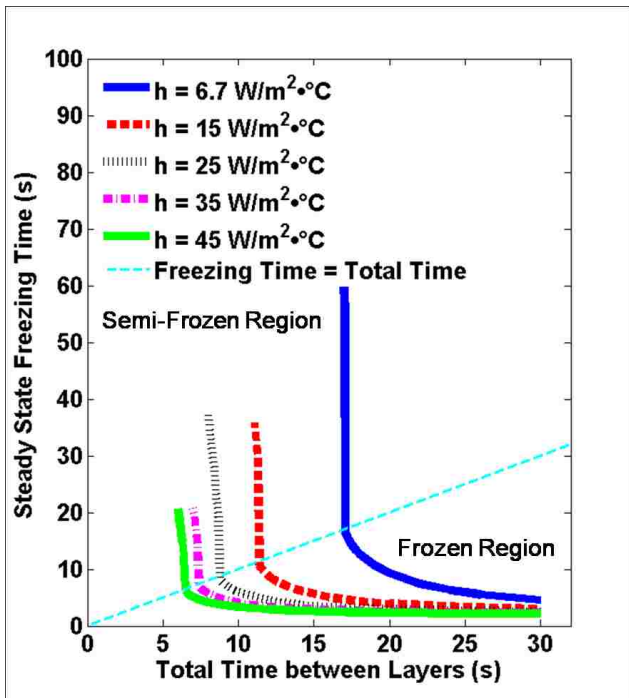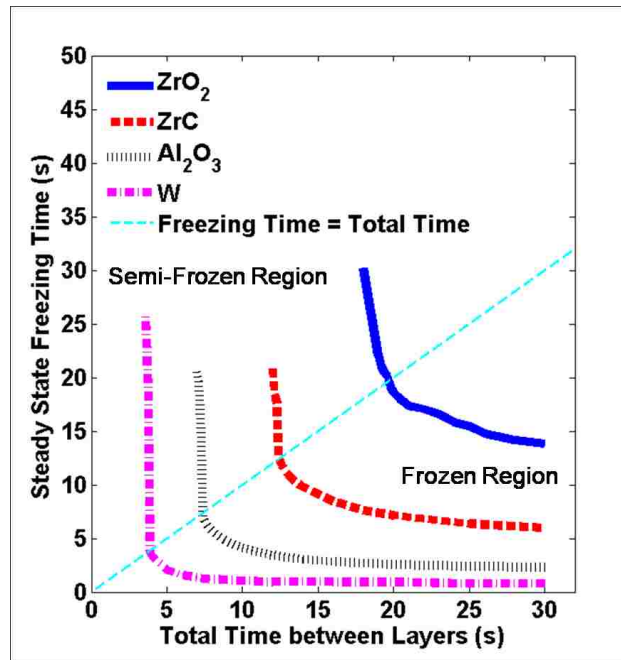Figure 4.10. Steady-state freezing time versus total time between layers for different paste materials with 45% solids loading, 35 W/m^2·°C convection coefficient (forced convection), 5 °C initial paste temperature, −10 °C ambient temperature, and 580 μm filament height and width.
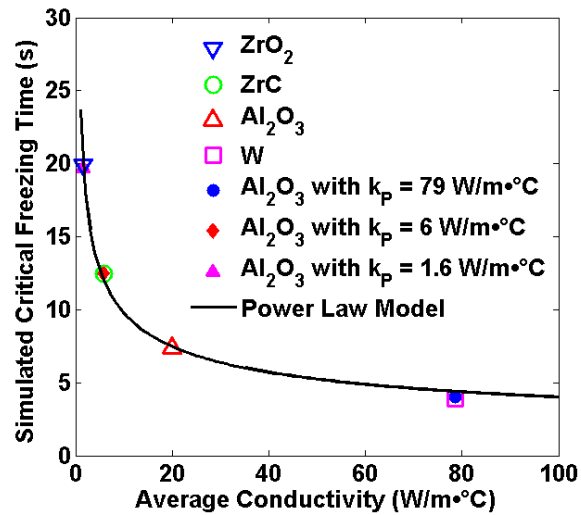
Figure 4.11. Simulated critical freezing time as a function of average thermal conductivity.

4.8.3. Paste Solids Loading. Any change in the paste solids loading will also change the thermal conductivity and the specific heat of the paste, as well as the paste's latent heat. These changes will change the energy contained in the paste and the heat transfer rate, thus affecting the freezing time. The paste freezing time simulation results for different solids loadings (in terms of vol.%) are shown in Figures 4.12 and 4.13. As the solids loading increases, the thermal conductivity increases, the specific heat and the latent heat decrease, and, thus, the freezing time decreases.

The relationship between the critical freezing time and the paste solids loading is plotted in Figure 4.14. A linear model was constructed using a linear least squares algorithm to obtain the following relationship

$$t_c = 15.1 - 16.6 v_e \qquad (4.27)$$

where v_e is vol.% solids loading. The linear model in Eq. (4.27) has a correlation coefficient of 0.996 and a root-mean-square error of 0.389 s, indicating a linear relationship between the critical freezing time and the solids loading. Therefore, in the range of solids loadings considered in Figure 4.14, the paste freezing time is linearly proportional to the vol.% water presented in the paste.
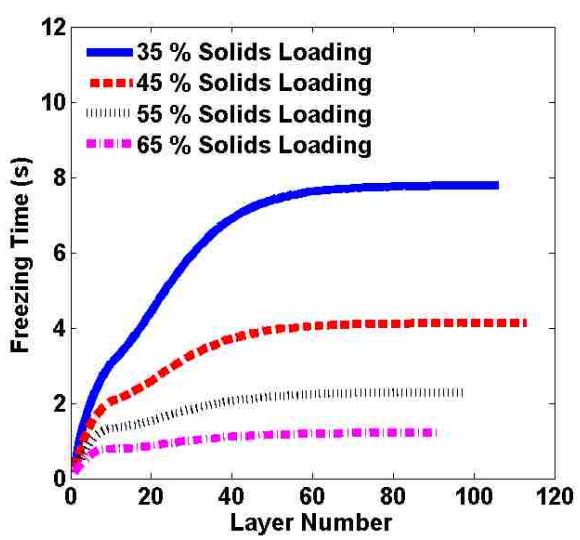
Figure 4.12. Paste freezing time for different paste solids loadings with Al_2O_3 paste, 35 W/m^2·°C convection coefficient (forced convection), 5 °C initial paste temperature, −10 °C ambient temperature, 580 μm filament height and width, and 10 s total time between layers.

Figure 4.13. Steady-state freezing time versus total time between layers for different paste solids loadings with Al_2O_3 paste, 35 W/m^2·°C convection coefficient (forced convection), 5 °C initial paste temperature, −10 °C ambient temperature, and 580 μm filament height and width.
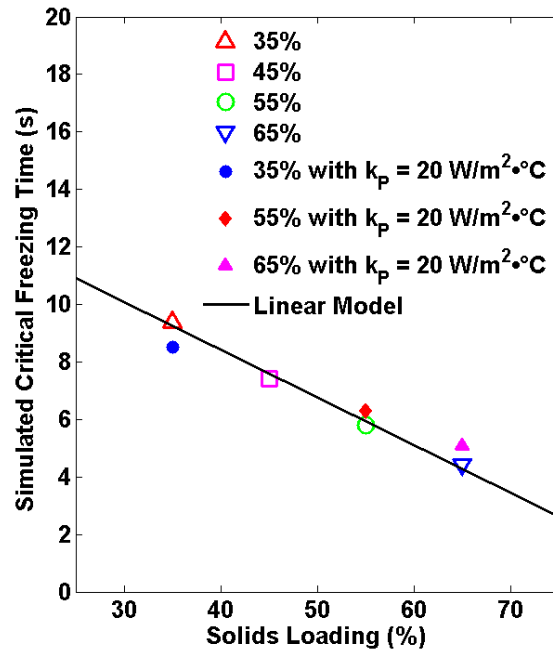
Figure 4.14. Simulated critical freezing time as a function of solids loading.

4.8.4. Initial Paste Temperature. The increase in the initial paste temperature (i.e., the paste temperature in the nozzle right before extrusion) will increase the energy carried by the paste. However, it will also increase the temperature difference between the ambient and the paste; thus, the paste's heat transfer rate to the ambient will increase. The paste freezing time simulation results for different initial paste temperatures are shown in Figures 4.15 and 4.16. As the initial temperature increases, the paste freezing time increases. The relationship between the critical freezing time and the initial paste temperature is plotted in Figure 4.17. A linear model was constructed using a linear least squares algorithm to obtain the following relationship

$$t_c = 6.73 + 0.13T_0 \qquad (4.28)$$

where T_0 (°C) is the initial paste temperature. The linear model in Eq. (4.28) has a correlation coefficient of 0.999 and a root-mean-square error of 0.135 s. Therefore, in the range of initial paste temperatures considered in Figure 4.17, the relationship between the critical freezing time and the initial paste temperature is linear.

Figure 4.15. Paste freezing time for different initial paste temperatures with Al_2O_3 paste, 45% solids loading, 35 W/m^2·°C convection coefficient (forced convection), −10 °C ambient temperature, 580 μm filament height and width, and 10 s total time between layers.

Figure 4.16. Steady-state freezing time versus total time between layers for different initial paste temperatures with Al_2O_3 paste, 45% solids loading, 35 W/m^2·°C convection coefficient (forced convection), −10 °C ambient temperature, and 580 μm filament height and width.
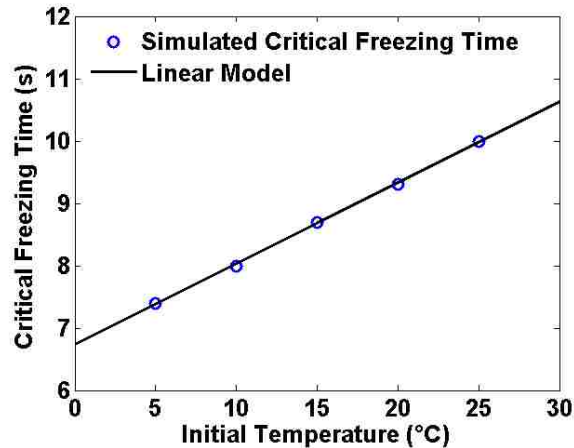
Figure 4.17. Simulated critical freezing time as a function of initial paste temperature.

4.8.5. Ambient Temperature. The change in the ambient temperature will modify the temperature difference between the ambient and the extruded paste, thus changing the heat transfer rate and the paste freezing time. When the ambient temperature decreases, the paste freezing time will decrease. The paste freezing time simulation results for different ambient temperatures are shown in Figures 4.18 and 4.19. The relationship between the critical freezing time and the ambient temperature is plotted in Figure 4.20. A power law was constructed using a nonlinear least squares algorithm to obtain the following relationship

$$t_c = 62.4\left(-T_\infty\right)^{-0.922} \tag{4.29}$$

where T_∞ (°C) is the ambient temperature. The power law in Eq. (4.29) has a correlation coefficient of 0.999 and a root-mean-square error of 0.216 s, indicating a nonlinear relationship between the critical freezing time and the ambient temperature. As the ambient temperature decreases, the paste freezing time decreases more slowly with respect to the decrease in ambient temperature.
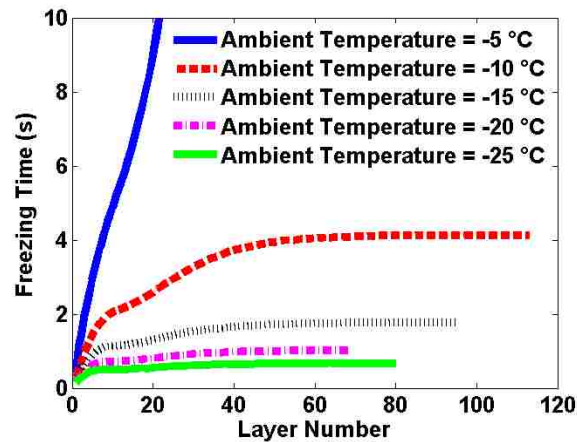
Figure 4.18. Paste freezing time for different ambient temperatures with Al_2O_3 paste, 45% solids loading, 35 $W/m^2 \cdot °C$ convection coefficient (forced convection), 5 °C initial paste temperature, 580 μm filament height and width, and 10 s total time between layers.
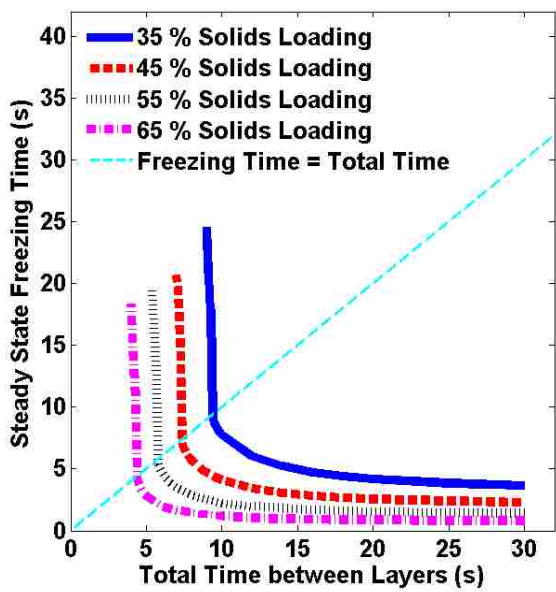

Figure 4.19. Steady-state freezing time versus total time between layers for different ambient temperatures with Al_2O_3 paste, 45% solids loading, 35 $W/m^2 \cdot °C$ convection coefficient (forced convection), 5 °C initial paste temperature, and 580 μm filament height and width.
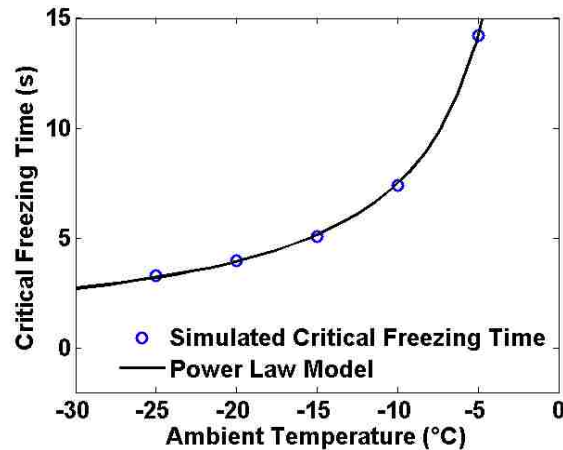
Figure 4.20. Simulated critical freezing time as a function of ambient temperature.

4.8.6. Filament Height. A change in the filament height will alter the ratio between the volume and the surface of the extruded paste exposed to the ambient, which will in turn alter the ratio between the energy contained in the paste and the heat transfer rate. The simulation results for varying filament height are shown in Figures 4.21 and 4.22. When the filament height decreases, the paste freezing time decreases; however, the number of layers required to build the same part increases.

The relationship between the critical freezing time and the filament height is plotted in Figure 4.23. A linear model was constructed using a linear least squares algorithm to obtain the following relationship

$$t_c = 0.193 + 0.0126\Delta z \tag{4.30}$$

where Δz (μm) is the filament height. The linear model in Eq. (4.30) has a correlation coefficient of 0.999 and a root-mean-square error of 0.192 s, which is small relative to the average critical freezing time of 5.8 s. The y-intercept of the linear model is 0.193 s, which is also small relative to the average critical freezing time, indicating that the critical freezing time is linearly proportional to the filament height. Therefore, in the range of filament heights considered in Figure 4.23, if the total time between layers in the FEF process is set the same as the critical freezing time, then the total part build time will not be affected by changes in filament height.
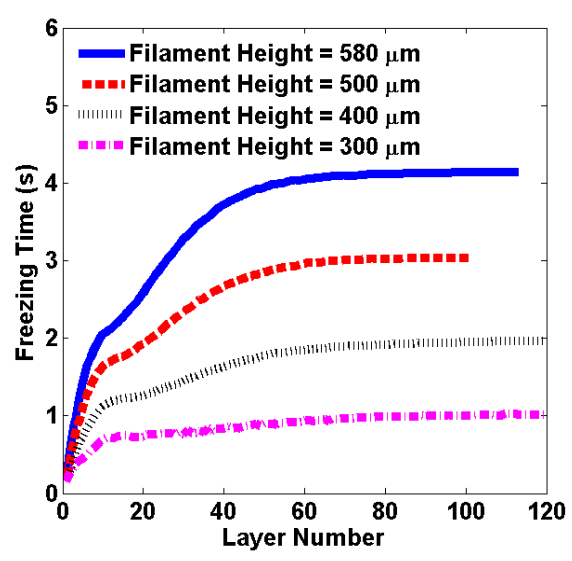
Figure 4.21. Paste freezing time for different filament heights with Al_2O_3 paste, 45% solids loading, 35 W/m^2·°C convection coefficient (forced convection), 5 °C initial paste temperature, −10 °C ambient temperature, 580 μm filament width, and 10 s total time between layers.
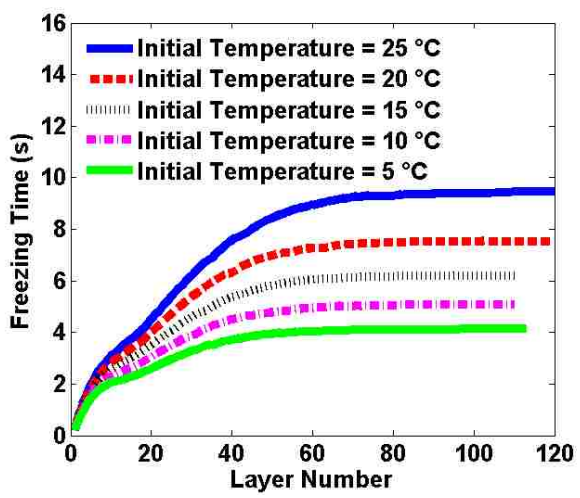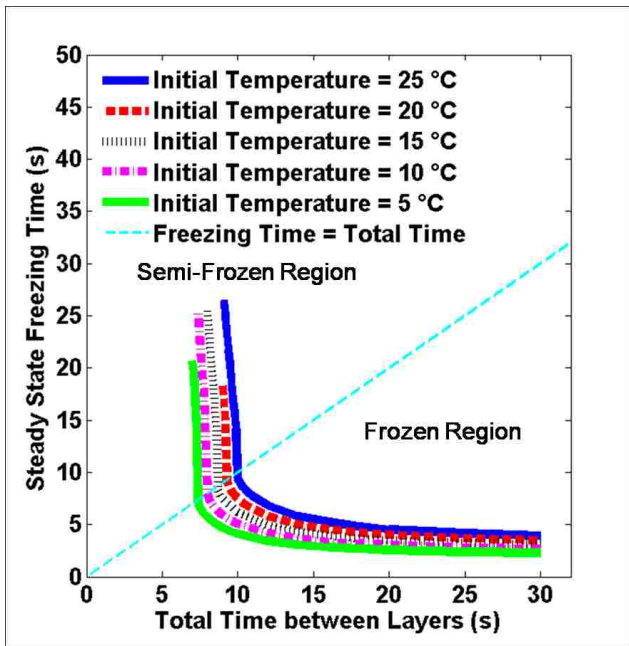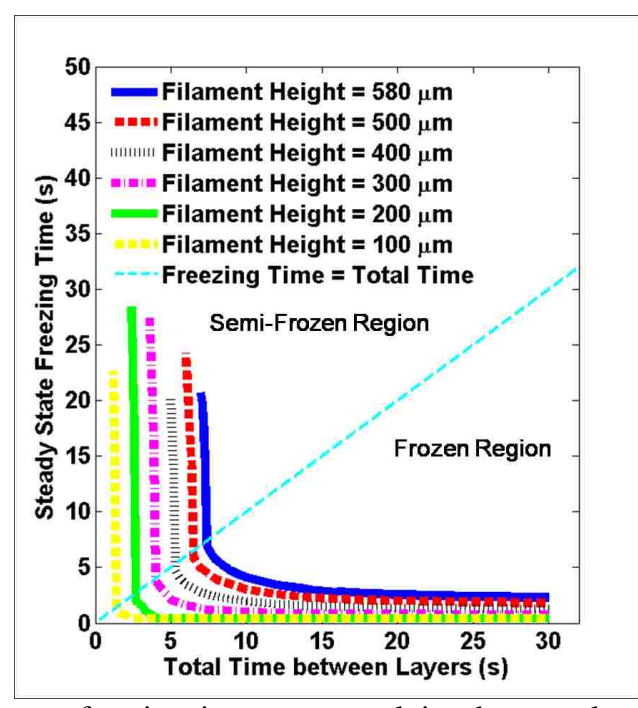

Figure 4.22. Steady-state freezing time versus total time between layers for different filament heights with Al_2O_3 paste, 45% solids loading, 35 W/m^2·°C convection coefficient (forced convection), 5 °C initial paste temperature, −10 °C ambient temperature, and 580 μm filament width.
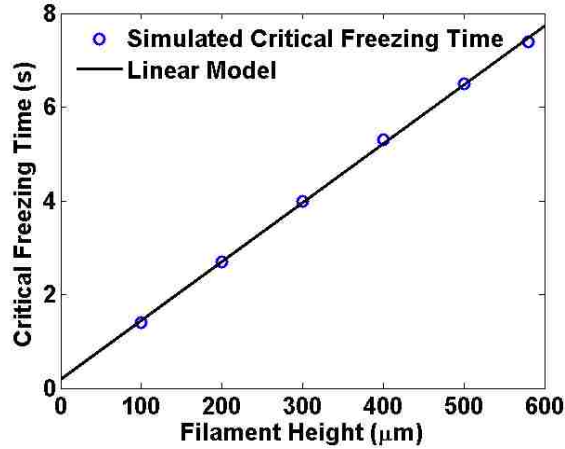
Figure 4.23. Simulated critical freezing time as a function of filament height.

4.8.7. Filament Width. Like the filament height, a change in the filament width will also alter the ratio between the volume and the surface of the extruded paste exposed to the ambient, which will in turn alter the ratio between the energy contained in the paste and the heat transfer rate. The simulation results for varying filament width are shown in Figures 4.24 and 4.25. When the filament width increases, the paste freezing time will increase. The relationship between the critical freezing time and the filament width is plotted in Figure 4.26. A power law was constructed using a nonlinear least squares algorithm to obtain the following relationship

$$t_c = 0.326 \Delta y^{0.490} \tag{4.31}$$

where Δy (μm) is the filament width. The power law in Eq. (4.31) has a correlation coefficient of 0.968 and a root-mean-square error of 0.144 s, indicating a nonlinear relationship between the critical freezing time and the filament width. As the filament width increases, the paste freezing time becomes larger.
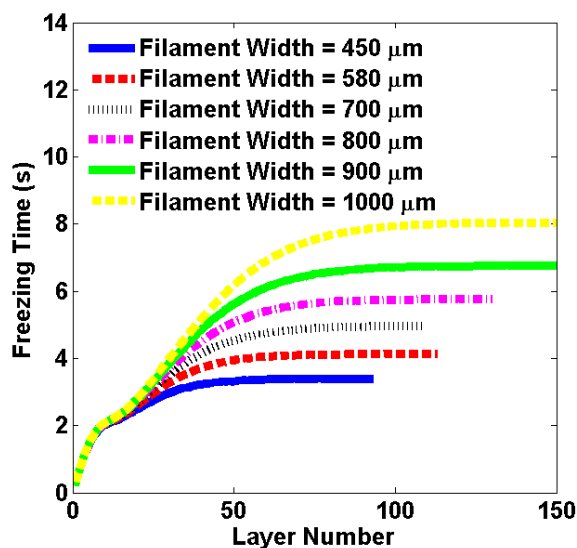
Figure 4.24. Paste freezing time for different filament widths with Al_2O_3 paste, 45% solids loading, 35 W/m^2·°C convection coefficient (forced convection), 5 °C initial paste temperature, –10 °C ambient temperature, 580 μm filament height, and 10 s total time between layers.
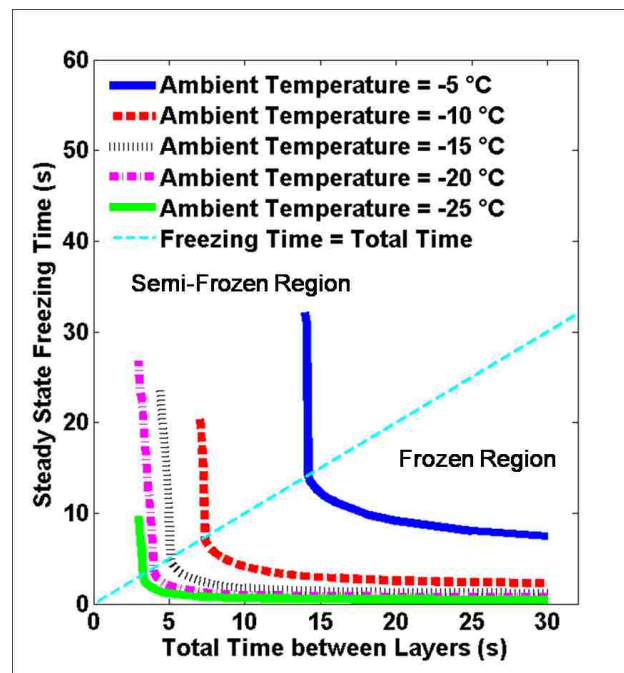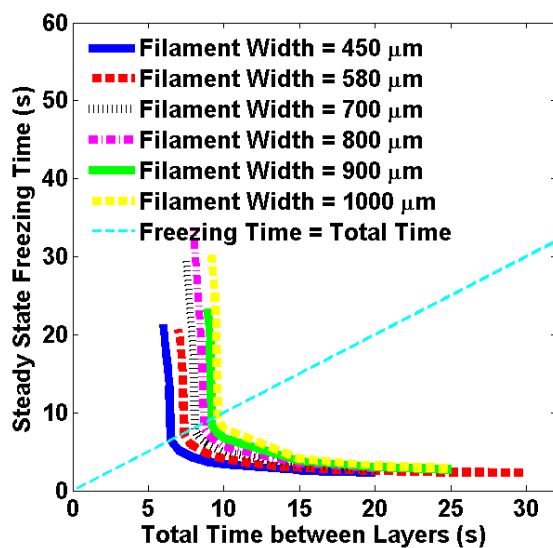

Figure 4.25. Steady-state freezing time versus total time between layers for different filament widths with Al_2O_3 paste, 45% solids loading, 35 W/m^2·°C convection coefficient (forced convection), 5 °C initial paste temperature, –10 °C ambient temperature, and 580 μm filament height.
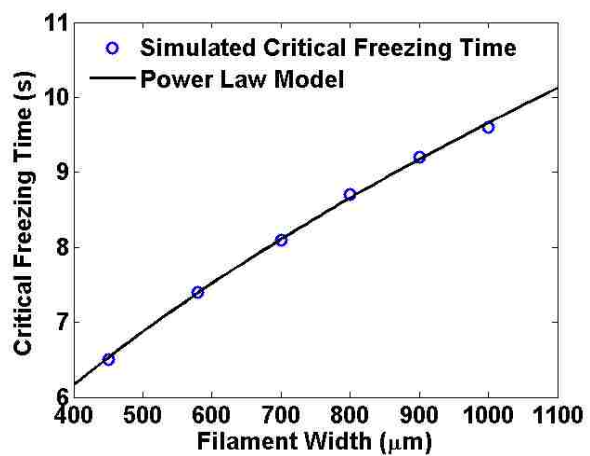
Figure 4.26. Simulated critical freezing time as a function of filament width.

5. MODELING AND ANALYSIS OF PASTE FREEZING IN FREEZE-FORM EXTRUSION FABRICATION OF THIN-WALL PARTS VIA LUMPED METHOD

5.1. LUMPED METHOD

Consider a thin wall composed of N paste filaments, as shown in Figure 5.1. Each filament has width Δy (m) and height Δz (m). According to Fourier's Law, the governing energy equation for the nth filament is

$$\frac{dH_n(t)}{dt} = -\frac{k}{\rho\Delta z^2}\left[T_n(t) - T_{n-1}(t)\right] + \frac{k}{\rho\Delta z^2}\left[T_{n+1}(t) - T_n(t)\right] - \frac{2h}{\rho\Delta y}\left[T_n(t) - T_\infty\right] \quad (5.1)$$

where H_n (J/kg) and T_n (°C) are the enthalpy and temperature, respectively, of the nth filament. When $n = 1$, T_{n-1} is the substrate temperature, which is T_∞. When $n = N$, the conduction term $\frac{k}{\rho\Delta z^2}\left[T_{n+1}(t) - T_n(t)\right]$ is replaced by the convection term

$$-\frac{h}{\rho\Delta z}\left[T_n(t) - T_\infty\right].$$
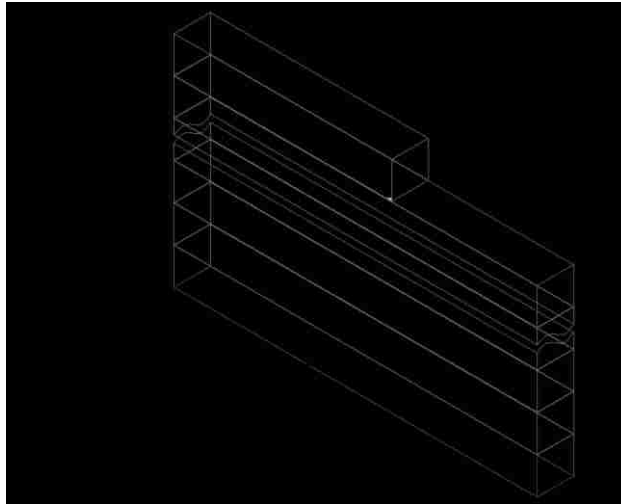
Figure 5.1. Schematic of thin wall composed of N paste filaments.

A thin wall may contain three regions: solid, mushy, and liquid. Let subscripts s, m, and l indicate the solid, mushy, and liquid regions, respectively. Considering the specific heat as constant, the temperature can be obtained based on the definition of enthalpy

$$T(H) = \begin{cases} \dfrac{H}{c} + T_\infty & H \le cT_S \\[2mm] T_S & cT_S < H < cT_S + L \\[2mm] \dfrac{H-L}{c} + T_\infty & H \ge cT_S + L \end{cases} \tag{5.2}$$

where T_S (°C) is the solidus temperature. Therefore, for filaments in the solid region, Eq. (5.1) can be rewritten using the form of enthalpy

$$\frac{dH_n(t)}{dt} = -\frac{k}{\rho c \Delta z^2}\left[H_n(t) - H_{n-1}(t)\right] + \frac{k}{\rho c \Delta z^2}\left[H_{n+1}(t) - H_n(t)\right] - \frac{2h}{\rho c \Delta y}H_n(t) \tag{5.3}$$

For filaments in the mushy liquid region, their temperatures are constant (T_S) and, in this case, Eq. (1) becomes

$$\frac{dH_n(t)}{dt} = -\frac{2}{\rho \Delta y}\left[h(T_S - T_\infty)\right] \tag{5.4}$$

For the filaments in the liquid region, Eq. (1) becomes

$$\frac{dH_n(t)}{dt} = -\frac{k}{\rho c \Delta z^2}\left[H_n(t) - H_{n-1}(t)\right]$$
$$+ \frac{k}{\rho c \Delta z^2}\left[H_{n+1}(t) - H_n(t)\right] - \frac{2h}{\rho c \Delta y}\left[H_n(t) - L\right] \tag{5.5}$$

where L (J/kg·K) is the latent heat. Let $\tau = \dfrac{kt}{\rho c \Delta z^2}$, $\mathrm{Bi} = \dfrac{h\Delta z^2}{k\Delta y}$, $\mathrm{Bi}_z = \dfrac{h\Delta z}{k}$,

$\eta = \dfrac{H}{c(T_S - T_\infty)}$, and $E = \dfrac{L}{c(T_S - T_\infty)}$ denote the non-dimensional time, effective Biot number, effective vertical Biot number, non-dimensional enthalpy, and non-dimensional latent heat, respectively. Combining Eqs. (5.3)–(5.5) and rewriting them in matrix form

$$\begin{bmatrix} \boldsymbol{\eta}'_s(\tau) \\ \boldsymbol{\eta}'_m(\tau) \\ \boldsymbol{\eta}'_l(\tau) \end{bmatrix} = \begin{bmatrix} \mathbf{M}_s & \mathbf{O} & \mathbf{O} \\ \mathbf{U} & \mathbf{O} & \mathbf{D} \\ \mathbf{O} & \mathbf{O} & \mathbf{M}_l \end{bmatrix} \begin{bmatrix} \boldsymbol{\eta}_s(\tau) \\ \boldsymbol{\eta}_m(\tau) \\ \boldsymbol{\eta}_l(\tau) \end{bmatrix} + \begin{bmatrix} \boldsymbol{\beta}_s \\ \boldsymbol{\beta}_m \\ \boldsymbol{\beta}_l \end{bmatrix} \tag{5.6}$$

where

$$\mathbf{M}_s = \begin{bmatrix} -(3+2\mathrm{Bi}) & 1 & 0 & \cdots & 0 \\ \ddots & \ddots & \ddots & \ddots & \vdots \\ \vdots & 1 & -2(1+\mathrm{Bi}) & 1 & \vdots \\ \vdots & \ddots & \ddots & \ddots & \ddots \\ 0 & \cdots & 0 & 1 & -2(1+\mathrm{Bi}) \end{bmatrix} \tag{5.7}$$

$$\mathbf{M}_l = \begin{bmatrix} -2(1+\mathrm{Bi}) & 1 & 0 & \cdots & 0 \\ \ddots & \ddots & \ddots & \ddots & \vdots \\ \vdots & 1 & -2(1+\mathrm{Bi}) & 1 & \vdots \\ \vdots & \ddots & \ddots & \ddots & \ddots \\ 0 & \cdots & 0 & 1 & -(1+2\mathrm{Bi}+\mathrm{Bi}_z) \end{bmatrix} \tag{5.8}$$

$$\mathbf{U} = \begin{bmatrix} 0 & \cdots & 0 & 1 \\ \vdots & \ddots & 0 & 0 \\ \vdots & \ddots & \ddots & \vdots \\ 0 & \cdots & \cdots & 0 \end{bmatrix} \tag{5.9}$$

$$\mathbf{D} = \begin{bmatrix} 0 & \cdots & \cdots & 0 \\ \vdots & \ddots & \ddots & \vdots \\ 0 & 0 & \ddots & \vdots \\ 1 & 0 & \cdots & 0 \end{bmatrix} \tag{5.10}$$

$$\boldsymbol{\beta}_s = \begin{bmatrix} 0 & \cdots & 0 & 1 \end{bmatrix}^T \tag{5.11}$$

$$\boldsymbol{\beta}_m = \begin{bmatrix} -(1+2\mathrm{Bi}) & -2\mathrm{Bi} & \cdots & -2\mathrm{Bi} & -(1+2\mathrm{Bi}+E) \end{bmatrix}^T \tag{5.12}$$

$$\boldsymbol{\beta}_l = \begin{bmatrix} (1+2\mathrm{Bi}E+E) & 2\mathrm{Bi}E & \cdots & 2\mathrm{Bi}E & (2\mathrm{Bi}+\mathrm{Bi}_z)E \end{bmatrix}^T \tag{5.13}$$

and $\boldsymbol{\eta}'_*(\tau)$ is the derivative of $\boldsymbol{\eta}_*(\tau)$ with respect to τ, where the subscript * is s for solid region, m for mushy region, and l for liquid region. Therefore, the solution for the solid and liquid regions is

$$\boldsymbol{\eta}_*(\tau) = \mathbf{Q}_* \left[\mathbf{R}_* \boldsymbol{\eta}_*(0) \circ \exp(\boldsymbol{\lambda}_* \tau) \right]$$
$$+ \mathbf{Q}_* \left\{ \mathbf{R}_* \circ \left\{ \left\{ \left[\exp(\boldsymbol{\lambda}_* \tau) - 1 \right] \circ \frac{1}{\boldsymbol{\lambda}_*} \right\} \mathbf{v}^T \right\} \right\} \boldsymbol{\beta}_* \tag{5.14}$$

where the symbol $\circ$ denotes element-wise product, $\boldsymbol{\lambda}$ is the eigenvalue vector of matrix $\mathbf{M}$, $\mathbf{Q}$ is the corresponding eigenvector matrix, $\mathbf{R}$ is the inverse matrix of $\mathbf{Q}$, and

$$\mathbf{v} = \begin{bmatrix} 1 & \cdots & 1 & \cdots & 1 \end{bmatrix}^T \tag{5.15}$$

The solution for the mushy region is

$$\boldsymbol{\eta}_m(\tau) = \boldsymbol{\eta}_m(0) + \boldsymbol{\beta}_m \tau + \boldsymbol{\varphi}_m(\tau) \tag{5.16}$$

where

$$\boldsymbol{\varphi}_m(\tau) = \left[\int_0^\tau \eta_{s,N_s}(\varepsilon) d\varepsilon \quad 0 \quad \cdots \quad 0 \quad \cdots \quad 0 \quad \int_0^\tau \eta_{l,1}(\varepsilon) d\varepsilon \right]^T \tag{5.17}$$

$$\int_0^\tau \boldsymbol{\eta}_*(\varepsilon) d\varepsilon = \mathbf{Q}_* \left\{ \mathbf{R}_* \boldsymbol{\eta}_*(0) \circ \left[\exp(\boldsymbol{\lambda}_* \tau) - 1 \right] \circ \frac{1}{\boldsymbol{\lambda}_*} \right\}$$
$$+ \mathbf{Q}_* \left\{ \mathbf{R}_* \circ \left\{ \left\{ \left[\exp(\boldsymbol{\lambda}_* \tau) - \boldsymbol{\lambda}_* \tau - 1 \right] \circ \frac{1}{\boldsymbol{\lambda}_* \circ \boldsymbol{\lambda}_*} \right\} \mathbf{v}^T \right\} \right\} \boldsymbol{\beta}_* \tag{5.18}$$

For the solid region, the elements of the corresponding matrices and vectors are [34]

$$\lambda_{s,i} = -2 \left[1 + \text{Bi} - \cos\left(\frac{2i\pi}{2N_s + 1} \right) \right] \tag{5.19}$$

$$Q_{s,ij} = \sin\left[\frac{(2i-1) j\pi}{2N_s + 1} \right] \tag{5.20}$$

$$R_{s,ij} = \frac{4}{2N_s + 1} Q_{s,ji} = \frac{4}{2N_s + 1} \sin\left[\frac{i(2j-1)\pi}{2N_s + 1} \right] \tag{5.21}$$

In most of the cases studied, Bi_z is typically smaller than 0.01; therefore, $\mathrm{Bi}_z \approx 0$. The physical meaning of this approximation is that the top of the liquid region is modeled as an insulated surface. In this case, Eq. (5.8) becomes

$$\mathbf{M}_l = \begin{bmatrix} -2(1+\mathrm{Bi}) & 1 & 0 & \cdots & 0 \\ \ddots & \ddots & \ddots & \ddots & \vdots \\ \vdots & 1 & -2(1+\mathrm{Bi}) & 1 & \vdots \\ \vdots & \ddots & \ddots & \ddots & \ddots \\ 0 & \cdots & 0 & 1 & -(1+2\mathrm{Bi}) \end{bmatrix} \tag{5.22}$$

and the elements of the corresponding matrices and vectors for the liquid region are [34]

$$\lambda_{l,i} = -2\left[1+\mathrm{Bi} - \cos\left(\frac{2i-1}{2N_l+1}\pi\right)\right] \tag{5.23}$$

$$Q_{l,ij} = \sin\left[\frac{i(2j-1)\pi}{2N_l+1}\right] \tag{5.24}$$

$$R_{l,ij} = \frac{4}{2N_l+1}Q_{l,ji} = \frac{4}{2N_l+1}\sin\left[\frac{(2i-1)j\pi}{2N_l+1}\right] \tag{5.25}$$

When a new layer is deposited, the freezing time of the layer is composed of two parts. The first part is the time spent for the liquid region to transform into a mushy region. The second part is the time spent for the mushy region to transform into a solid region. Due to the fact that the latent heat is much larger than the specific heat and the initial temperature is very close to the solidus temperature, the liquid region transforms into a mushy region much faster than the mushy region transforms into a solid region. Therefore, for the extruded paste, the freezing time can be computed from the non-dimensional freezing time

$$t_f = \frac{\rho c \Delta z^2}{k}\sum_{n=1}^{N_m}\tau_{f,n} \tag{5.26}$$

where $\tau_{f,n}$ is the solution of

$$\eta_{m,1}(\tau) = 1 \tag{5.27}$$

In this case, the liquid region does not need to be considered and Eq. (5.6) becomes

$$\begin{bmatrix} \boldsymbol{\eta}_s'(\tau) \\ \boldsymbol{\eta}_m'(\tau) \end{bmatrix} = \begin{bmatrix} \mathbf{M}_s & \mathbf{O} \\ \mathbf{U} & \mathbf{O} \end{bmatrix} \begin{bmatrix} \boldsymbol{\eta}_s(\tau) \\ \boldsymbol{\eta}_m(\tau) \end{bmatrix} + \begin{bmatrix} \boldsymbol{\beta}_s \\ \boldsymbol{\beta}_m \end{bmatrix} \tag{5.28}$$

This change means there is no liquid region and the top surface of the mushy region is directly exposed to the ambient. Therefore, the terms in Eq. (5.16) become

$$\boldsymbol{\beta}_m = \begin{bmatrix} -(1+2\mathrm{Bi}) & -2\mathrm{Bi} & \cdots & -2\mathrm{Bi} & -(1+2\mathrm{Bi}+\mathrm{Bi}_z) \end{bmatrix}^T \tag{5.29}$$

$$\boldsymbol{\varphi}_m(\tau) = \begin{bmatrix} \int_0^\tau \eta_{s,N_s}(\varepsilon)d\varepsilon & 0 & \cdots & 0 & \cdots & 0 \end{bmatrix}^T \tag{5.30}$$

Substituting Eqs. (5.19)−(5.21) into Eq. (5.16)

$$\begin{aligned} \eta_{m,1}(\tau) = \eta_{m,1}(0) &- (1+2\mathrm{Bi})\tau + \frac{4}{2N_s+1}\sum_{i=1}^{N_s}\left\{\frac{\exp(\lambda_{s,i}\tau)-\lambda_{s,i}\tau-1}{\lambda_{s,i}^2}\sin^2\left[\frac{(2N_s-1)i\pi}{2N_s+1}\right]\right\} \\ &+ \frac{4}{2N_s+1}\sum_{i=1}^{N_s}\left\{\frac{\exp(\lambda_{s,i}\tau)-1}{\lambda_{s,i}}\sin\left[\frac{(2N_s-1)i\pi}{2N_s+1}\right]\sum_{j=1}^{N_s}\left\{\sin\left[\frac{i(2j-1)\pi}{2N_s+1}\right]\eta_{s,j}(0)\right\}\right\} \end{aligned} \tag{5.31}$$

When $\tau \gg 0$, the terms $\exp(\lambda_n\tau)$ are negligible for $n>1$. Therefore, Eq. (5.27) becomes

$$\begin{aligned} &\frac{4}{2N_s+1}\left\{\frac{1}{\lambda_{s,1}^2}\sin^2\left(\frac{2\pi}{2N_s+1}\right)+\frac{1}{\lambda_{s,1}}\sin\left(\frac{2\pi}{2N_s+1}\right)\sum_{j=1}^{N_s}\left\{\sin\left[\frac{(2j-1)\pi}{2N_s+1}\right]\eta_{s,j}(0)\right\}\right\}\exp(\lambda_{s,1}\tau) \\ &= \left\{(1+2\mathrm{Bi})+\frac{4}{2N_s+1}\sum_{i=1}^{N_s}\left[\frac{1}{\lambda_{s,i}}\sin^2\left(\frac{2i\pi}{2N_s+1}\right)\right]\right\}\tau \\ &\quad + \eta_{m,1}(\tau)-\eta_{m,1}(0)+\frac{4}{2N_s+1}\sum_{i=1}^{N_s}\left[\frac{1}{\lambda_{s,i}^2}\sin^2\left(\frac{2i\pi}{2N_s+1}\right)\right] \\ &\quad + \frac{4}{2N_s+1}\sum_{i=1}^{N_s}\left\{\frac{1}{\lambda_{s,i}}\sin\left[\frac{(2N_s-1)i\pi}{2N_s+1}\right]\sum_{j=1}^{N_s}\left\{\sin\left[\frac{i(2j-1)\pi}{2N_s+1}\right]\eta_{s,j}(0)\right\}\right\} \end{aligned} \tag{5.32}$$

To prevent the part from deforming or collapsing during the fabrication process, the new paste layer should only be deposited when the previous layers are frozen. In that case, the mushy region typically only has one layer. Solving Eq. (5.32) and noting $\eta_{m,1}(0) \approx 1+E$, the non-dimensional freezing time is

$$\tau_f = -\frac{W\left[-\dfrac{\lambda_{s,1}}{\alpha}\exp\left(-\dfrac{\gamma}{\alpha}\lambda_{s,1}\right)\right]}{\lambda_1} - \frac{\gamma}{\alpha} \tag{5.33}$$

where W is Lambert W function, principal branch and

$$\alpha = \frac{\left(1+2\mathrm{Bi}+\mathrm{Bi}_z\right)+\dfrac{4}{2N_s+1}\displaystyle\sum_{i=1}^{N_s}\left[\dfrac{1}{\lambda_{s,i}}\sin^2\left(\dfrac{2i\pi}{2N_s+1}\right)\right]}{\dfrac{4}{2N_s+1}\left\{\dfrac{1}{\lambda_{s,1}^2}\sin^2\left(\dfrac{2\pi}{2N_s+1}\right)+\dfrac{1}{\lambda_{s,1}}\sin\left(\dfrac{2\pi}{2N_s+1}\right)\displaystyle\sum_{j=1}^{N_s}\left\{\sin\left[\dfrac{(2j-1)\pi}{2N_s+1}\right]\eta_{s,j}(0)\right\}\right\}} \tag{5.34}$$

$$\gamma = \frac{-E+\dfrac{4}{2N_s+1}\displaystyle\sum_{i=1}^{N_s}\left\{\dfrac{1}{\lambda_{s,i}^2}\sin^2\left(\dfrac{2i\pi}{2N_s+1}\right)+\dfrac{1}{\lambda_{s,i}}\sin\left[\dfrac{(2N_s-1)i\pi}{2N_s+1}\right]\displaystyle\sum_{j=1}^{N_s}\left\{\sin\left[\dfrac{i(2j-1)\pi}{2N_s+1}\right]\eta_{s,j}(0)\right\}\right\}}{\dfrac{4}{2N_s+1}\left\{\dfrac{1}{\lambda_{s,1}^2}\sin^2\left(\dfrac{2\pi}{2N_s+1}\right)+\dfrac{1}{\lambda_{s,1}}\sin\left(\dfrac{2\pi}{2N_s+1}\right)\displaystyle\sum_{j=1}^{N_s}\left\{\sin\left[\dfrac{(2j-1)\pi}{2N_s+1}\right]\eta_{s,j}(0)\right\}\right\}} \tag{5.35}$$

In the cases studied in this paper, $W\left[-\dfrac{\lambda_1}{\alpha}\exp\left(-\dfrac{\gamma}{\alpha}\lambda_1\right)\right]$ is small relative to the term $\dfrac{\gamma}{\alpha}\lambda_1$

and, thus, may be neglected. In this case, Eq. (5.33) becomes

$$\tau_f = \frac{E-\dfrac{4}{2N_s+1}\displaystyle\sum_{i=1}^{N_s}\left\{\dfrac{1}{\lambda_{s,i}^2}\sin^2\left(\dfrac{2i\pi}{2N_s+1}\right)-\dfrac{1}{\lambda_{s,i}}\sin\left[\dfrac{(2N_s-1)i\pi}{2N_s+1}\right]\displaystyle\sum_{j=1}^{N_s}\left\{\sin\left[\dfrac{i(2j-1)\pi}{2N_s+1}\right]\eta_{s,j}(0)\right\}\right\}}{\left(1+2\mathrm{Bi}+\mathrm{Bi}_z\right)+\dfrac{4}{2N_s+1}\displaystyle\sum_{i=1}^{N_s}\left[\dfrac{1}{\lambda_{s,i}}\sin^2\left(\dfrac{2i\pi}{2N_s+1}\right)\right]} \tag{5.36}$$

Similar to the approximation in the liquid region, Bi_z is negligible in the cases studied in this paper. Letting subscript d denote steady state, the steady-state freezing time is

$$\tau_d = \frac{E-C_{\lambda2}-C_\eta}{1+2\mathrm{Bi}+C_{\lambda1}} \tag{5.37}$$

where

$$C_{\lambda1}(\mathrm{Bi}) = \lim_{N_s\to\infty}\left\{\frac{4}{2N_s+1}\sum_{i=1}^{N_s}\left[\frac{1}{\lambda_{s,i}}\sin^2\left(\frac{2i\pi}{2N_s+1}\right)\right]\right\} \tag{5.38}$$

$$C_{\lambda2}(\mathrm{Bi}) = \lim_{N_s\to\infty}\left\{\frac{4}{2N_s+1}\sum_{i=1}^{N_s}\left[\frac{1}{\lambda_{s,i}^2}\sin^2\left(\frac{2i\pi}{2N_s+1}\right)\right]\right\} = \frac{dC_{\lambda1}}{2d\mathrm{Bi}} \tag{5.39}$$

$$C_\eta(\mathrm{Bi},\tau_\delta) = \lim_{N_s\to\infty}\left\{\frac{4}{2N_s+1}\sum_{i=1}^{N_s}\left\{\frac{1}{\lambda_{s,i}}\sin\left[\frac{(2N_s-1)i\pi}{2N_s+1}\right]\sum_{j=1}^{N_s}\left\{\sin\left[\frac{i(2j-1)\pi}{2N_s+1}\right]\eta_{s,j}(0)\right\}\right\}\right\} \tag{5.40}$$

and the subscript ξ denotes the total time between layers (i.e., summation of the deposition time for the current layer and the dwell time between the current and next layers).

When the steady state occurs, C_η must be constant, which requires

$$\frac{4}{2N_s+1}\sum_{i=1}^{N_s}\left\{\frac{1}{\lambda_{s,i}}\sin\left[\frac{(2N_s-1)i\pi}{2N_s+1}\right]\sum_{j=1}^{N_s}\left\{\sin\left[\frac{i(2j-1)\pi}{2N_s+1}\right]\eta_{s,j}(0)\right\}\right\}$$
$$=\frac{4}{2N_s+3}\sum_{i=1}^{N_s+1}\left\{\frac{1}{\lambda_{s,i}}\sin\left[\frac{(2N_s+1)i\pi}{2N_s+3}\right]\sum_{j=1}^{N_s+1}\left\{\sin\left[\frac{i(2j-1)\pi}{2N_s+3}\right]\eta_{s,j}(\tau_\xi)\right\}\right\}$$

(5.41)

$$\mathbf{\eta}_s(\tau_d)=\frac{4}{2N_s+1}\mathbf{Q}_s\left[\mathbf{Q}_s^T\mathbf{\eta}_s(0)\circ\exp(\lambda_s\tau_d)\right]$$
$$+\frac{4}{2N_s+1}\mathbf{Q}_s\left\{\mathbf{Q}_s^T\circ\left\{\left\{\left[\exp(\lambda_s\tau_d)-1\right]\circ\frac{1}{\lambda_s}\right\}\mathbf{v}_s^T\right\}\right\}\mathbf{\beta}_s$$

(5.42)

$$\mathbf{\eta}_s(\tau_\xi)=\frac{4}{2N_s+3}\left\{\mathbf{Q}_s\left\{\mathbf{Q}_s^T\begin{bmatrix}\mathbf{\eta}_s(\tau_d)\\1\end{bmatrix}\circ\exp\left[\lambda_s(\tau_\xi-\tau_d)\right]\right\}\right\}$$

(5.43)

Note that the steady-state freezing time is a function of the total time between layers and recall the critical freezing time is defined as the time when the steady-state freezing time is equal to the total time between layers. When the critical freezing time occurs, Eqs. (5.42) and (5.43) are combined and

$$\mathbf{\eta}_s(\tau_d)=\begin{bmatrix}\dfrac{4}{2N_s+1}\mathbf{Q}_s\left[\mathbf{Q}_s^T\mathbf{\eta}_s(0)\circ\exp(\lambda_s\tau_d)\right]\\+\dfrac{4}{2N_s+1}\mathbf{Q}_s\left\{\mathbf{Q}_s^T\circ\left\{\left\{\left[\exp(\lambda_s\tau_d)-1\right]\circ\dfrac{1}{\lambda_s}\right\}\mathbf{v}_s^T\right\}\right\}\mathbf{\beta}_s\\1\end{bmatrix}$$

(5.44)

5.2. LUMPED METHOD VERSUS NUMERICAL SIMULATION

According to Eqs.(5.37)−(5.44), the non-dimensional critical freezing time is a function of the non-dimensional latent heat and effective Biot number. Although the non-dimensional total time between layers is only presented in Eq. (5.40), it is solved by

combining Eqs. (5.37), (5.41), and (5.44). Therefore, a random initial enthalpy distribution can be fed into Eq. (5.41) with a reasonable layer number, which is typically between 50 and 150. After several iterations of Eq.(5.44), the critical freezing time is then obtained from Eq. (5.37).

The critical freezing times computed using the lumped method are compared in Figure 5.2 to the numerical simulations results generated using the method described in Section 4. The material properties used in the computation are listed in Table 4.2. As stated in Section 4.6, unless otherwise noted, the convection coefficient was 35 W/m^2·°C, the initial paste temperature was 5 °C, the ambient temperature was −10 °C, and the filament height and width were both 580 μm. As the effective Biot number increases, the percent errors for the data points are 2.04%, 3.25%, 6.29%, 14.4%, respectively. The error is mainly introduced by neglecting the temperature gradient inside a single filament in the lumped method. As the effective Biot number increases, the temperature gradient inside a single filament becomes larger. Therefore, the heat transfer rate computed by the numerical simulation is larger than the heat transfer rate assumed in the lumped method, causing the critical freezing time computed by the numerical simulation to be less than the critical freezing time computed by the lumped method. In the cases studied in this paper, the convection coefficient is typically smaller than 35 W/m^2·°C and the paste conductivity is typically larger than 1.8 W/m·°C; therefore, the effective Biot numbers are always smaller than the maximum effective Biot number in Figure 5.2. The convergence history of the computations is shown in Figure 5.3. All of the computations started with the following initial condition: 150 layers have been deposited and their non-dimensional enthalpies are linearly distributed from zero to the solidus enthalpy value 1 along z direction. All of the computations reached steady state after an additional 20 layers were deposited.
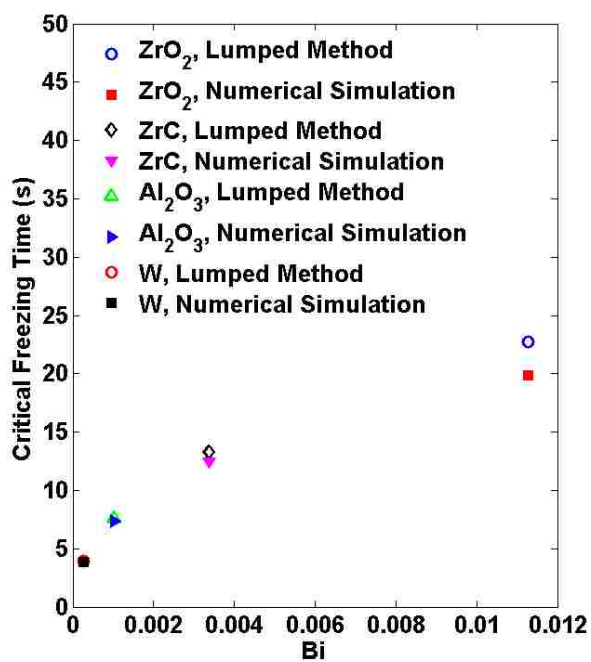
Figure 5.2. Critical freezing time computed by lumped method and numerical simulation.
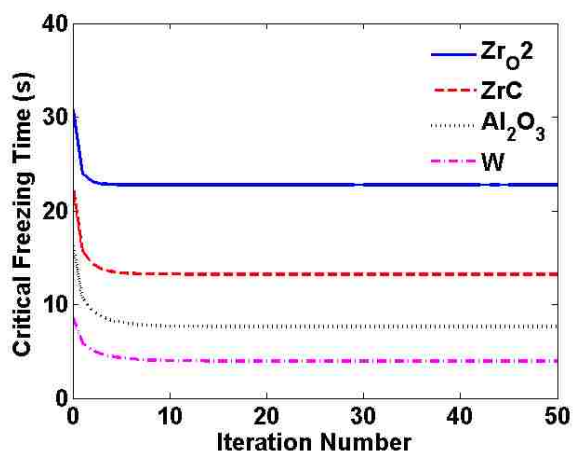
Figure 5.3. Convergence history of the critical freezing times computed using the lumped method.

5.3. EFFECTS OF NON-DIMENSIONAL FACTORS ON CRITICAL FREEZING TIME

As seen in Eq. (5.37), the non-dimensional critical freezing time is a function of the non-dimensional latent heat and effective Biot number. For the cases studied in Section 5.2, the non-dimensional latent heats are between 5 and 8, while the effective Biot number varies from 5×10^{-4} to 1.5×10^{-2}. Therefore, the studies conducted in this paper will focus on the ranges $E \in [4, 9]$ and $\mathrm{Bi} \in [5 \times 10^{-4}, 2 \times 10^{-2}]$.

5.3.1. Non-Dimensional Latent Heat. To study the effect of non-dimensional latent heat, differentiating Eq. (5.37) with respect to non-dimensional latent heat

$$\frac{\partial \tau_d}{\partial E} = \frac{1}{1 + 2\mathrm{Bi} + C_{\lambda 1} + \dfrac{\partial C_\eta}{\partial \tau_d}} \tag{5.45}$$

The term $\partial C_\eta / \partial \tau_d$ is difficult to express explicitly. The iteratively computed value of $\partial C_\eta / \partial \tau_d$ versus τ_d is plotted in Figure 5.4. In the range of effective Biot numbers considered in Figure 5.4, the value of $\partial C_\eta / \partial \tau_d$ is negligible compared to the term $1 + 2\mathrm{Bi} + C_{\lambda 1}$. Therefore, the relationship between the non-dimensional critical freezing time and the non-dimensional latent heat is nearly linear, and the slope is a function of the effective Biot number, as plotted in Figure 5.5. The smaller the effective Biot number, the more rapidly non-dimensional critical freezing time changes.
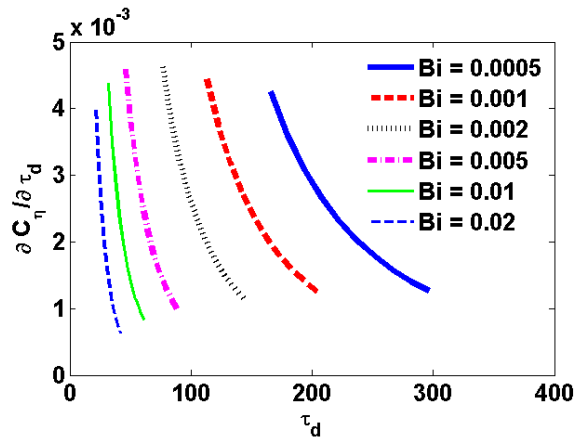
Figure 5.4. Computed $\partial C_\eta / \partial \tau_d$ as a function of non-dimensional critical freezing time.
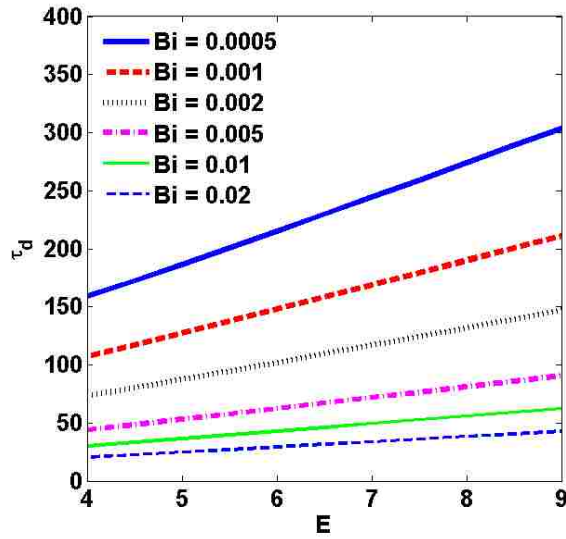
Figure 5.5. Non-dimensional critical freezing time as a function of non-dimensional latent heat for various effective Biot numbers.

5.3.2. Effective Biot Number. To study the effect of the effective Biot number, differentiating Eq. (5.37) with respect to the effective Biot number and rearranging

$$\frac{\partial \tau_d}{\partial \mathrm{Bi}} = -\frac{\left(\dfrac{dC_{\lambda 2}}{d\mathrm{Bi}} + \dfrac{\partial C_\eta}{\partial \mathrm{Bi}}\right)}{\left(1 + 2\mathrm{Bi} + C_{\lambda 1}\right)} - \frac{\left(E - C_{\lambda 2} - C_\eta\right)\left(2 + 2C_{\lambda 2}\right)}{\left(1 + 2\mathrm{Bi} + C_{\lambda 1}\right)^2} \tag{5.46}$$

which is also a complex function that is difficult to express explicitly. The terms $C_{\lambda 1}$, $C_{\lambda 2}$, and C_η, are plotted versus effective Biot number in Figures 5.6 and 5.7. All of these terms are highly nonlinear, and they all can be treated as functions of the effective Biot number. The relationship between the non-dimensional critical freezing time and the effective Biot number is plotted in Figures 5.8 and 5.9. The partial derivative of the non-dimensional critical freezing time with respect to effective Biot number is always negative. When the effective Biot number is small, the absolute value of the partial derivative of the critical freezing time to the Biot number is large. As the effective Biot number increases, the absolute value of the partial derivative decreases nonlinearly.
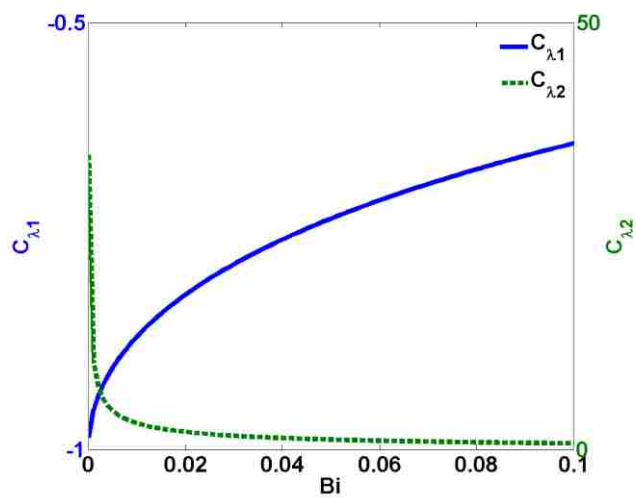
Figure 5.6. $C_{\lambda 1}$ and $C_{\lambda 2}$ as a function of effective Biot number.
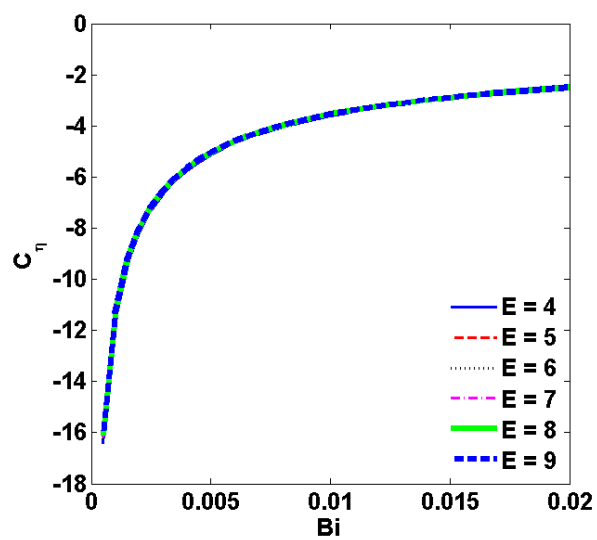
Figure 5.7. Computed C_η as a function of effective Biot number.
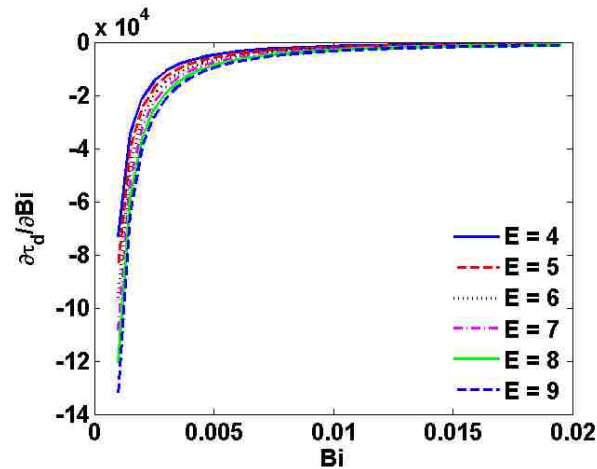
Figure 5.8. Partial derivative of non-dimensional critical freezing time with respect to effective Biot number.
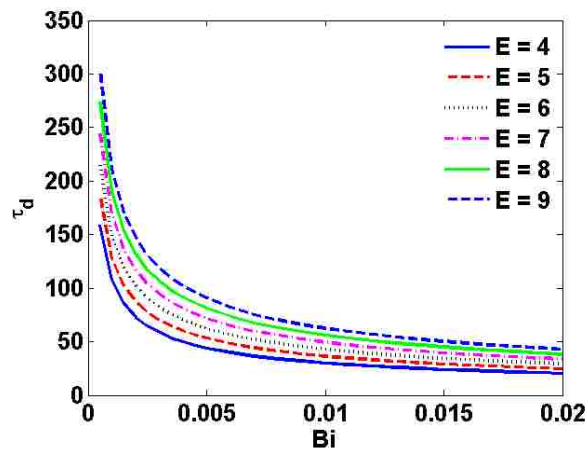
Figure 5.9. Non-dimensional critical freezing time as a function of effective Biot number.

5.4. EFFECTS OF DIMENSIONAL FACTORS ON CRITICAL FREEZING TIME

Only two non-dimensional factors can affect the non-dimensional critical freezing time. However, each non-dimensional factor may be affected by multiple dimensional factors, and some of the dimensional factors can change both non-dimensional factors. The conversion from non-dimensional freezing time τ_d to dimensional freezing time t_d

also involves several dimensional factors. A discussion of the effects of the dimensional factors is given below.

   5.4.1. Convection Coefficient. To study the effect of convection coefficient, Eq. (5.37) is differentiated with respect to convection coefficient. Since the convection coefficient only affects the effective Biot number

$$\frac{\partial t_d}{\partial h} = \frac{\rho c \Delta z^2}{k} \frac{\partial \tau_d}{\partial \mathrm{Bi}} \frac{\partial \mathrm{Bi}}{\partial h} = \frac{\rho c \Delta z^4}{k^2 \Delta y} \frac{\partial \tau_d}{\partial \mathrm{Bi}} \tag{5.47}$$

For the same paste and environmental conditions, the relationship between the critical freezing time and the convection coefficient is proportional to the relationship between the non-dimensional critical freezing time and the effective Biot number, which is depicted in Figure 5.9. Therefore, as the convection coefficient increases, the critical freezing time decreases nonlinearly.

   5.4.2. Paste Material Properties. The change of paste material will change all of the material properties, i.e., thermal conductivity, specific heat, latent heat, and density. To study the effect of material properties, Eq. (5.37) is differentiated with respect to each material property

$$\begin{aligned}
\frac{\partial t_d}{\partial k} &= \frac{-\rho c \Delta z^2}{k^2} \tau_d + \frac{\rho c \Delta z^2}{k} \frac{\partial \tau_d}{\partial \mathrm{Bi}} \frac{\partial \mathrm{Bi}}{\partial k} \\
&= -\frac{\rho c \Delta z^2}{k^2} \left(\tau_d + \mathrm{Bi} \frac{\partial \tau_d}{\partial \mathrm{Bi}} \right) \\
&= -\frac{\rho c \Delta z^2}{k^2} \frac{\partial \left(\tau_d \mathrm{Bi} \right)}{\partial \mathrm{Bi}}
\end{aligned} \tag{5.48}$$

$$\begin{aligned}
\frac{\partial t_d}{\partial c} &= \frac{\rho \Delta z^2}{k} \tau_d + \frac{\rho c \Delta z^2}{k} \frac{\partial \tau_d}{\partial E} \frac{\partial E}{\partial c} \\
&\approx \frac{\rho \Delta z^2}{k} \left[\tau_d - \frac{E}{\left(1 + 2\mathrm{Bi} + C_{\lambda 1} \right)} \right] \\
&= -\frac{\rho \Delta z^2 \left(C_{\lambda 2} + C_\eta \right)}{k \left(1 + 2\mathrm{Bi} + C_{\lambda 1} \right)}
\end{aligned} \tag{5.49}$$

$$\frac{\partial t_d}{\partial L} = \frac{\rho c \Delta z^2}{k} \frac{\partial \tau_d}{\partial E} \frac{\partial E}{\partial L}$$

$$\approx \frac{\rho \Delta z^2}{k \left(1 + 2\text{Bi} + C_{\lambda 1}\right)\left(T_S - T_0\right)}$$

(5.50)

$$\frac{\partial t_d}{\partial \rho} = \frac{c \Delta z^2}{k} \tau_d$$

(5.51)

The partial derivative of $\tau_d \text{Bi}$ with respect to Bi is plotted in Figure 5.10. Since the value of $\partial(\tau_d \text{Bi})/\partial \text{Bi}$ is always positive, $\partial t_d/\partial k$ is always negative. Therefore, as the thermal conductivity increases, the critical freezing time decreases nonlinearly. The summation of $C_{\lambda 2}$ and C_η is plotted in Figure 5.11. Since the summation is always negative, $\partial t_d/\partial c$ is always positive. Therefore, as the specific heat increases, the critical freezing time increases nonlinearly. According to Eqs. (5.50) and (5.51), the critical freezing time is proportional to latent heat and density.
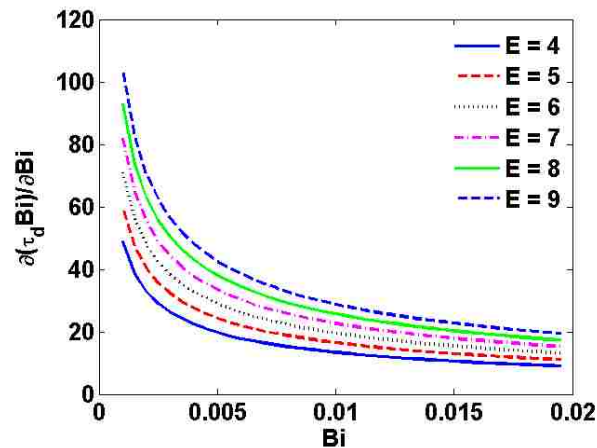
Figure 5.10. Partial derivative of $\tau_d \text{Bi}$ with respect to Bi.
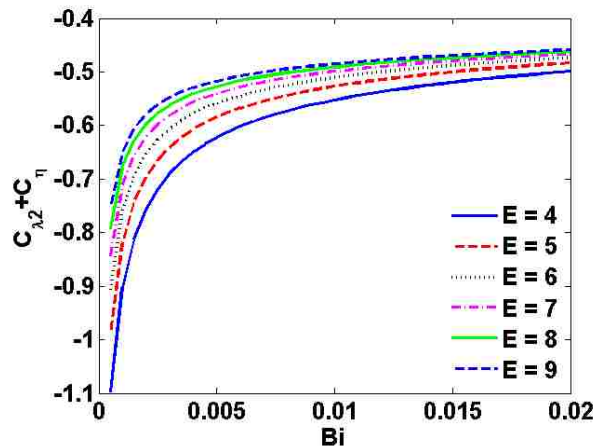
Figure 5.11. Summation of $C_{\lambda 2}$ and C_η as a function of Bi.

5.4.3. Paste Solids Loading. Similar to the paste material, the change of paste solids loading will change all of the material properties. When paste material changes, the properties change discretely to other values. When paste solids loading changes, the properties changes continuously. Previous research has shown that paste density, specific heat, and latent heat can be computed by the law of mixtures. Also, paste thermal conductivity can be estimated using Eq. (4.12). Let the subscripts e and w denote ceramic and water, respectively, and the variable v denote the volume fraction. To study the effect of paste solids loading, Eq. (5.37) is differentiated with respect to ceramic volume fraction

$$
\begin{aligned}
\frac{\partial t_d}{\partial v_e} &= \frac{\partial t_d}{\partial k}\frac{\partial k}{\partial v_e} + \frac{\partial t_d}{\partial c}\frac{\partial c}{\partial v_e} + \frac{\partial t_d}{\partial L}\frac{\partial L}{\partial v_e} + \frac{\partial t_d}{\partial \rho}\frac{\partial \rho}{\partial v_e} \\[2mm]
&= \frac{3\left(k_e - k_w\right)\left\{1 + 2\left\{\left[\left(3v_e - 1\right)k_e + \left(2 - 3v_e\right)k_w\right]^2 + 8k_e k_w\right\}^{-\frac{1}{2}}\right\}}{4}\frac{\partial t_d}{\partial k} \\[2mm]
&\quad + \frac{\left(c_e - c_w\right)\rho_e \rho_w}{\left[\rho_e v_e + \rho_w\left(1 - v_e\right)\right]^2}\frac{\partial t_d}{\partial c} + \frac{-\rho_e \rho_w L_w}{\left[\rho_e v_e + \rho_w\left(1 - v_e\right)\right]^2}\frac{\partial t_d}{\partial L} + \left(\rho_e - \rho_w\right)\frac{\partial t_d}{\partial \rho}
\end{aligned}
\tag{5.52}
$$

It can be seen in Eq. (5.52) that the relationship between critical freezing time and paste solids loading depends on the ceramic properties. Typically, the ceramic particles have

larger thermal conductivity, smaller specific heat, and larger density than water. In this case, the first three terms of Eq. (5.52) are negative, and the last term of Eq. (5.52) is positive. However, because of the large latent heat, the term $\dfrac{-\rho_e \rho_w L_w}{\left[\rho_e v_e + \rho_w\left(1-v_e\right)\right]^2} \dfrac{\partial t_d}{\partial L}$ dominates the expression for the materials studied in this paper. In this case, as the paste solids loading increases, the critical freezing time decreases.

5.4.4. Ambient Temperature. To study the effect of ambient temperature, Eq. (5.37) is differentiated with respect to ambient temperature. Ambient temperature only affects the non-dimensional latent heat. Therefore

$$\begin{aligned}
\frac{\partial t_d}{\partial T_\infty} &= \frac{\rho c \Delta z^2}{k} \frac{\partial \tau_d}{\partial E} \frac{\partial E}{\partial T_\infty} \\
&\approx \frac{\rho c \Delta z^2}{k\left(T_S - T_\infty\right)} \frac{E}{\left(1 + 2\mathrm{Bi} + C_{\lambda 1}\right)}
\end{aligned} \tag{5.53}$$

All of the parameters in Eq. (5.53) are positive; therefore, the derivative is also positive. For the same paste and environmental conditions, as the ambient temperature increases, the critical freezing time increases nonlinearly.

5.4.5. Filament Height. To study the effect of filament height, Eq. (5.37) is differentiated with respect to filament height. Filament height appears in both the conversion from non-dimensional freezing time to dimensional freezing time and in the effective Biot number. Therefore

$$\begin{aligned}
\frac{\partial t_d}{\partial \Delta z} &= \frac{\rho c}{k}\left(2\Delta z \tau_d + \Delta z^2 \frac{\partial \tau_d}{\partial \mathrm{Bi}} \frac{\partial \mathrm{Bi}}{\partial \Delta z}\right) \\
&= \frac{2\rho c \Delta z}{k}\left(\tau_d + \mathrm{Bi}\frac{\partial \tau_d}{\partial \mathrm{Bi}}\right) \\
&= \frac{2\rho c \Delta z}{k}\frac{\partial\left(\tau_d \mathrm{Bi}\right)}{\partial \mathrm{Bi}}
\end{aligned} \tag{5.54}$$

As plotted in Figure 5.10, the partial derivative in Eq. (5.54) is always positive. Therefore, for the same paste and environmental conditions, as the filament height increases, the critical freezing time increases nonlinearly.

5.4.6. Filament Width. To study the effect of filament width, Eq. (5.37) is differentiated with respect to the filament width. Filament width only affects the effective Biot number. Therefore

$$\frac{\partial t_d}{\partial \Delta y} = \frac{\rho c \Delta z^2}{k} \frac{\partial \tau_d}{\partial \mathrm{Bi}} \frac{\partial \mathrm{Bi}}{\partial \Delta y}$$
$$= -\frac{h \rho c \Delta z^4}{k^2 \Delta y^2} \frac{\partial \tau_d}{\partial \mathrm{Bi}} \qquad (5.55)$$

As plotted in Figure 5.8, the term $\partial \tau_d/\partial \mathrm{Bi}$ is always negative. Therefore, this derivative is always positive. For the same paste and environmental conditions, as the filament width increases, the critical freezing time increases nonlinearly.

5.5. EXPERIMENTAL VALIDATION

With the model derived in Section 5.1, the critical freezing time of thin-wall parts can be computed efficiently, and the error can be analyzed with the relationship derived in Section 5.4.

5.5.1. Experimental Setup and Paste Preparation. The paste was a combination of Al_2O_3 powder (A-16SG, ALMATIS), DARVAN® C-N (Ammonium polymethacrylate, Vanderbilt Minerals, LLC), METHOCEL F4M (Methylcellulose, Dow Chemical Company) and deionized water. The alumina powder was dispersed in water using DARVAN C and then ball milled for approximately 15 hours to break up agglomerates and to produce a uniform mixture. METHOCEL was then added to the slurry at 70°C with mechanical stirring to increase paste viscosity and to assist in forming a stronger green body after drying. Finally, a vacuum mixer (Whip Mix, Model F) was used to remove air bubbles. The components of paste used for experiments conducted in this study are listed in Table 5.1.

The FEF setup is comprised of three subsystems: a gantry controlled by a motion card (DELTA TAU Data Systems Inc.), extruders controlled by LabVIEW, and a freezer encompassing the entire machine. Figure 5.12 shows different parts of the FEF machine.

Table 5.1. Components of pastes used for experiments conducted in this paper.

Paste	Al_2O_3, 45% solids loading	Al_2O_3, 60% solids loading
Ceramic powder (g)	326	585
Water (g)	100	100
Binder METHOCEL (g)	4.5	3.5
Dispersant Darvan C (g)	3.1	5.5
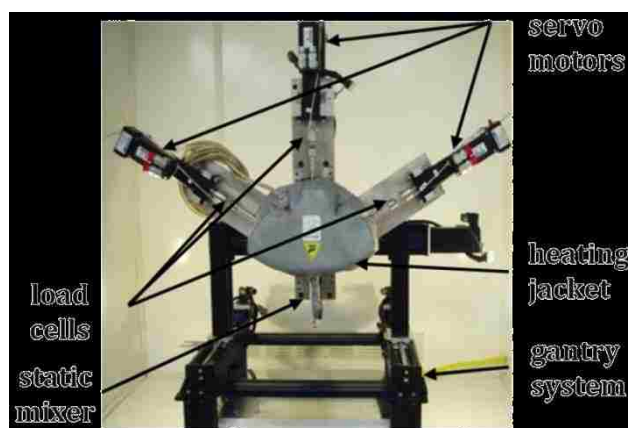
Figure 5.12. Different parts of FEF machine.

The chamber temperature, also referred to as the ambient temperature, is reduced from room temperature using a liquid nitrogen tank connected to the chamber via tubing. A solenoid valve is used to maintain the ambient temperature at the desired value by connecting/disconnecting the flow of nitrogen into the chamber. To preclude freezing of the paste inside the syringe, specially designed heating jacket with a controllable temperature was employed. Another heater surrounds the nozzle to prevent clogging as a result of freezing of the paste at the nozzle tip. The paste is extruded through a 610 μm diameter nozzle and deposited on an aluminum substrate which is at ambient temperature (a thermocouple is utilized to measure this temperature as well). Two fans cause the air to flow around the part being fabricated to enable forced convection.

To validate the analytical results, thin-wall square parts were fabricated with different process parameters. If each layer has enough time to freeze, it can bear the weight of next layers and the part will stand. However, if each layer does not have enough time to freeze, the part will deform and possibly collapse. Table 5.2 shows the parameters affecting the critical time and their values during the experiments.

To obtain the critical freezing time experimentally for each set of parameters, various travel speeds and side lengths were examined. Clearly, if the nozzle moves faster or the part has a shorter side length, the total time between layers will be smaller. In these experiments, two different travel speeds (12.7 and 21.2 mm/s) and 12 different side lengths (17.8-68.6 mm) were used to find critical freezing time experimentally and compare them with analytical predictions. In order to prove the experimental results are repeatable, two batches of paste were used in separate experimental runs for both experiment groups.

Table 5.2. Constant and variable parameters used in experimental studies.

Constant Parameter	Value
Syringe temperature (°C)	20
Nozzle temperature (°C)	20
Filament width (µm)	1010
Variable Parameter	Value
Solids Loading (% Vol.)	45, 60
Convection condition	Forced, Natural
Ambient temperature (°C)	−10, −20
Filament height (µm)	300, 500

5.5.2. Possible Error Sources. There are uncertainties in the values of some of the parameters which affect the accuracy of the experimental results. The actual solids loadings of the pastes are not exactly equal to the desired values and were found to vary by approximately 3%. Furthermore, the trace amount (1-4 vol.%) of binder and dispersant were neglected when calculating the thermal conductivity of the paste. The

flow rate of the paste from the nozzle is not constant during an experiment as a result of minor inconsistency in the paste preparation process and the paste compressibility. This was found to lead to approximately 5% variation in filament width. Although a closed loop control system was employed to control the temperature inside the chamber, variations of approximately ±1 °C were observed. The flow condition in the chamber can be very complex. Even when the fan is off, due to the flow of nitrogen and the machine motion, the part will not experience pure natural convection. When the fan is on, the inside of the part does not have exactly the same convection condition as the outside of the part, nor does it have pure natural convection. The effects of each error source on critical freezing time are discussed case by case in the next section.

5.5.3. Experiment Group 1. For the experiments conducted in experiment group1, the material was 45% solids loading alumina paste, the convection condition was forced, the ambient temperature was −20 °C, the travel speed was 12.7 mm/s, and the filament height and width were 500 and 1010 μm, respectively. The estimated average thermal conductivity of this paste is 10.48 W/m·°C. With these experiment conditions, the predicted critical freezing time is 8.14 s and the corresponding critical side length is 25.9 mm. If the part has a larger size, it should stand (i.e., not deform or collapse). If the part has a smaller size, it is expected to deform or collapse. The results of experiment group 1 are listed in Table 5.3, the effects of possible sources are shown in Figure 5.13, and part photos are shown in Figure 5.14.

The experimental critical freezing times for the pastes in batches #1 and #2 are 9.6 and 8.4 s, and the errors between the predicted and measured results are 17.9% and 3.2%, respectively. Because the ambient temperature is −20 °C, the effect of ambient temperature and convection coefficient error are not as significant as the effect of solids loading error. If the paste solids loading decreases to 40%, the critical freezing time will increase approximately 25%. If the ambient temperature increases to −18 °C or the convection coefficient decreases 10%, the critical freezing time will increase less than 10%. When the total time between layers is close to the critical freezing time, a small change in the total time between layers may result in a dramatically different build, as seen in photos (a) and (b) in Figure 5.14.

Table 5.3. Experimental and predicted results for experiment group 1.

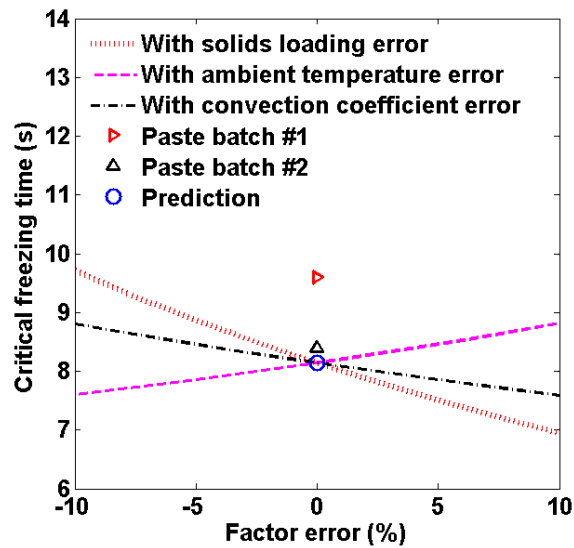| Side Length (mm)	Experimental Result	Predicted Result
Paste batch #1		
17.8	Collapsed	Collapsed
22.9	Collapsed	Collapsed
25.4	Collapsed	Collapsed
27.9	Deformed	Stood
33.0	Stood	Stood
Paste batch #2		
20.3	Collapsed	Collapsed
22.9	Collapsed	Collapsed
25.4	Deformed	Collapsed
27.9	Stood	Stood
33.0	Stood	Stood

Figure 5.13. Predicted critical freezing time and effects of error sources for experiment group 1.
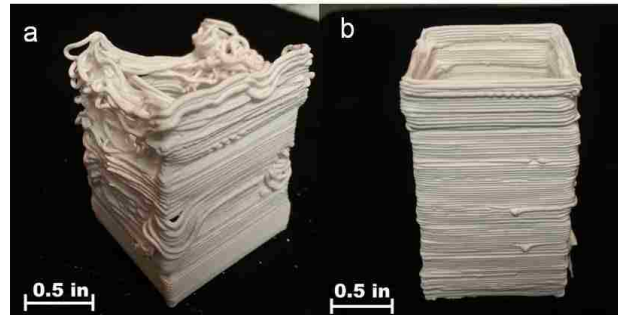
Figure 5.14. Parts fabricated in experiment group 1 using paste batch #2 (a) 25.4 mm (b) 27.9 mm.

5.5.4. Experiment Group 2. For the experiments conducted in experiment group 2, the material was 60% solids loading alumina paste, the convection condition was natural, the ambient temperature was $-10\,°C$, the travel speed was 21.2 mm/s, and the filament height and width were 300 and 1010 μm, respectively. The estimated average thermal conductivity of this paste is 18.81 W/m·°C. With these experiment conditions, the predicted critical freezing time is 11.16 s and the corresponding critical side length is 59.1 mm. The results of experiment group 2 are listed in Table 5.4, the effects of possible sources are shown in Figure 5.15, and part photos are shown in Figure 5.16. Although the freezing time and fabrication results are very different for parts in Figures 5.14 and 5.16, the first 12-15 layers of each sample visually have good quality. This phenomenon can be explained by the work in Section 4. When the paste is close to the substrate, conduction dominates the heat transfer process and the first several layers freeze very fast despite convection conditions and total time between layers. The lumped method presented in this section mainly focuses on computing the critical freezing time, which can be used to predict whether parts with large numbers of layers can be successfully built. If a part only has a few layers, then the part may still be successfully built even if the total time between layers is shorter than the critical freezing time. In that case, the numerical simulation model presented in Section 4 is more suitable for computing the freezing time and determining if the part can be successfully built.

The experimental critical freezing times for the pastes in batches #1 and #2 are 12.5 and 12.0 s, and the errors between the predicted and measured results are 12.0% and

7.5%, respectively. The effect of solids loading error is still large. If the paste solids loading decreases to 55%, the critical freezing time will increase approximately 20%. If the ambient temperature increases to −9 °C, the critical freezing time will increase less than 10%. The effect of convection coefficient becomes less significant since the parts fabricated in group 2 are subjected to natural convection instead of forced convection.

Table 5.4. Experimental and predicted results for experiment group 2.

Side Length (mm)	Experimental Result	Predicted Result
Paste batch #1		
55.9	Collapsed	Collapsed
61.0	Collapsed	Stood
63.5	Deformed	Stood
68.6	Stood	Stood
76.2	Stood	Stood
Paste batch #2		
55.9	Collapsed	Collapsed
61.0	Collapsed	Stood
66.0	Stood	Stood
68.6	Stood	Stood

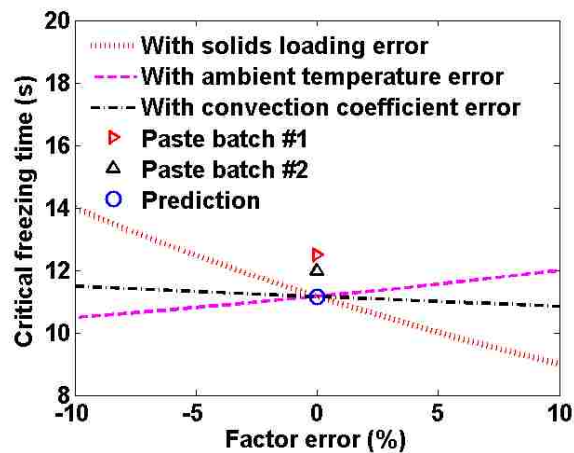Figure 5.15. Predicted critical freezing time and effects of error sources for experiment group 2.
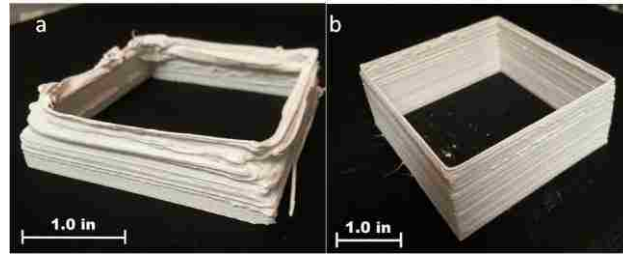
Figure 5.16. Parts fabricated in experiment group 2 using paste batch #2 (a) 61.0 mm (b) 66.0 mm.

5.6. SUMMARY AND CONCLUSIONS FOR PASTE FREEZING IN FEF OF THIN-WALL PARTS

A simplified 1D heat transfer model was developed to efficiently study the freezing time of aqueous-based paste extruded in a freezing environment. The 1D model was validated by 3D simulations conducted using the commercial finite element software FLUENT. When the paste is near the substrate, the paste freezing time is small. As the part height increases, the paste freezing time increases, finally reaching a steady-state value. When this steady-state freezing time is larger than the total time between layers, the paste will be in a semiliquid state and the part enters a semifrozen region. When the steady-state freezing time is smaller than the total time between layers, the paste will be totally frozen. The critical freezing time, which is the steady-state freezing time when it is equal to the total time between layers, is theoretically the optimal total time between layers for the FEF process.

An analytical freezing time model for thin-wall part was developed using a lumped method in order to gain more physical understanding about the freezing process of aqueous-based pastes extruded in a freezing environment. This method can be used to predict the freezing time of thin-wall parts with large numbers of layers. For parts with small numbers of layers, a detailed numerical simulation is required to compute the freezing time. The major assumption in the lumped method is that the temperature gradient is negligible inside a single paste filament.

Two non-dimensional factors, the non-dimensional latent heat and the effective Biot number, were shown to be the main variables affecting the non-dimensional critical

freezing time. As the non-dimensional latent heat increases, the non-dimensional critical freezing time increases linearly. As the effective Biot number increases, the non-dimensional critical freezing time decreases nonlinearly. The two non-dimensional factors are affected by six factors, i.e., convection coefficient, paste material, paste solids loading, ambient temperature, filament height, and filament width. The effects of these dimensional factors on the critical freezing time were also studied. As the convection coefficient increases, the critical freezing time decreases nonlinearly. As each of the ambient temperature, filament height, and filament width increases, the critical freezing time increases nonlinearly. The effects of paste material and paste solids loading are complex due to the simultaneous changes of the paste thermal conductivity, specific heat, latent heat, and density. However, the effect of each single material property is clear. As the thermal conductivity increases, the critical freezing time decreases nonlinearly. As the specific heat increases, the critical freezing time increases nonlinearly. As the latent heat or density increases, the critical freezing time increases nearly linearly. The effect of initial paste temperature was not studied analytically; however, the numerical simulation showed that as the initial paste temperature increases, the critical freezing time increases linearly.

Experiments were conducted using different pastes and extrusion parameters. The experimental critical freezing times have good agreement with the predicted critical freezing times using the lumped method as the average error is approximately 10% and the maximum error is 17.9%. The errors are mainly due to the uncertainty in the ambient temperature, ambient flow, and paste solids loading.

6. SUMMARY AND CONCLUSIONS

The Freeze-form Extrusion Fabrication process can be divided into two stages. The first stage is the paste flow in the extruder, and the second stage is the freezing process after the paste is deposited. During the first stage, the paste temperature is maintained in a small range above the freezing point, and fluid dynamics is dominating. During the second stage, the paste velocity is near zero, and heat transfer becomes dominating. Both of the two stages were studied in this paper.

The paste flow stage was studied in Sections 2 and 3. A dynamic extrusion force constitutive model was developed to describe the relationship between the plunger velocity and the extrusion force in the extrusion of aqueous-based ceramic paste. A modified Herschel-Bulkley model was used to describe the viscosity of aqueous-based ceramic paste. The steady-state component of the constitutive model was then developed based on the Navier-Stokes equation. Because of the compressibility introduced by the trapped air, the extrusion force dynamic was described by a first-order nonlinear differential equation using plunger velocity as an input. The settling time depends on the amount of air trapped in the paste and the magnitude of the extrusion force. As more air is trapped in the paste, the settling time increases; as the extrusion force increases, the settling time and gain both decrease. The dynamics that occur during air bubble release, which causes a sudden drop in the extrusion force due to the change of the volume of paste in the nozzle, can be described by the developed constitutive model.

A series of experimental and numerical studies were conducted to verify the developed constitutive model. A capillary rheometer was used to determine the viscosity model parameters, which were then used for the prediction of extrusion forces in a single extruder system. Extrusion experiments were also conducted in this single extruder system, and a good agreement was obtained between the predicted and measured extrusion forces. The extrusion experiments conducted on the capillary rheometer and on the single extruder system proved that the large settling time is mainly caused by the air trapped in the paste and the change of settling time also depends on the extrusion force. As the extrusion force increases from a small value, the settling time decreases rapidly, giving the dynamic response the appearance of a quadratic response. When the extrusion

force is large, the settling time changes slowly, thus, the dynamic response is dominated by a first-order response. Air bubble release was studied by a series of simulations, which showed that the magnitude of drop in the extrusion force depends on the air bubble volume. Experimental and simulation results were compared for the dynamic response models of extrusion process and air bubble release. Good agreements were obtained in all of the experimental and simulation comparisons, suggesting that the constitutive model can be used to predict the steady-state and transient extrusion force responses, as well as to describe the air bubble release phenomenon in aqueous-based extrusion of ceramic paste.

The paste freezing stage was studied in Sections 4 and 5. A simplified 1D heat transfer model was developed to efficiently study the freezing time of aqueous-based paste extruded in a freezing environment. The 1D model was validated by 3D simulations conducted using the commercial finite element software FLUENT. When the paste is near the substrate, the paste freezing time is small. As the part height increases, the paste freezing time increases, finally reaching a steady-state value. When this steady-state freezing time is larger than the total time between layers, the paste will be in a semiliquid state and the part enters a semifrozen region. When the steady-state freezing time is smaller than the total time between layers, the paste will be totally frozen. The critical freezing time, which is the steady-state freezing time when it is equal to the total time between layers, is theoretically the optimal total time between layers for the FEF process.

An analytical freezing time model for thin-wall part was developed using a lumped method in order to gain more physical understanding about the freezing process of aqueous-based pastes extruded in a freezing environment. This method can be used to predict the freezing time of thin-wall parts with large numbers of layers. For parts with small numbers of layers, a detailed numerical simulation is required to compute the freezing time. The major assumption in the lumped method is that the temperature gradient is negligible inside a single paste filament.

Two non-dimensional factors, the non-dimensional latent heat and the effective Biot number, were shown to be the main variables affecting the non-dimensional critical freezing time. As the non-dimensional latent heat increases, the non-dimensional critical freezing time increases linearly. As the effective Biot number increases, the non-

dimensional critical freezing time decreases nonlinearly. The two non-dimensional factors are affected by six factors, i.e., convection coefficient, paste material, paste solids loading, ambient temperature, filament height, and filament width. The effects of these dimensional factors on the critical freezing time were also studied. As the convection coefficient increases, the critical freezing time decreases nonlinearly. As each of the ambient temperature, filament height, and filament width increases, the critical freezing time increases nonlinearly. The effects of paste material and paste solids loading are complex due to the simultaneous changes of the paste thermal conductivity, specific heat, latent heat, and density. However, the effect of each single material property is clear. As the thermal conductivity increases, the critical freezing time decreases nonlinearly. As the specific heat increases, the critical freezing time increases nonlinearly. As the latent heat or density increases, the critical freezing time increases nearly linearly. The effect of initial paste temperature was not studied analytically; however, the numerical simulation showed that as the initial paste temperature increases, the critical freezing time increases linearly.

Experiments were conducted using different pastes and extrusion parameters. The experimental critical freezing times have good agreement with the predicted critical freezing times using the lumped method as the average error is approximately 10% and the maximum error is 17.9%. The errors are mainly due to the uncertainty in the ambient temperature, ambient flow, and paste solids loading.

BIBLIOGRAPHY

[1] Huang, T., Mason, M. S., Hilmas, G. E., and Leu, M. C., 2006, "Freeze-Form Extrusion Fabrication of Ceramic Parts," *Virtual and Physical Prototyping*, 1(2), pp. 93-100.

[2] Mason, M. S., Huang, T., Landers, R. G., Leu, M. C., and Hilmas, G. E., 2009, "Aqueous-based Extrusion of High Solids Loading Ceramic Pastes: Process Modeling and Control," *Journal of Materials Processing Technology*, 209, pp. 2946-2957.

[3] Zhao, X., Landers, R. G., and Leu, M. C., 2010, "Adaptive Extrusion Force Control of Freeze-form Extrusion Fabrication Processes," *ASME Journal of Manufacturing Science and Engineering*, 132(6), p. 065504.

[4] Benbow, J. J., Lawson, T. A., Oxley, E. W., and Bridgwater, J., 1989, "Prediction of Paste Extrusion Pressure," *American Ceramic Society Bulletin*, 68, pp. 1821-1824.

[5] Padmanabhan, M., and Bhattacharya, M., 1989, "Analysis of Pressure Drop in Extruder Dies," *Journal of Food Science*, 54, pp. 709-713.

[6] Li, Y. Y., and Bridgwater, J., 2000, "Prediction of Extrusion Pressure using an Artificial Neural Network," *Powder Technology*, 108(1), pp. 65-73.

[7] Shepard, T., Nisaratanaporn, E., and McShane, H. B., 1998, "Material Flow and Pressure Prediction when Extruding through Bridge Dies," *Zeitschrift fuer Metallkunde Materials Research and Advanced Techniques*, 89, pp. 327-337.

[8] Horrobin, D. J., and Nedderman, R. M., 1998, "Die Entry Pressure Drops in Paste Extrusion," *Chemical Engineering Science*, 53(18), pp. 3215-3225.

[9] Lang, U., and Michaeli, W., 1998, "Development of a Mathematical Model for the Calculation of the Pressure Drop in Extrusion Dies," *Journal of Reinforced Plastics and Composites*, 17, pp. 1110-1118.

[10] Smay, J. E., Cesarano, J., and Lewis, J. A., 2002, "Colloidal Inks for Directed Assembly of 3-D Periodic Structures," *Langmuir*, 18(14), pp. 5429-5437.

[11] Herschel, W., and Bulkley, R., 1926, "Measurement of Consistency as Applied to Rubber Benzene Solutions," *Proceedings - American Society for Testing Materials*, 26(82), pp. 621-629.

[12] Chilton, R. A., and Stainsby, R., 1998, "Pressure Loss Equations for Laminar and Turbulent Non-Newtonian Pipe Flow," *Journal of Hydraulic Engineering*, 124(5), pp. 522-529.

[13] Oakes, T., Kulkarni, P., Landers, R. G., and Leu, M. C., "Development of Extrusion-on-Demand for Ceramic Freeze-form Extrusion Fabrication," *Proceedings of Solid Freeform Fabrication Symposium*, Austin, Texas, pp. 206-218, 2009.

[14] Zhu, C., and Smay, J. E., 2011, "Thixotropic Rheology of Concentrated Alumina Colloidal Gels for Solid Freeform Fabrication," *Journal of Rheology*, 55(3), pp. 655-672.

[15] Ram, A., and Tamir, A., 1964, "A Capillary Viscometer for Non-Newtonian Liquids," *Industrial and Engineering Chemistry*, 56(2), pp. 47-53.

[16] Zeng, K., Pal, D., and Stucker, B., 2012, "A Review of Thermal Analysis Methods in Laser Sintering and Selective Laser Melting," *Solid Freeform Fabrication Symposium*, Austin, TX, pp. 796-814.

[17] Tapia, G., and Elwany, A., 2014, "A Review on Process Monitoring and Control in Metal-Based Additive Manufacturing," *ASME Journal of Manufacturing Science and Engineering*, 136(6), p. 060801.

[18] Zhao, H., Zhang, G., Yin, Z., and Wu, L., 2013, "Effects of Interpass Idle Time on Thermal Stresses in Multipass Multilayer Weld-Based Rapid Prototyping," *ASME Journal of Manufacturing Science and Engineering*, 135(1), p. 011016.

[19] Jamshidinia, M., Kong, F., and Kovacevic, R., 2013, "Numerical Modeling of Heat Distribution in the Electron Beam Melting® of Ti-6Al-4V," *ASME Journal of Manufacturing Science and Engineering*, 135(6), p. 061010.

[20] Paul, R., Anand, S., and Gerner, F., 2014, "Effect of Thermal Deformation on Part Errors in Metal Powder Based Additive Manufacturing Processes," *ASME Journal of Manufacturing Science and Engineering*, 136(3), p. 031109.

[21] Zhang, W., Leu, M. C., Ji, Z., and Yan, Y., 1999, "Rapid Freezing Prototyping with Water," *Materials and Design*, 20(2-3), pp. 139-145.

[22] Leu, M. C., Zhang, W., and Sui, G., 2000, "An Experimental and Analytical Study of Ice Part Fabrication with Rapid Freeze Prototyping," *CIRP Annals - Manufacturing Technology*, 49(1), pp. 147-150.

[23] Feng, C., Yan, S., Zhang, R., and Yan, Y., 2005, "Heat Transfer Analysis of Rapid Ice Prototyping Process by Finite Element Method," *Materials and Design*, 28(3), pp. 921-927.

[24] Liu, Q., and Leu, M. C., 2007, "Finite Element Analysis of Solidification in Rapid Freeze Prototyping," *ASME Journal of Manufacturing Science and Engineering*, 129(4), pp. 810-820.

[25] Denlinger, E. R., Irwin, J., and Michaleris, P., 2014, "Thermomechanical Modeling of Additive Manufacturing Large Parts," *ASME Journal of Manufacturing Science and Engineering*, 136(6), p. 061007.

[26] Michaleris, P., 2014, "Modeling Metal Deposition in Heat Transfer Analyses of Additive Manufacturing Processes," *Finite Elements in Analysis and Design*, 86, pp. 51-60.

[27] Zhang,Y., and Faghri, A., 1999, "Melting of a Subcooled Mixed Powder Bed with Constant Heat Flux Heating," *International Journal of Heat and Mass Transfer*, 42(5), pp. 775-788.

[28] ANSYS FLUENT 12.0 Documentation.

[29] Seber, G. A. F., and Wild, C. J., 2003, *Nonlinear Regression*, Hoboken, NJ: Wiley-Interscience.

[30] Vollera, V. R., and Swaminathana, C. R., 1991, "Generalized Source-Based Method for Solidification Phase Change," *Numerical Heat Transfer, Part B: Fundamentals*, 19(2), pp. 175-189.

[31] Brailsford, A. D., and Major, K. G., 1964, "The Thermal Conductivity of Aggregates of Several Phases, Including Porous Materials," *British Journal of Applied Physics*, 15(3), pp 313-319.

[32] Landauer, R., 1952, "The Electrical Resistance of Binary Metallic Mixtures," *Journal of Applied Physics*, 23, pp. 779-784.

[33] Cengel, Y. A., 2002, *Heat* Transfer*, a Practical Approach*, WCB/McGraw-Hill, New York.

[34] Yueh, W. C., 2005, "Eigenvalues of Several Tridiagonal Matrices," *Applied Mathematics E-Notes*, 5, pp. 66-74.

VITA

Mingyang Li was born on November 9, 1983 in Shandong, P. R. China. In July 2005, he received his Bachelor of Engineering in Thermal Energy and Power Engineering from Tsinghua University, P. R. China.

Upon completion of his undergraduate degree, he worked at the Fuhai Securities Company as stock trader from August 2005 to July 2007.

In September 2007, he began his study for Master's degree. In July 2009, he received his Master of Engineering in Engineering Thermal from Beijing Jiaotong University, P. R. China.

In August 2010, he began his study for Doctor's degree in Mechanical Engineering. His research areas include heat transfer, fluid dynamics, modeling and simulation, rapid prototyping, and additive manufacturing. He received his Doctor of Philosophy in Mechanical Engineering from Missouri University of Science and Technology in May, 2016.